

**HZDR-105**

**INFRARED NANOSPECTROSCOPY  
AT CRYOGENIC TEMPERATURES  
AND ON SEMICONDUCTOR NANOWIRES**

Denny Lang

Wissenschaftlich-Technische Berichte  
HZDR-105 · ISSN 2191-8708

**WISSENSCHAFTLICH-  
TECHNISCHE BERICHTE**

**hZDR**



**HELMHOLTZ  
ZENTRUM DRESDEN  
ROSSENDORF**



Wissenschaftlich-Technische Berichte  
HZDR-105

Denny Lang

**INFRARED NANOSPECTROSCOPY  
AT CRYOGENIC TEMPERATURES  
AND ON SEMICONDUCTOR NANOWIRES**

**HZDR**

 **HELMHOLTZ**  
| ZENTRUM DRESDEN  
| ROSSENDORF

Druckausgabe: ISSN 2191-8708

Elektronische Ausgabe: ISSN 2191-8716

Die elektronische Ausgabe erscheint unter Creative Commons License (CC BY 4.0):

<https://www.hzdr.de/publications/Publ-29741>

<urn:nbn:de:bsz:d120-qucosa2-355963>

Die vorliegende Arbeit wurde sowohl als Dissertation an der Fakultät Mathematik und Naturwissenschaften der Technischen Universität Dresden sowie als Wissenschaftlich-Technischer Bericht des Helmholtz-Zentrum Dresden – Rossendorf mit der Berichtsnummer **HZDR-105** veröffentlicht.

2019

Herausgegeben vom

Helmholtz-Zentrum Dresden - Rossendorf

Bautzner Landstraße 400

01328 Dresden

Germany



---

---

Infrared nanospectroscopy  
at cryogenic temperatures and  
on semiconductor nanowires

---

---

DISSERTATION

zur Erlangung des akademischen Grades  
Doctor rerum naturalium  
(Dr. rer. nat.)

durchgeführt am  
Helmholtz-Zentrum Dresden-Rossendorf

vorgelegt  
der Fakultät Mathematik und Naturwissenschaften  
der Technischen Universität Dresden

von  
Dipl.-Phys. Denny Lang  
geboren am 12.09.1988 in Reichenbach im Vogtland



Die Dissertation wurde in der Zeit von Januar 2015 bis Januar 2019 am Institut für Ionenstrahlphysik und Materialforschung am Helmholtz-Zentrum Dresden-Rossendorf (HZDR) angefertigt.

Eingereicht am: 28.03.2019

Verteidigt am: 16.09.2019

Erstgutachter: Prof. Dr. Manfred Helm  
Technische Universität Dresden & HZDR

Zweitgutachter: Prof. Dr. Thomas Taubner  
Rheinisch-Westfälische Technische Hochschule Aachen

---

## Abstract

This PhD thesis concentrates on scattering scanning near-field infrared microscopy (s-SNIM) which utilizes the radiation from the free-electron laser (FEL) at the Helmholtz-Zentrum Dresden-Rossendorf. The FEL is an intense, narrow-band radiation source, tunable from the mid- to far-infrared spectral range (5 meV to 250 meV). The s-SNIM technique enables infrared microscopy and spectroscopy with a wavelength-independent spatial resolution of about 10 nm.

The first part demonstrates the extension of s-SNIM at the FEL towards cryogenic temperatures as low as 5 K. To this end, we show the functionality of our low-temperature s-SNIM apparatus on different samples such as Au, structured Si/SiO<sub>2</sub>, as well as the multiferroic material gallium vanadium sulfide (GaV<sub>4</sub>S<sub>8</sub>). The latter material recently attracted a lot of interest since it hosts a Néel-type skyrmion lattice – a periodic array of spin vortices. Below  $T = 42$  K, GaV<sub>4</sub>S<sub>8</sub> undergoes a structural phase transition and then forms ferroelectric domains, which we can map out by low-temperature s-SNIM. Notably, we found a strong impact on the ferroelectric domains upon infrared irradiation, which we further utilize to calibrate the local heat contribution of the focused infrared beam beneath the s-SNIM probe.

The second part of this thesis contains comprehensive s-SNIM investigations of high-quality semiconductor nanowires (NWs) grown by molecular beam epitaxy. Such NWs are promising building blocks for fast (opto-)electronic nanodevices, amongst others due to their high carrier mobility. We have examined highly doped GaAs/InGaAs core/shell NWs and observed a strong and spectrally sharp plasmonic resonance at about  $\hbar\omega = 125$  meV, using a continuous wave CO<sub>2</sub> laser for probing. If we probe the same NWs utilizing the intense, pulsed FEL radiation, we observe a pronounced redshift to  $\hbar\omega < 100$  meV and a broadening of the plasmonic response. This nonlinear response is most likely induced by heating of the electron gas upon irradiation by the strong FEL pulses. Our observations open up the possibility to actively induce and observe non-equilibrium states in s-SNIM directly by the mid-infrared beam. Beside the nonlinear effect, we prepared and measured cross sections of both homogeneously-doped and modulation-doped core/shell NWs.



## Zusammenfassung

Die vorliegende Dissertation befasst sich mit der streuenden, infraroten Raster-nahfeldmikroskopie (engl. s-SNIM) in Kombination mit dem Freie-Elektronen Laser (FEL) am Helmholtz-Zentrum Dresden-Rossendorf. Der FEL ist eine intensive, schmalbandige Strahlungsquelle, welche vom mittleren bis ferninfraroten Spektralbereich durchstimmbar ist (5 meV bis 250 meV). Die s-SNIM Technik ermöglicht Infrarotmikroskopie- und spektroskopie mit einer wellenlängenunabhängigen räumlichen Auflösung von etwa 10 nm.

Der erste Ergebnisteil demonstriert die Erweiterung eines FEL-basierten s-SNIM hinsichtlich der Möglichkeit, bei tiefen Temperaturen bis 5 K messen zu können. So verdeutlichen wir die Funktionalität unseres Tieftemperatur-s-SNIM anhand verschiedener Proben wie Au, strukturiertem Si/SiO<sub>2</sub> sowie Gallium-Vanadium-Sulfid (GaV<sub>4</sub>S<sub>8</sub>). Das letztgenannte Material erregt momentan ein hohes wissenschaftliches Interesse, da es sogenannte Skyrmionen des Néel-Typs – periodische angeordnete Spinwirbel – enthält. GaV<sub>4</sub>S<sub>8</sub> hat einen strukturellen Phasenübergang bei  $T = 42$  K und beinhaltet bei niedrigeren Temperaturen ferroelektrische Domänen, die wir unter anderem mittels s-SNIM abbilden können. Hierbei beobachten wir einen beträchtlichen Einfluss der Infrarotstrahlung auf die Domänenstruktur. Dies nutzen wir, um den lokalen Hitzeintrag der Infrarotstrahlung lokal unter der s-SNIM Sonde zu quantifizieren.

Der zweite Teil der Ergebnisse beinhaltet s-SNIM Messungen an hochwertigen Halbleiter-Nanodrähten (ND), welche mittels Molekularstrahlepitaxie gewachsen wurden. Derartige ND sind, unter anderem aufgrund ihrer hohen Ladungsträgermobilität, vielversprechende Komponenten für schnelle optoelektronische Nanoelemente der Zukunft. So untersuchen wir beispielsweise hochdotierte GaAs/InGaAs Kern/Schale ND, bei denen wir – unter Verwendung eines Dauerstrich CO<sub>2</sub> Lasers – eine spektral scharfe plasmonische Resonanz bei etwa  $\hbar\omega = 125$  meV beobachten. Betrachten wir selbige ND mittels intensiver, gepulster FEL-Strahlung, ist eine signifikante Rotverschiebung zu  $\hbar\omega < 100$  meV sowie eine Verbreiterung der Resonanz festzustellen. Dieses nichtlineare Verhalten wird zurückgeführt auf eine starke Erhitzung des Elektronengases unter dem Einfluss der intensiven FEL-Pulse. Unsere Erkenntnisse zeigen dahingehend die Möglichkeiten auf, Nichtgleichgewichtszustände im s-SNIM gezielt zu induzieren und zu

beeinflussen. Abgesehen von den Messungen der Nichtlinearität ist die Herstellung und Charakterisierung von ND-Querschnitten – sowohl der genannten homogen dotierten, als auch modulationsdotierten– Gegenstand des zweiten Ergebniskapitels.

# Contents

<b>Abstract</b>	<b>iii</b>
<b>Zusammenfassung</b>	<b>v</b>
<b>1 Introduction</b>	<b>1</b>
<b>2 Fundamentals</b>	<b>3</b>
2.1 Scanning probe techniques . . . . .	3
2.1.1 Atomic force microscopy . . . . .	4
2.1.2 Piezoresponse force microscopy . . . . .	8
2.1.3 Kelvin-probe force microscopy . . . . .	9
2.2 Infrared nanospectroscopy . . . . .	10
2.2.1 The diffraction limit . . . . .	10
2.2.2 Scattering scanning near-field infrared microscopy . . . . .	11
2.2.3 Point-dipole model . . . . .	12
2.2.4 Signal detection . . . . .	17
2.2.5 Higher harmonic demodulation and contrast . . . . .	19
2.2.6 Advantages and limitations of s-SNIM . . . . .	22
2.3 Infrared light sources . . . . .	24
2.3.1 Carbon dioxide laser . . . . .	24
2.3.2 Free-electron laser . . . . .	26
<b>3 Infrared nanospectroscopy at cryogenic temperatures</b>	<b>31</b>
3.1 Introduction . . . . .	31
3.2 Samples . . . . .	33
3.3 Experimental details . . . . .	36
3.3.1 Low-temperature atomic force microscopy . . . . .	36
3.3.2 Optical setup . . . . .	38

3.3.3	Low-temperature scattering scanning near-field infrared microscopy . . . . .	39
3.3.4	Measurement modes and data acquisition . . . . .	42
3.4	Results and discussion . . . . .	44
3.4.1	Performance and IR heating calibration . . . . .	44
3.4.2	s-SNIM study of gallium vanadium sulfide . . . . .	49
3.5	Conclusion . . . . .	51
<b>4</b>	<b>Infrared nanospectroscopy on semiconductor nanowires</b>	<b>53</b>
4.1	Introduction . . . . .	53
4.2	Samples . . . . .	55
4.2.1	GaAs/InGaAs core/shell nanowires . . . . .	55
4.2.2	Modulation doped nanowires . . . . .	56
4.2.3	Nanowire cross sections . . . . .	57
4.2.4	Infrared response of doped nanowires . . . . .	59
4.3	Experimental details . . . . .	61
4.3.1	Room-temperature atomic force microscopy . . . . .	61
4.3.2	Room-temperature scattering scanning near-field infrared microscopy . . . . .	63
4.3.3	Properties of the free-electron laser pulses . . . . .	65
4.4	Results and discussion . . . . .	68
4.4.1	GaAs/InGaAs core/shell nanowires . . . . .	68
4.4.2	Nanowire cross sections . . . . .	75
4.5	Conclusion . . . . .	79
<b>5</b>	<b>Summary and outlook</b>	<b>81</b>
<b>A</b>	<b>Citation metrics</b>	<b>85</b>
<b>B</b>	<b>Additional nanospectroscopic studies</b>	<b>87</b>
B.1	Silicon carbide nanoparticle probes . . . . .	87
B.2	Individual impurities in Si . . . . .	91
B.3	Surface phonon polaritons in molybdenum disulfide . . . . .	96



---

<b>C Derivation of the nonparabolic effective mass and density of states</b>	<b>99</b>
C.1 Effective mass . . . . .	99
C.2 Density of states . . . . .	100
<b>D Comparison of self-homodyne and pseudo-heterodyne detection</b>	<b>103</b>
<b>Bibliography</b>	<b>105</b>
<b>List of Abbreviations</b>	<b>125</b>
<b>List of Symbols</b>	<b>132</b>
<b>List of Publications</b>	<b>133</b>
<b>Acknowledgments</b>	<b>137</b>
<b>Versicherung</b>	<b>139</b>



# 1 Introduction

Already back in 1928, the Irish physicist Edward Hutchinson Synge postulated the idea of using a tiny aperture in the vicinity of a sample to excite and collect light while scanning the surface [1]. As a result, the spatial resolution, which is limited by diffraction to  $\sim \lambda/2$  in conventional far-field microscopy, should be significantly improved. The subdiffraction resolution is possible by accessing the evanescent fields close to the surface. Synge also proposed to utilize a small colloidal particle instead of an aperture and detect the scattered light. Albert Einstein, with whom Synge had a correspondence on this topic, answered in his response letter that Synge's fundamental idea seems to be correct. However, Einstein considered the specific implementation as not feasible at all [2].

Seen in this light, Synge can be considered as the forefather of near-field microscopy, even though his ideas could not be realized until many years later by the extensive developments in the field of nanotechnology. Thus, the rapid progress in scanning probe microscopy [3] in the 1980s contributed decisively to the requirement of rastering a tiny aperture or scattering probe over a surface. Although both the approach of the aperture probe and that of the scattering probe were followed, the latter has proven to be particularly useful in the infrared and THz spectral range. Accordingly, the method is called scattering scanning near-field infrared microscopy (s-SNIM). The latter combines the unique possibilities of infrared and THz spectroscopy, covering numerous fundamental excitations of condensed matter, with a wavelength-independent spatial resolution on the nanometer scale. Especially within the last decade, s-SNIM has established itself as a versatile tool for infrared nanospectroscopy (see Appendix A), essentially contributing in various fields of research. For example, there are important contributions on metamaterials[4–6], two-dimensional materials and van der Waals heterostructures [7–10], semiconductor nanostructures [11, 12], or strongly correlated materials [13].

The s-SNIM technology is in constant evolution, among other things to be able to observe physical processes with high temporal resolution [14, 15] or at low temperatures [16]. The latter is of particular importance when it comes to far-infrared or THz spectroscopy, where the photon energy approaches the thermal energy scale  $\sim k_B T$ . Moreover, complex phase transitions in exotic material classes such as multiferroic materials or high-temperature superconductors have to be studied at low temperatures. Here, the nanometer spatial resolution of s-SNIM promises great advances since the local structural changes, e. g. in the case of phase coexistence, can be observed. Thus, the first part of this thesis demonstrates our low-temperature s-SNIM system operating down to  $T = 5$  K. In addition to being used as s-SNIM, the apparatus allows the application of complementary *in situ* modes such as Kelvin-probe force microscopy and piezoresponse force microscopy. Moreover, we study the local heating impact of the infrared probe beam beneath the metallized s-SNIM tip. As infrared sources we apply both a tunable CO<sub>2</sub> laser as well as the free-electron laser (FEL) at the Helmholtz-Zentrum Dresden-Rossendorf. The FEL has the unique feature of being tunable over a wide spectral range spanning from 5  $\mu\text{m}$  to 250  $\mu\text{m}$  (5 meV to 250 meV) while providing intense, narrow-band radiation at a high repetition rate.

Such intense, pulsed FEL radiation can drive interesting non-equilibrium phenomena such as the strong heating of an electron gas. The latter is demonstrated in the second part of this thesis. Here, we find a pronounced redshift of the plasma resonance of about 25 % in highly-doped InGaAs/GaAs core/shell nanowires (NWs). This redshift is attributed to an associated increase in the effective mass, which can be explained by a significant increase in the temperature of the electron gas. In our model, this causes an altered Fermi-Dirac distribution of carriers in the nonparabolic  $\Gamma$ -valley of InGaAs. With this we can estimate a maximal temperature of the electron gas of about 3900 K and an effective electric peak field of  $\sim 50$  kV/cm. Hence, for the first time, we directly observe a nonlinear impact of the mid-infrared probe beam in s-SNIM. In the regime of low peak fields using a continuous wave laser, there is a sharp plasma resonance at about 125 meV, demonstrating the excellent quality of our NWs. Finally, this requires a high charge carrier density of about  $8 \times 10^{18} \text{ cm}^{-3}$  and, at the same time, a carrier mobility of about  $1000 \text{ cm}^2/\text{Vs}$ . Furthermore, we performed a s-SNIM study of NW cross sections, fabricated by focused ion beam technique.

## 2 Fundamentals

This chapter includes basic experimental methods of atomic force microscopy (AFM) and related modes such as piezoresponse force microscopy (PFM) and Kelvin-probe force microscopy (KPFM). Moreover, a larger section is dedicated to infrared (IR) nanospectroscopy. In particular, scattering scanning near-field infrared microscopy (s-SNIM) that is based on AFM will be introduced both conceptionally and from a theoretical point of view. Finally, the IR sources are introduced on their basic principle and their most important properties.

### 2.1 Scanning probe techniques

The first scanning probe microscopy (SPM) technique, scanning tunneling microscopy (STM), was introduced in 1983 by Binnig<sup>1</sup> et al. [17]. In STM, the tunnel current between a sharp metallic tip and a conductive sample surface serves as a controlled variable. The probe raster scans the surface, while the current is kept constant by precisely readjusting the tip-sample distance. Hence, the equipotential surface of constant electron density is probed, yielding information on the local surface topography and the local electronic configuration. Since typically only one atom of the tip contributes to the tunnelling current, atomic resolution can be achieved. However, STM is basically restricted to conductive samples (or samples covered by a thin metallic layer). Only few years later, in 1986, Binnig et al. [3] introduced the similar concept of AFM that is based on the inter-atomic forces of the tip in proximity to a surface.

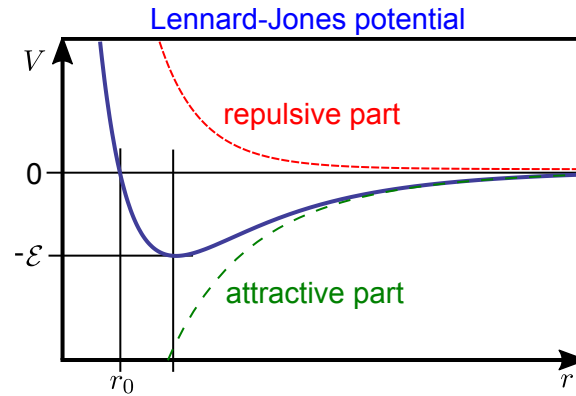


Figure 2.1: Lennard-Jones potential (blue, solid line), approximately describing the tip-sample interaction by a short-range repulsive part (red) and a long-range attractive part (green).

### 2.1.1 Atomic force microscopy

The force in between two atoms that are not charged or chemically bound is commonly approximated by the empirical Lennard-Jones (12-6) potential [18, 19]

$$V(r) = 4\mathcal{E} \left[ \left( \frac{r_0}{r} \right)^{12} - \left( \frac{r_0}{r} \right)^6 \right], \quad (2.1)$$

where  $r_0$  is the intersection with the  $x$ -axis [ $V(\sigma) = 0$ ],  $\mathcal{E}$  is the minimal energy, and  $r$  is the inter-atomic distance. The  $r^{-12}$  term of Equation (2.1) describes the short-range Pauli repulsion, whereas the  $r^{-6}$  term describes attractive long-range forces such as van der Waals forces. Figure 2.1 depicts the Lennard-Jones potential according to Equation (2.1), with both the repulsive contribution (red) and the attractive contribution (green).

An AFM probe typically consists of a cantilever having a sharp tip at one side. A common material for such a probe is crystalline Si that can be covered by a thin metal layer (e. g. Au or Pt) to ensure electrical conductivity. The motion of the cantilever can be detected, for example, by a laser beam [beam-deflection method, see Figure 2.2 (a)]. The reflected light from the top side of the cantilever is detected by a four-segment diode, where the output voltages of each segment is proportional to the respective intensity. Hence, an out-of-plane motion of the

<sup>1</sup>Gerd Binnig and Heinrich Rohrer received the Nobel Prize for the invention of the STM in 1986.

cantilever is described by

$$D_{\text{oop}} \equiv D \propto \frac{(U_1 + U_2) - (U_3 + U_4)}{U_1 + U_2 + U_3 + U_4}, \quad (2.2)$$

where  $U_i$  are the output voltages of the diode segments as depicted in Figure 2.2 (a). An in-plane displacement, i. e. a torsion of the cantilever, is recognized by

$$D_{\text{ip}} \propto \frac{(U_2 + U_4) - (U_1 + U_3)}{U_1 + U_2 + U_3 + U_4}. \quad (2.3)$$

Another method to detect the motion of the cantilever is based on interferometric detection [Figure 2.2 (b)]. An optical fiber is placed above the cantilever, where one part of the beam, the reference  $I_{\text{ref}}$ , is reflected at the fiber's end, and the other part  $I_c$  is reflected at the cantilever. Both beams superimpose and the detector signal shows the proportionality

$$D \propto \cos\left(\frac{4\pi\Delta z}{\lambda}\right), \quad (2.4)$$

where  $\Delta z$  is the displacement of the cantilever with respect to the fiber's end and  $\lambda$  is the wavelength of the light. When the wavelength is known, the displacement can be measured directly without further calibration (within the unambiguous range). Any in-plane motion of the cantilever, however, can not be detected by the interferometric method.

The simplest way to control the tip-sample distance and hence measure the topography is the contact mode, where the tip is kept in the repulsive regime of Figure 2.1. This is achieved by setting a fixed value of  $D = D_{\text{sp}}$  as set point (SP) and approaching the sample. If the tip feels the repulsive force of the surface, the cantilever bends until  $D_{\text{sp}}$  is reached. Subsequently, a proportional-integral (PI) control loop ensures a constant  $D$  by readjusting the  $z$  displacement of the scanner. The latter is able to move the sample beneath the tip in all three dimensions with a sub-nanometer precision (see Figure 2.2), e. g. by using piezoelectric actuators. Hence, by scanning the lateral orientations  $x$  and  $y$ , a topographic map  $z(x, y)$  is recorded with a lateral resolution in the range of the tip apex ( $\sim 25$  nm) and a sub-nanometer  $z$  resolution (limited by the overall electrical and mechanical AFM stability). A disadvantage of the contact mode is that damage

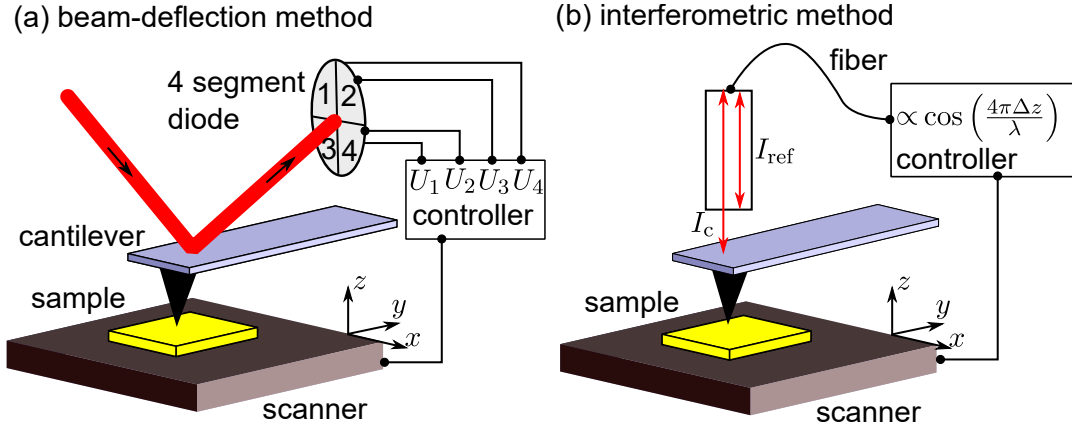


Figure 2.2: (a) Schematic drawing of the beam-deflection method for the detection of the cantilever's motion. Both out-of-plane and in-plane components can be detected. (b) Interferometric method, which only detects the out-of-plane displacement of the cantilever.

either to the tip or the sample during a scan can occur easily, since instant operation in the repulsive regime is necessary. Thus, the tip may also spatially move small objects or particles that are only weakly bound to the surface. Another disadvantage is the higher probability of cantilever torsion at sharp edges that can lead to artifacts (even though the in-plane component can be measured in the case of the beam-deflection method). In this thesis, contact-mode AFM is exclusively applied to perform PFM measurements, which is explained later (see Section 2.1.2).

An alternative way to control the tip-sample distance is the so-called tapping mode. Here, the cantilever is excited resonantly at its mechanical resonance frequency  $\Omega$ . In the experiment, this frequency is typically about 5 kHz to 500 kHz, which mainly depends on the stiffness and geometry of the cantilever. The mechanical amplitude  $A$  and phase  $\Phi$  of the modulated deflection signal  $D(\Omega)$  gets demodulated by a lock-in amplifier. In contrast to the contact mode, now the amplitude  $A$  serves as control parameter for the PI controller. Accordingly, a SP  $A = A_{\text{sp}}$  smaller than the free oscillation amplitude is chosen. A slight shift of the cantilever's frequency due to the approaching sample leads to a large decrease of  $A$ , as depicted in Figure 2.3. Typically, the amplitude in contact is chosen to be 10 nm to 100 nm, which is about 80% of the respective free amplitude. The PI



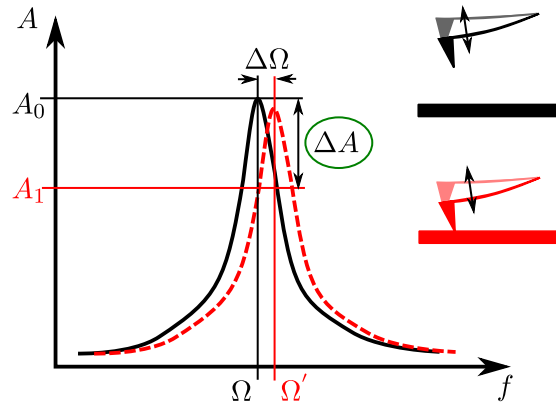


Figure 2.3: Typical amplitude resonance curve of a cantilever (Lorentzian shape) with its free resonance frequency  $\Omega$  and free resonance amplitude  $A_0$ . The interaction with an approaching sample (red) shifts the resonance frequency and hence reduces the amplitude to  $A_1$  at  $\Omega$ . For tapping mode, the oscillation amplitude at a fixed excitation frequency is the guide value for the AFM control loop.

controller corrects the  $z$  value of the scanner to keep  $A$  constant, similar to  $D$  for the contact mode. The advantage of the tapping mode is that a direct contact of the tip to the sample is limited to a much shorter time period and, hence, the damage probability, both for sample and tip, is reduced. Moreover, the impact of cantilever torsion is less critical compared to the contact mode. In addition to the amplitude, a mechanical phase  $\Phi$  is recorded simultaneously. This phase also contains useful information about the sample as it is sensitive to the damping of the tip oscillation [20]. The interpretation of  $\Phi$  may, however, be difficult since different physical origins can cause the same phase contrast.

A partially charged surface can add an additional (long-range) electrostatic repulsive force to the Lennard-Jones potential. Subsequently, the tip cannot approach the surface anymore. In this case, an additional bias voltage for compensation between tip and sample has to be applied, which can be controlled by KPFM (see Section 2.1.3). Furthermore, within this thesis, the tapping mode is applied for all nanospectroscopic measurements since the tip oscillation also modulates the scattered infrared radiation and thus enables a beneficial demodulation technique (see Section 2.2.2).

### 2.1.2 Piezoresponse force microscopy

PFM is an electrical AFM mode that can be applied in contact mode operation with an conductive, i. e. metallized, tip [21, 22]. PFM is commonly used to map ferroelectric domains at the surface of bulk or thin film materials.

In the PFM mode, an AC bias voltage with a frequency  $f_{\text{PFM}}$  is applied between the tip and the back contact of an insulating sample:

$$U_{\text{PFM}} = U_0 \cos(2\pi f_{\text{PFM}} t). \quad (2.5)$$

The applied bias amplitude  $U_0$  depends strongly on the thickness of the investigated sample ( $\sim \text{mV}$  for thin films,  $\sim \text{V}$  for bulk) at a frequency  $f_{\text{PFM}}$  of 1 kHz to 50 kHz for non-resonant excitation<sup>2</sup>.

Piezoelectric samples (such as ferroelectric materials like barium titanate), show a deformation of the crystal lattice in presence of an external electric field due to the inverse piezoelectric effect. The strain  $\vec{X}$  induced by the electric field  $\vec{E}$  can be described by

$$X_i = \sum_{k=1}^3 d_{ki} E_k : i = 1, \dots, 6, \quad (2.6)$$

where  $\mathbf{d}$  is the piezoelectric tensor.

The modulation due to the inverse piezoelectric effect subsequently induces a modulation of the cantilever displacement  $D$ , which can be analyzed by a lock-in amplifier at the excitation frequency  $f_{\text{PFM}}$ . Hence, an amplitude  $A_{\text{PFM}}$  and phase  $\Phi_{\text{PFM}}$  are recorded during an AFM scan (*in situ* to the topography). This can be used to map ferroelectric domains, i. e. areas with differently oriented and/or differently strong permanent electric polarizations. If the in-plane component of the cantilever is detectable, it is also possible to measure in-plane components of the piezoelectric tensor to achieve a more comprehensive view for the reconstruction of the domain pattern [23].

---

<sup>2</sup>The coupled tip-sample system typically has a mechanical resonance at a certain frequency, which can be used to enhance the PFM signal. However, this complicates the interpretation since, for example, phase jumps may occur.

### 2.1.3 Kelvin-probe force microscopy

KPFM is an electrical AFM mode that can be used to map the local surface potential or work function between the sample surface and the (conductive) AFM probe [24–26]. As a side effect, KPFM can compensate electrostatic repulsion at the sample surface that can occur due to induced charges (e. g. by pyroelectricity).

For KPFM, a bias voltage with both an AC part  $U_{AC}$  and a DC part  $U_{DC}$  is applied. In this case, the potential difference between tip and sample can be expressed by

$$U = (U_{DC} - U_{CPD}) + U_{AC} \cos(2\pi f_{KPFM}t) , \quad (2.7)$$

where  $U_{CPD}$  is the (unknown) contact-potential difference.

The applied field induces an additional force to the tip that can be approximated by the force of an electrical capacitor:

$$F = \frac{1}{2} \frac{\partial C}{\partial z} U^2 , \quad (2.8)$$

where  $C$  is the effective capacitance,  $z$  is the tip-sample distance, and  $U$  is the electric-potential difference between the tip and the sample. By substituting the voltage of Equation (2.7) into Equation (2.8), it follows that only one term depends directly on the excitation frequency  $f_{KPFM}$ :

$$F_{f_{KPFM}} \propto 2U_{AC}(U_{DC} - U_{CPD}) \cos(2\pi f_{KPFM}t) . \quad (2.9)$$

Accordingly, the contact potential can be determined by applying an equal DC voltage that minimizes the  $f_{KPFM}$ -modulated component. In practice, this is achieved by detecting the cantilever modulation at  $f_{KPFM}$  by an additional lock-in amplifier. The phase between excitation and detected modulation should be adjusted in such a way that the pure cosine (or sine) part<sup>3</sup> is detected by the lock-in amplifier. This value,  $X_{KPFM}$ , becomes zero for  $U_{DC} = U_{CPD}$ . Since  $U_{CPD}$  is typically not constant while scanning, a feedback loop is applied that minimizes  $X_{KPFM}$ .

---

<sup>3</sup>Taking into account Euler's equations,  $X = \text{Re}(z) = A \cos \phi$  and  $Y = \text{Im}(z) = A \sin \phi$ , where  $A$  is the amplitude and  $\phi$  is the phase of the lock-in amplifier, respectively.

## 2.2 Infrared nanospectroscopy

Infrared nanospectroscopy, in the sense of scattering scanning near-field infrared microscopy (s-SNIM), enables imaging and spectroscopy of surfaces<sup>4</sup> at the nanometer scale, far beyond the classical diffraction limit [33]. In this section, the concept of s-SNIM is introduced both as experimental concept and by an analytic theoretical approach. Generally, s-SNIM is an AFM-based technique providing a wavelength-independent spatial resolution in the order of the AFM tip's apex diameter, i. e. about 10 nm to 50 nm.

### 2.2.1 The diffraction limit

Classical optical microscopy is basically limited in its resolution by the wave nature of light, i. e. by diffraction. The most famous expression of the resolution limit in classical optical microscopy has been formulated by Ernst Abbe in 1873 [34]:

$$x_{\min} = \frac{\lambda}{2n \sin(\delta)} \approx \frac{\lambda}{2}, \quad (2.10)$$

where  $x_{\min}$  is the minimal observable (lateral) distance between two lines of a grating,  $\lambda$  is the wavelength,  $n$  is the refractive index of the immersion medium, and  $\delta$  is half of the opening angle of the objective (see Figure 2.4). Equation (2.10) is strictly valid for an optical microscope with condenser, otherwise the factor 2 in the denominator is omitted.

Even though other expressions of the resolution limit exist, such as the Rayleigh criterion [35] or the full width at half maximum (FWHM) of the point spread function [36], the wavelength dependence marks a fundamental limitation of classical microscopy. This becomes particularly clear for the wavelength range of infrared and THz radiation, which spans about 1  $\mu\text{m}$  to 300  $\mu\text{m}$ . Alternative concepts of microscopy can achieve sub diffraction resolution. They are referred to as super-resolution techniques based on confocal optical microscopy, such as stimulated emission depletion (STED) microscopy [37, 38]. However, STED probes light via fluorescence and thus requires fluorescent markers in the sample.

---

<sup>4</sup>Also buried structures beneath the surface can be observed down to a depth of several 10 nm, depending on the material properties [27–32].

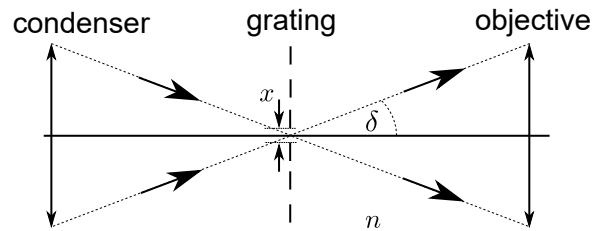


Figure 2.4: Simplified beam path of a classical optical microscope with objective and condenser.

### 2.2.2 Scattering scanning near-field infrared microscopy

Figure 2.5 shows the two common concepts of scanning near-field optical/infrared microscopy. Historically, the first approach was to utilize a sub-wavelength aperture that is significantly smaller than the wavelength, scanning the sample in proximity to the surface. Accordingly, this technique is called aperture scanning near-field optical microscopy (a-SNOM) and yields different possibilities of illumination and collection of light [see Figure 2.5 (a)]. In practice, aperture tips consist of silicon or glass and are covered by a thin metal layer with an about 100 nm wide opening at the tip's end. The spatial resolution is then given by the size of the aperture, which beats the diffraction limit. The main drawback of a-SNOM is that the transmitted intensity through the aperture is reduced by orders of magnitude, when the aperture is smaller than  $\lambda/2$  [39]. This prevents the effective use of a-SNOM in combination with mid-infrared or even THz radiation.

Alternatively, scattering scanning near-field optical microscopy (s-SNOM) [33, 40, 41] is based on a conventional (metallized) AFM tip in proximity to the sample that is illuminated from the side [see Figure 2.5 (b)]. The backscattered light from the tip-sample system is collected and recorded during the AFM scan. In contrast to a-SNOM, there is no wavelength-dependent cut-off for the laser intensity. The spatial resolution in s-SNOM mainly depends on the effective size of the scatterer, i. e. the apex diameter of the AFM tip, and is, most importantly, wavelength independent. To emphasize that we work exclusively in the infrared wavelength range the term s-SNIM<sup>5</sup> will be used in the following.

While a-SNOM is conceptually closer to classical optical microscopy, contrast

<sup>5</sup>In fact, s-SNIM and s-SNOM describe exactly the same principle.

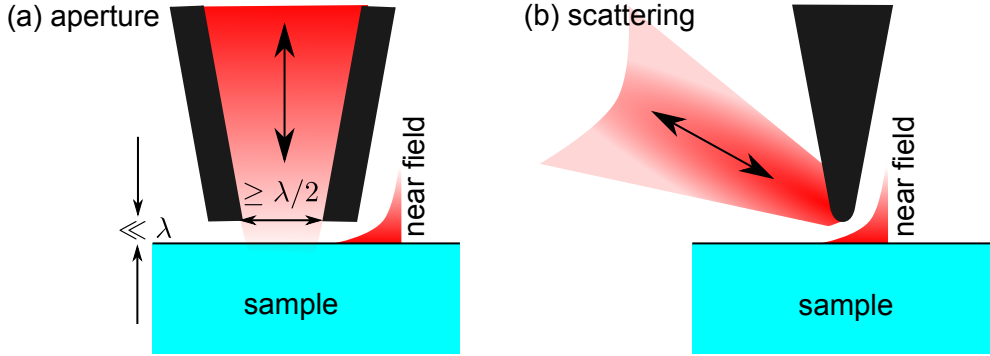


Figure 2.5: The two main concepts of SPM-based microscopy: (a) aperture scanning near-field optical microscopy (a-SNOM) and (b) scattering scattering scanning near-field optical microscopy (s-SNOM)

generation and therefore the evaluation of s-SNIM images and spectra is more complex, as we will discuss in the following chapter. Nevertheless, only s-SNIM enables a truly wavelength-independent operation on the nanometer scale. For instance, a spatial resolution of about  $\lambda/4600$  at  $\lambda = 230 \mu\text{m}$  ( $\hbar\omega = 5.4 \text{ meV}$ ) can be achieved [42]. S-SNIM is typically based on AFM using a conventional metallized tip. Hence, different kinds of complementary techniques, such as KPFM or PFM, can be applied at the same sample position. Thus, in addition to the actual s-SNIM measurement, comprehensive information about the topography, the surface potential, or the ferroelectric domain structure can be obtained.

### 2.2.3 Point-dipole model

The point-dipole model (PDM) has been introduced to describe s-SNIM by Knoll and Keilmann in 2000 [40] and provides an analytic approach to the contrast formation in s-SNIM. In the PDM, the probe is approximated by a homogeneous, isotropic sphere with the radius  $a$  at a distance  $z$  to the sample surface (see Figure 2.6). The sphere should be much smaller than the wavelength and any motion of the sphere much slower than the frequency of the radiation. Hence, the electrostatic limit can be assumed and the scattering of the sphere can be treated in the Rayleigh limit of Mie theory.

An external applied electric field  $\vec{E}_0$  induces a electric polarization of the probe (in air/vacuum) with a dipole moment

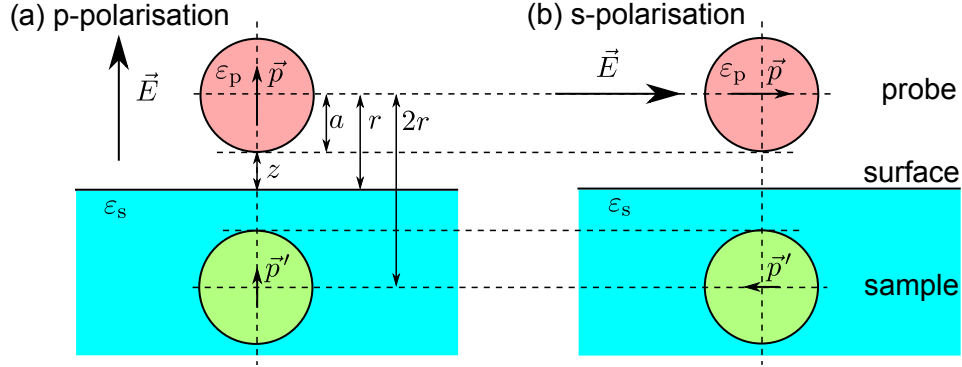


Figure 2.6: Geometry of probe dipole  $\vec{p}$  and image dipole  $\vec{p}'$  used in the PDM for (a) p-polarized electric field ( $\perp$ , perpendicular to the surface) and (b) s-polarized electric field ( $\parallel$ , parallel to the surface).

$$\vec{p} = \epsilon_0 \alpha \vec{E}_0, \quad (2.11)$$

where  $\epsilon_0$  is the vacuum permittivity and  $\alpha$  is the probe polarizability. The latter is expressed by

$$\alpha = 4\pi a^3 \frac{\epsilon_p - 1}{\epsilon_p + 2}, \quad (2.12)$$

where  $\epsilon_p = \epsilon_p' + i\epsilon_p''$  is the probe permittivity. Equation (2.12) contains the so-called Fröhlich resonance for  $\epsilon_p' = -2$  and  $\epsilon_p'' \ll 1$  [43]. For a metal probe, where  $\epsilon_p'$  gains a negative value in the IR, i. e.  $\epsilon_p' \ll -1$ , Equation (2.12) can be approximated by  $\alpha \approx 4\pi a^3$ . Generally, the electric field of a point dipole with a dipole moment  $\vec{p}$  is described by [44]

$$\vec{E}_{\text{dipole}}(\vec{r}) = \frac{1}{4\pi\epsilon_0} \left( 3 \frac{\vec{p} \cdot \vec{r}}{r^5} \vec{r} - \frac{1}{r^3} \vec{p} \right), \quad (2.13)$$

where  $\vec{r} = \vec{0}$  is the point-dipole origin. In the following, to simplify the further derivation, we consider the field along the  $z$ -direction through the center of the sphere. The electric field perpendicular to the surface [see Figure 2.6 (a)] hence is

$$E \vec{e}_z = \frac{p}{2\pi\epsilon_0 r^3} \vec{e}_z. \quad (2.14)$$

If the sphere approaches the surface of a sample, the dipole field changes. The

field distribution of the point dipole in proximity to a surface can be treated by introducing an image dipole  $p' = \beta p$  in the sample at the distance  $2r$  with respect to the probe dipole with

$$\beta = \frac{\varepsilon_s - 1}{\varepsilon_s + 1}, \quad (2.15)$$

where  $\varepsilon_s = \varepsilon'_s + i\varepsilon''_s$  is the sample permittivity. Equation (2.15), i. e.  $\beta$ , is also called sample response function. The field of the induced image dipole at the distance  $2r$  modifies the probe's dipole moment to

$$p = \varepsilon_0 \alpha \left[ E_0 + \frac{p'}{2\pi\varepsilon_0(2r)^3} \right] \quad (2.16)$$

$$= \varepsilon_0 \alpha E_0 + \frac{\alpha\beta p}{16\pi r^3}. \quad (2.17)$$

By solving the latter for  $p$  we get:

$$p = \frac{\alpha}{1 - \frac{\alpha\beta}{16\pi r^3}} \varepsilon_0 E_0. \quad (2.18)$$

In the far field, where the signal is detected and the distance between dipole and image dipole is negligible, a superposition of dipole and image dipole fields yields the effective total polarization

$$p_{\text{tot}} = p + p' = (1 + \beta)p = \varepsilon_0 \alpha^{\text{eff}} E_0. \quad (2.19)$$

Hence, an effective polarizability for p-polarization [ $\perp$ , Figure 2.6 (a)] of the coupled probe-sample system can be deduced by considering Equation (2.18):

$$\alpha_{\perp}^{\text{eff}} = \frac{\alpha(1 + \beta)}{1 - \frac{\alpha\beta}{16\pi(a+z)^3}}, \quad (2.20)$$

where  $a$  is the probe (sphere) radius and  $z$  is the distance from the surface to the sphere (see Figure 2.6).

For s-polarization, where the electric field  $E_0$  is oriented parallel to the surface [ $\parallel$ , Figure 2.6 (b)], the image dipole  $|\vec{p}'| = -\beta|\vec{p}|$  is oriented opposite to the probe dipole. According to Equation (2.13), the electric field of the probe dipole is now



$$E\vec{e}_x = -\frac{p}{4\pi\epsilon_0 r^3}\vec{e}_x. \quad (2.21)$$

Following the same steps as for p-polarization, the effective polarizability for s-polarization is then given by:

$$\alpha_{\parallel}^{\text{eff}} = \frac{\alpha(1-\beta)}{1 - \frac{\alpha\beta}{32\pi(a+z)^3}}. \quad (2.22)$$

The scattering cross section  $C_{\text{sca}}$  and the absorption cross section  $C_{\text{abs}}$  of the coupled probe-sample system can be deduced by applying Mie theory [45] in the Rayleigh limit, i. e. assuming the probe is much smaller than the wavelength ( $a \ll \lambda$ ) [40, 46, 47]:

$$\sigma_{\text{sca}} = \frac{k^4}{6\pi} |\alpha^{\text{eff}}|^2 \quad (2.23)$$

$$\sigma_{\text{abs}} = k\text{Im}(\alpha^{\text{eff}}), \quad (2.24)$$

where  $\alpha^{\text{eff}}$  is the effective polarizability for p-polarization (2.20) or s-polarisation (2.22), respectively. Note that in a realistic scenario the light is neither purely s- nor p-polarized, but contains contributions of both due to the oblique angle of incidence. Since we usually measure with (mostly) p-polarized light, we only consider the polarizability  $\alpha_{\perp}^{\text{eff}}$  in the following.

Figure 2.7 demonstrates how the resonance of the effective polarizability  $\alpha_{\perp}^{\text{eff}}$  behaves qualitatively. Here, we simplify the probe polarizability as given by Equation (2.12) to  $\alpha \approx 4\pi a^3$ , i. e. we assume a nonresonant probe. Generally, the dipole model predicts a resonance of  $\alpha_{\perp}^{\text{eff}}$  for a slightly negative real part of the sample permittivity of about  $\epsilon'_s \in (-3, -1)$ . As depicted in Figures 2.7 (a) and (b), for an increasing imaginary part  $\epsilon''_s$  the resonance width broadens and the maximum value  $\text{Max}(\alpha_{\perp}^{\text{eff}})$  [red curve in Figure 2.7 (b)] strongly decreases. Also the position of the maximum  $\epsilon'_{s,\text{max}}$  [blue curve in Figure 2.7 (b)] shifts towards lower values. A more realistic case, where both  $\epsilon'_s$  and  $\epsilon''_s$  change at the same time, depending on a physical model, will be discussed later (see Section 2.2.5).

Furthermore, the resonance is sensitive to the probe-sample distance  $z$  [48], as illustrated in Figures 2.7 (c) and (d). For a fixed  $\epsilon''_s$ , the maximum value  $\text{Max}(\alpha_{\perp}^{\text{eff}})$

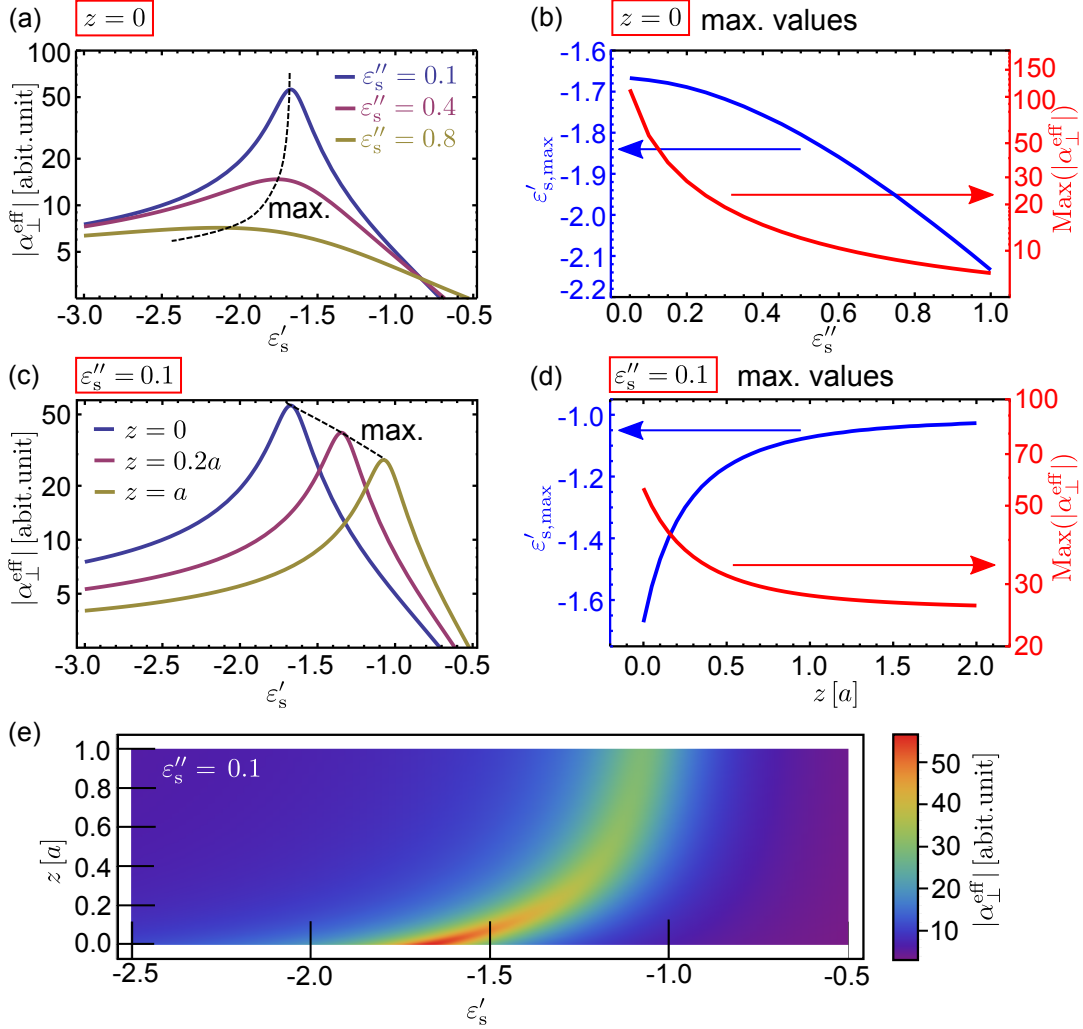


Figure 2.7: Resonance behavior of the effective polarizability  $\alpha_{\perp}^{\text{eff}}$  based on Equation (2.20): (a) Sample resonance for different imaginary parts of the permittivity  $\epsilon''$  at a fixed probe-sample distance ( $z = 0$ ). (b) Maximum values  $\text{Max}(|\alpha_{\perp}^{\text{eff}}|)$  and their positions  $\epsilon'_{s,\text{max}}$  according to (a). (c) Sample resonance for different tip-sample distances  $z$  at a fixed  $\epsilon''$ . (d)  $\text{Max}(|\alpha_{\perp}^{\text{eff}}|)$  and  $\epsilon'_{s,\text{max}}$  according to (c). (e) Map of the resonance for a fixed  $\epsilon''$ .

decreases rapidly, whereas the maximum position  $\varepsilon'_{s,\max}$  increases and asymptotically approaches  $-1$ . The map in Figure 2.7 (e) again emphasizes the resonance behavior depending both on  $\varepsilon'_s$  and  $z$ . In particular, it becomes clear that the signal does not automatically have to be largest at the smallest distance. Such maps can be measured experimentally, for example by retracting the tip from the surface and varying the photon energy (and thus  $\varepsilon_s$ ). This results – in combination with the higher harmonic demodulation technique (see Section 2.2.5) – in so-called lobes within the retract maps for strong sample resonances (e. g. phonon resonances [49]), which demonstrates the accuracy of the PDM.

The PDM has been applied successfully in various studies [33, 50–53] to explain experimental s-SNIM results. In addition to the PDM, extended or alternative models have been developed for specific cases or a more realistic description, for example:

- The finite-dipole model [54] is an alternative analytic approach, where the point dipole is replaced by a finite dipole consisting of point charges. This approximation fits better to the real probe shape, which is highly anisotropic, i. e. elongated along the  $z$  axis. Hence, the finite dipole model yields a higher precision in predicting the quantitative behavior of s-SNIM. On the other hand, the resulting effective polarizability is much less intuitive and contains additional empirical parameters, although it shows the same qualitative results as the PDM.
- The sample permittivity  $\varepsilon_s$  in Equation (2.15) is assumed to be isotropic. An extension of the PDM towards anisotropic permittivities is introduced in [47]. This model becomes important to explain and quantify the contrast of optically anisotropic materials, for example ferroelectric domains excited resonantly at their reststrahlenband [55].

### 2.2.4 Signal detection

In s-SNIM, part of the backscattered intensity  $I$  from the tip gets detected in the far field regime. Since the PDM does not contain the angular distribution of the scattered light and the probe is, realistically, an elongated antenna-like conductor, the exact scattered intensity cannot be deduced within this simple

analytic frame. Hence, it is necessary to perform s-SNIM measurements with respect to a reference (for example Au) with a well known permittivity in order to predict or interpret s-SNIM data.

The detected intensity  $I$  contains both background contributions  $E_{\text{bg}} = E_{\text{bg},0}e^{i\phi_{\text{bg}}}$  from the cantilever and scattering particles close to the probe, as well as the actual scattered contribution  $E_{\text{sca}} \propto \alpha^{\text{eff}}E_0 \equiv |\alpha^{\text{eff}}|e^{i\phi_{\text{sca}}}E_0$  ( $E_0 \in \mathbb{R}$ ) described by the PDM, as depicted in Figure 2.8. The intensity measured in the far field by the detector is then:

$$\begin{aligned} I &\propto |E|^2 = |E_{\text{bg}} + E_{\text{sca}}|^2 \\ &\propto |\alpha^{\text{eff}}|^2 E_0^2 + E_{\text{bg},0}^2 + 2E_0 E_{\text{bg},0} |\alpha^{\text{eff}}| \cos(\phi_{\text{bg}} - \phi_{\text{sca}}). \end{aligned} \quad (2.25)$$

Since the background signal is assumed to be much stronger than the scattered signal from the probe-sample system, i. e.

$$|\alpha^{\text{eff}}|^2 E_0^2 \ll 2E_0 E_{\text{bg},0} |\alpha^{\text{eff}}|, \quad (2.26)$$

the first term in (2.25) can be neglected. The second term should be large, but gets canceled out by the demodulation technique, which is described in the next section. Hence, the third term dominates the measured intensity, which has mainly two consequences:

- The measured detector signal contains both amplitude  $|\alpha^{\text{eff}}|$  and phase  $\phi_{\text{sca}}$  of the tip-sample dipole interaction. The exact contributions of both are, however indistinguishable and can lead to difficulties in the data interpretation.
- The background field amplitude  $E_{\text{bg},0}$  and phase  $\phi_{\text{bg}}$  are generally unknown. In particular phase variations due to scattering objects on the surface may have a strong impact on the signal and can lead, for instance, to strong interference patterns.

The aforementioned way of signal detection is commonly referred to as non-interferometric or self-homodyne detection [56]. In order to extract both optical amplitude and phase information it is common to use a setup based on a Michelson

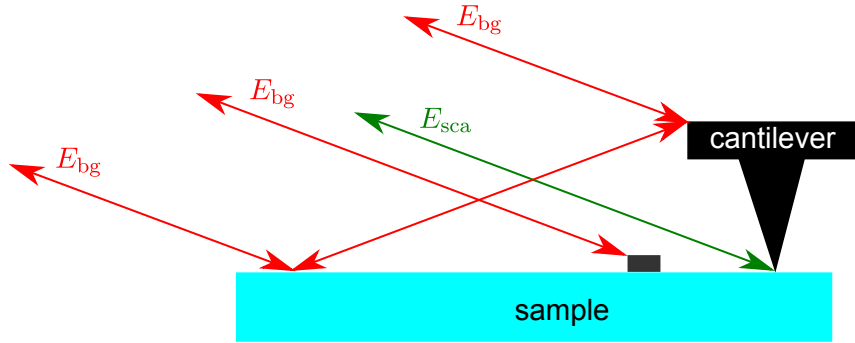


Figure 2.8: Possible background scattering contributions  $E_{bg}$  and the field scattered from the probe-sample system  $E_{sca}$ , containing the near-field information.

interferometer, where one arm is the s-SNIM path and the other arm is modulated in a controlled fashion. This detection scheme is referred to as pseudo-heterodyne detection [57]. The latter, however, requires an extremely stable (usually continuous wave) laser. Thus, an implementation of pseudo-heterodyne detection in combination with a free-electron laser (FEL) has not been achieved yet.

### 2.2.5 Higher harmonic demodulation and contrast

Since the scattered near-field contribution is typically much smaller than the background, a technique to suppress the latter contribution is required. This is achieved practically by a periodic modulation of the probe-sample distance

$$z(t) = z_0 + A[1 + \cos(2\pi\Omega t)] , \quad (2.27)$$

where  $z_0$  is the minimal distance,  $A$  is the oscillation amplitude, and  $\Omega$  is the frequency. Since the scattered electric field rapidly varies with increasing tip-sample distance  $z$  in a nonlinear fashion, the modulated scattered signal is not purely harmonic but contains higher order frequencies  $n\Omega$ ,  $n \in \mathbb{N}$  of the probe oscillation.

These higher orders can be calculated numerically by deducing the  $n^{\text{th}}$ -harmonic Fourier component of  $I$ :

$$\begin{aligned}
I_n &\propto \int_0^{1/\Omega} dt I_{\text{det}} e^{-2\pi i n \Omega t} \\
&\propto \int_0^{1/\Omega} dt |\alpha^{\text{eff}}| \cos(\phi_{\text{bg}} - \phi_{\text{sca}}) \cos(2\pi n \Omega t) ,
\end{aligned} \tag{2.28}$$

This so-called higher harmonic demodulation technique can be applied easily in the experiment by using tapping-mode AFM (see Section 2.1.1) and a lock-in amplifier for the optical signal detection. The demodulation helps to efficiently extract the near-field contribution from the total signal, since the far-field contribution typically behaves linear at small tip-sample distance [40, 47]. Note, however, that the detector signal is in general a complicated interference of the background with the scattered near-field signal, as explained in the previous Section 2.2.4. Thus, also the higher harmonic signals  $I_{n\Omega}$  may contain unwanted background contributions, for example the background phase  $\Phi_{\text{bg}}$ .

Finally, to compare the spectral response or evaluate the contrast of an s-SNIM image, we have to relate the signals to a reference with a well-known permittivity yielding the signal  $s_{n\Omega,\text{ref}}$ . Deviding both signals eliminates all unknown prefactors and defines the contrast to

$$\frac{s_{n\Omega}}{s_{n\Omega,\text{ref}}} = \frac{|I_{n\Omega}|}{|I_{n\Omega,\text{ref}}|} , \tag{2.29}$$

where  $s_{n\Omega}$  is the  $n^{\text{th}}$  harmonic demodulated s-SNIM signal and  $I_{n\Omega}/I_{n\Omega,\text{ref}}$  are the  $n^{\text{th}}$  Fourier components of sample and reference, respectively, according to Equation (2.28).

Figure 2.9 exemplarily shows the spectral contrasts according to two common analytic models, which describe the frequency dependence of the infrared permittivity. The model applied in Figure 2.9 (a) is the Drude model and is described by

$$\varepsilon_s(\omega) = \varepsilon_{\text{optic}} \left( 1 - \frac{\omega_{\text{pl}}^2}{\omega^2 + i\omega\gamma} \right) , \tag{2.30}$$

where  $\varepsilon_{\text{optic}}$  is the high-frequency permittivity,  $\omega_{\text{pl}}$  is the plasma frequency and  $\gamma$  is the damping factor. The Drude model is commonly used to describe the optical

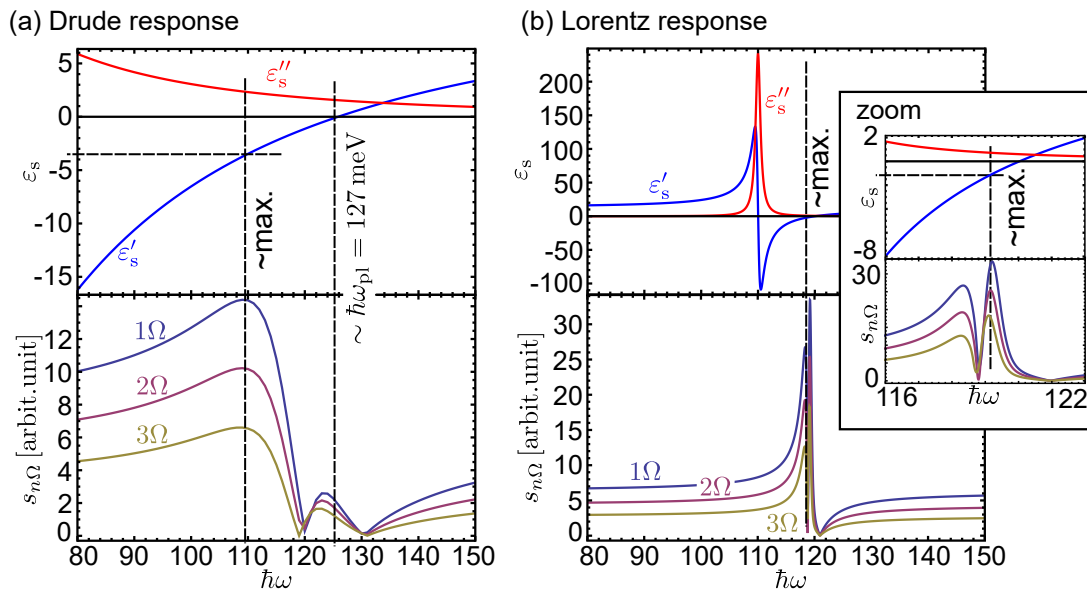


Figure 2.9: Exemplary resonances of the sample permittivity  $\varepsilon_s$  and simulated higher harmonic signals  $s_\Omega$  according to Equation (2.28) for: (a) A sample permittivity  $\varepsilon_s$  according to the Drude model (free carrier response). (b) A permittivity  $\varepsilon_s$  according to the Lorentz model (phonon response).

and infrared response of free charge carriers in metals or (doped) semiconductors (see Section 4.2.1). Figure 2.9 (a) shows both the real part  $\varepsilon'_s$  (blue) and imaginary part  $\varepsilon''_s$  (red) for  $\varepsilon_{\text{optic}} = 11.5$ ,  $\omega_{\text{pl}} = 127$  meV, and  $\gamma = 17$  meV. For  $\gamma \ll \omega_{\text{pl}}$ , the zero crossing of the real part  $\varepsilon_s = 0$  is close to  $\omega = \omega_{\text{pl}}$ . However, the maximum of all demodulation orders  $s_{n\Omega}$ ,  $n = 1, 2, 3$  is at significantly lower photon energies, here for example at about  $\omega = 110$  meV according to the s-SNIM resonance conditions discussed in Section 2.2.3. The s-SNIM resonance is, in our example, spectrally broad due to the relatively large imaginary part  $\varepsilon''_s > 1$ . Another characteristic in this case is that  $s_{n\Omega}$  is significantly larger for  $\omega \ll \omega_{\text{pl}}$  than for  $\omega \gg \omega_{\text{pl}}$  (similar to the reflectivity in the far field). The small dip at  $\omega \approx 125$  meV results from the phase contribution, which is mixed in the signal according to Equation (2.25). For instance, the dip does not appear if we only consider  $|\alpha^{\text{eff}}|^2$ . In fact, this demonstrates the uncertainty in non-interferometric detection induced by the unknown background phase  $\Phi_{bg}$ .

Figure 2.9 (b) shows another example of a common model for the infrared permittivity, the Lorentz model with

$$\varepsilon_s = \varepsilon_{\text{optic}} - \frac{(\varepsilon_{\text{static}} - \varepsilon_{\text{optic}})\omega_{\text{TO}}^2}{\omega^2 - \omega_{\text{TO}}^2 + i\omega\gamma}, \quad (2.31)$$

where  $\varepsilon_{\text{static}}$  is the low frequency permittivity,  $\omega_{\text{TO}}$  is the transversal optical (TO) phonon frequency, and  $\gamma$  is the (phonon) damping (for details see again Section 4.2.1). Here, the parameters are set to  $\varepsilon_{\text{optic}} = 11.5$ ,  $\varepsilon_{\text{static}} = 13.7$ ,  $\omega_{\text{TO}} = 110$  meV, and  $\gamma = 1$  meV. The real part  $\varepsilon'_s$  has two zero crossings: one at the maximum of the distinct peak of  $\varepsilon''_s$  and another at a higher phonon energy of  $\omega \sim 120$  meV. The sharp maximum of the demodulated signal  $s_{n\Omega}$  is close to the latter since here  $\varepsilon_s$  fulfills the resonance condition, i. e. a slightly negative  $\varepsilon'_s$  and a small  $\varepsilon''_s < 1$ . Similar to the case of Figure 2.9 (a), the resonance shows a second peak as depicted by the zoom inset.

## 2.2.6 Advantages and limitations of s-SNIM

s-SNIM has established itself as a versatile tool for infrared microscopy and infrared spectroscopy on the nanometer scale. However, some limitation and issues that can cause artifacts in or misinterpretation of the s-SNIM data, should be



kept in mind:

- s-SNIM requires a highly stable, low-noise light source that operates either in cw or high repetition rate pulsed mode,
- low signal and contrast for non-resonant excitation, in particular if  $\varepsilon'$  is between 1 and 10,
- contrast interpretation is usually not straightforward, i. e. the s-SNIM results cannot be compared directly to (far-field) transmission or reflection spectra without further techniques or data analysis,
- prone to artifacts due to parasitic background radiation; in particular, but not only in non-interferometric detection.

Finally, the clear benefits of the s-SNIM technique are listed below:

- + Wavelength-independent spatial resolution of typically 10 nm to 50 nm [40, 41],
- + buried structures may still be detectable to a certain degree (subsurface imaging, see for example references [27–32]), so-called superlenses enable even larger depth sensitivity at high spatial resolution [4, 5, 58–60],
- + complementary AFM techniques can be applied *in situ* (such as tapping-mode topography and KPFM) or sequentially (such as PFM) [61],
- + possible implementation of low-temperature conditions [10, 13, 16, 61, 62], time-resolved studies [14, 15, 63, 64] , etc.,
- + noninvasive and contactless probing, no need for special marker or conductive layers.

## 2.3 Infrared light sources

Almost all<sup>6</sup> s-SNIM measurements presented within this thesis are either performed with a CO<sub>2</sub> laser or a free-electron laser (FEL), which are both described in the following.

### 2.3.1 Carbon dioxide laser

The CO<sub>2</sub> laser is a narrow-band, continuous wave (cw) infrared source, tunable in the spectral range of 109 meV to 130 meV (9.6 μm to 11.4 μm, 877 cm<sup>-1</sup> to 1040 cm<sup>-1</sup>, 26 THz to 31 THz). However, there are gaps from 112.7 meV to 113.7 meV, 117 meV to 121.6 meV, and 125.2 meV to 126.5 meV, where no radiation is emitted.

The laser is based on the vibrational-rotational levels of the CO<sub>2</sub> molecule with an energy

$$\mathcal{E} = \mathcal{E}_{\text{vib}}(\nu_1, \nu_2, \nu_3) + \mathcal{E}_{\text{rot}}(J), \quad (2.32)$$

where  $\mathcal{E}_{\text{vib}}$  is the vibrational energy and  $\mathcal{E}_{\text{rot}}$  is the rotational energy [65] with the rotational quantum number  $J$ . The vibrational energy is given by

$$\mathcal{E}_{\text{vib}} = \sum_{i=1}^3 \left( v_i + \frac{1}{2} \right) h\nu_i, \quad (2.33)$$

where  $v_i = 0, 1, 2, \dots : \forall i$  are the vibrational quantum numbers, frequency  $\nu_1$  corresponds to the symmetric valence vibration (stretch),  $\nu_2$  to the bending vibration, and  $\nu_3$  to the antisymmetric valence vibration [Figure 2.10 (a)]. States with the particular quantum number  $v_1, v_2$ , and  $v_3$  are denoted as  $v_1 v_2 v_3$  states.

The water-cooled laser with a cavity length of about 1 m contains a gas mixture of CO<sub>2</sub>, N<sub>2</sub>, and He. First, the electron impact by gas discharge excites a long-living vibrational motion of the N<sub>2</sub> molecules [see Figure 2.10 (b)]. Collision and energy transfer of the excited N<sub>2</sub> molecules with the non-excited CO<sub>2</sub> molecules leads to a population of the CO<sub>2</sub> 001 state, which has a very long lifetime of about 4 s. Subsequently, spontaneous emission of radiation to the 100 or 020 states occurs, corresponding to 117 meV or 129 meV, respectively. Transitions

<sup>6</sup>Except for the external measurements in Section 4.4.2 that utilized a tunable MIR QCL.

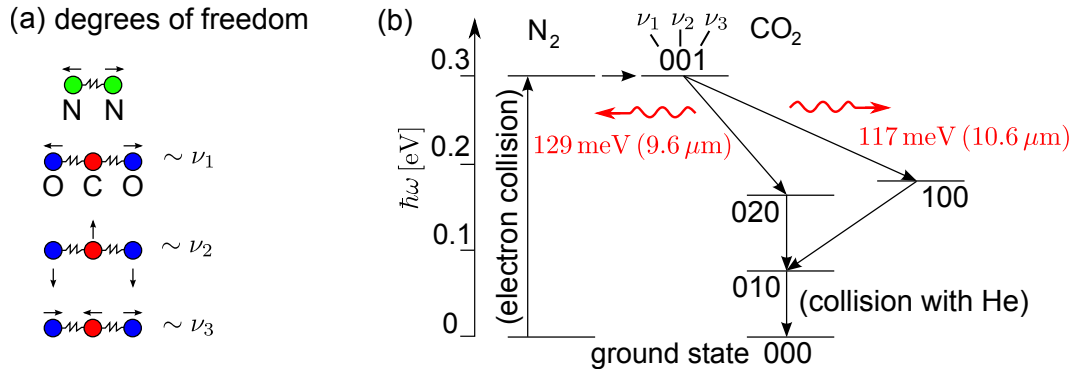


Figure 2.10: (a) Vibrational degrees of freedom of N<sub>2</sub> and CO<sub>2</sub> molecules. (b) Energy level scheme for a CO<sub>2</sub> laser. (adapted from [65])

between different types of vibrations are allowed due to the anharmonicity of the vibrations. Eventually, the CO<sub>2</sub> molecules are in a lower excited state 010 and relax to their ground state after collision with cold He atoms.

Beside the vibrational transition, the rotational energy changes with the selection rule  $\Delta J = \pm 1$  and additional rules for allowed states (for details see [65, pp. 270 sqq.]). Both vibrational and rotational states result in four branches (two each around the two main frequencies) with combs that include sharp spectral lines with line separations of about 0.25 meV. The linewidth is, for a low pressure of the gas mixture of less than 5 mbar, determined by Doppler broadening of the vibrational-rotational lines and in the order of  $10^{-6}$ .

To precisely select the emitted photon energy in the range of the allowed radiative transitions, the laser cavity contains a movable grating. The angle of the grating and hence the photon energy  $\hbar\omega$  is adjusted by a micrometer screw at the CO<sub>2</sub> laser. Furthermore, an active control loop of the cavity is included to ensure a high power stability of the laser by compensating thermal drift. The output power of the laser strongly depends on the selected wavelength and can reach several W. Since s-SNIM only requires laser powers in the order of 10 mW, the laser output is attenuated drastically by step attenuators. The emitted infrared radiation is linearly (p-)polarized and shows a well defined, Gaussian-shaped TEM<sub>00</sub> mode.

### 2.3.2 Free-electron laser

The FEL at the HZDR is part of the electron linear accelerator with high brilliance and low emittance (ELBE), and thus the FEL facility is also commonly referred to as FELBE. In fact, the latter consists out of two FELs that are sources of intense, narrow-band infrared radiation, both together covering the spectral range of 5 meV to 250 meV (5  $\mu\text{m}$  to 250  $\mu\text{m}$ ,  $40\text{ cm}^{-1}$  to  $2000\text{ cm}^{-1}$ , 1.2 THz to 60 THz).

ELBE provides highly-relativistic electron bunches with a kinetic energy of 5 MeV to 40 MeV and a maximal bunch charge of about 200 pC (using a superconducting photoelectron source). ELBE supports both a macro-pulse mode and a quasi-continuous mode with a repetition rate of typically 13 MHz. The latter mode is applied for all FEL-based s-SNIM measurements because it enables a reasonably short integration time ( $\sim 30\text{ ms}$ ) for the higher-harmonic demodulation technique (see Section 2.2.5), which is beneficial for s-SNIM imaging.

In an FEL, the relativistic electron bunches are directed into a periodic magnetic field of alternating direction, the so-called undulator, forcing them into a wiggling motion due to the Lorentz force (see Figure 2.11). Subsequently, the radially accelerated electrons emit electromagnetic radiation. The coherent amplification of the light field additionally requires a mirror cavity. The length  $l_c$  of the latter is chosen to match to the repetition rate  $f_{\text{rep}} = 13\text{ MHz}$  of the electron bunches, i. e. the infrared pulse should overlap with the next electron bunch after one round trip in the cavity. The interaction between the radiation field and the electron bunch *via* the ponderomotive force leads to the so-called microbunching [66]. Since the magnetic field of the light wave adds an additional Lorentz force to the electrons, which depends on the relative phase between electrons and the radiation, the electron bunch splits into compressed micro bunches. This effect ultimately explains the phase matching and the coherence of the emitted radiation.

FELBE actually consists of two FELs that contain different undulators, designed to cover two adjacent spectral regions: the so-called U37 for wavelengths from 5  $\mu\text{m}$  to 40  $\mu\text{m}$  (31 meV to 248 meV) and the U100 for 18  $\mu\text{m}$  to 250  $\mu\text{m}$  (5 meV to 69 meV). The names of the undulators indicate the undulator periods (i. e. the periods of the magnetic field) of 37 mm and 100 mm. The wide spectral overlap between the undulators is intended not only to prevent a gap but rather prevent



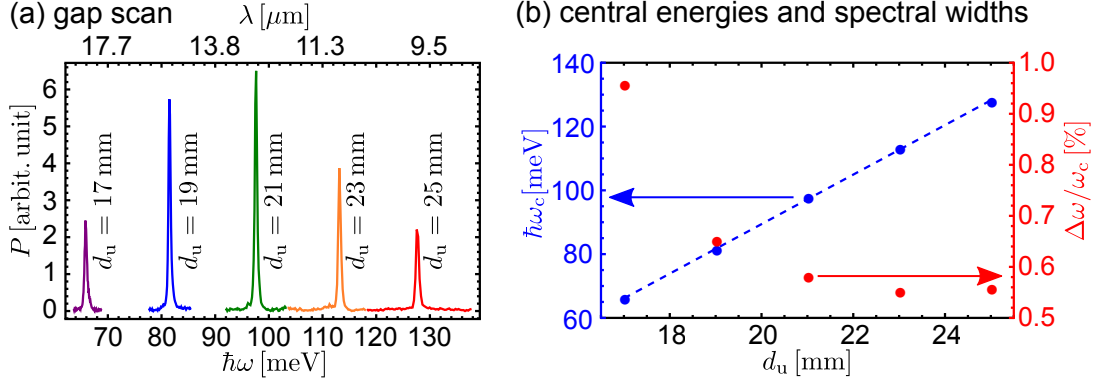


Figure 2.12: (a) FEL spectra for different undulator gap distances  $d_u$  using the U37 and a constant electron beam energy of  $\mathcal{E}_e = 28$  MeV. (b) Extracted central energies  $\hbar\omega_c$  and spectral bandwidths  $\Delta\omega/\omega_c$  [%] (FWHM).

where  $e$  is the elementary charge,  $B_0$  is the magnetic field strength, and  $m_e$  is the electron rest mass.

According to Equation (2.34) the wavelength  $\lambda$  (or photon energy  $\mathcal{E}_p = hc/\lambda$ ) can be tuned by the speed  $v_e$  of the relativistic electrons. In practice, the accelerator energy will be set by the ELBE operators to roughly match the desired photon energy with one of the undulators. Furthermore, the wavelength can be modified precisely over a smaller range by changing the undulator parameter  $K$ , i. e. *via* the magnetic field strength  $B_0$ .

This is practically achieved by varying the gap size within the undulator  $d_u$  (so-called gap scan). An exemplary gap scan is depicted in Figure 2.12 (a) that shows measured U37 FEL spectra for various gaps  $d_u$  at a fixed electron beam energy of  $\mathcal{E}_e = 28$  MeV. The narrow-band photon energy can be tuned over (at least) one octave from about 65 meV to 130 meV, as depicted by the blue points in Figure 2.12 (b). The photon energy scales nearly linear with  $d_u$  for the given range, as indicated by the fitted blue line. At the same time, the FWHM bandwidth  $\Delta\omega/\omega_c$  (red points) is in the order of 0.5% to 1% and tends to increase towards a more narrow gap, i. e. lower photon energies.

Beside the gap scan, it is also possible to precisely vary the cavity length, which is denoted as cavity detuning. The latter impacts not only the total emitted power but, moreover, the bandwidth and thus the peak intensity. Since the

emitted pulses can be considered as Fourier limited with an Gaussian envelope, the bandwidth scales inversely to the pulse duration. In our s-SNIM measurements we integrate over much longer time scales than the typical pulse duration of a few picoseconds and thus the exact pulse duration is usually not important. However, a more detailed description of the cavity detuning will be given later in Section 4.3.3, since Chapter 4 contains nonlinear observations of the s-SNIM signal.

### **Advantages and limitations**

The uniqueness of the FEL is certainly the tunability of coherent, intense radiation over a wide energy range within the so-called THz gap, which is partly not accessible by other (table-top) laser sources. Beside the advantages (+) mentioned in this section, many challenges (–) occur for the combination of s-SNIM and FEL:

- + Narrow band spectrum,
- + high fluence and high peak fields,
- + sufficiently high repetition rate of 13 MHz,
- + tunable over a wide spectral range in the mid- to far-infrared range without a (large) gap,
- restricted availability due to multiple user operation (typically about 72 h to 144 h per year per experiment),
- both non-symmetrical beam mode and steering of the beam can occur when the photon energy is tuned,
- power stability and signal-to-noise lower compared to, for example, the CO<sub>2</sub> laser,
- the last two points strongly depend on the wavelength and/or the current condition of the FEL.





# 3 Infrared nanospectroscopy at cryogenic temperatures

In this chapter, we present a scattering scanning near-field infrared microscope that operates in the temperature regime from room temperature down to  $T = 5$  K. In combination with the free-electron laser (FEL) at the Helmholtz-Zentrum Dresden-Rossendorf (HZDR), the apparatus enables nanospectroscopic investigations in terms of the local permittivity  $\varepsilon$  for a photon energy range from 5 meV to 250 meV. Moreover, Kelvin-probe force microscopy (KPFM) and piezoresponse force microscopy (PFM) reveal complementary information on the nanometer scale of the material under investigation.

The main results of this work have been published in Review of Scientific Instruments **89**, 033702 (2018) [61]. The development, set up and demonstration of the apparatus took place in close collaboration with the group of Prof. L. M. Eng from the Institute of Applied Physics, Technische Universität Dresden. Additional experimental details and comprehensive results on ferroelectric barium titanate ( $\text{BaTiO}_3$ ) at low temperatures can be found in the PhD thesis of J. Döring [55] and in related publications [62, 68, 69].

## 3.1 Introduction

The mid-infrared (MIR) and THz spectral range, also known as fingerprint region, is of high interest due to the diverse number of fundamental excitations, such as phonons, plasmons, molecular vibrations/rotations, and electronic excitations (e. g. intraband transitions). Since the energies in the THz frequency range correspond to low thermal energies, the investigation of many prominent effects in solid-state physics, such as superconductivity [70, 71], phase transitions

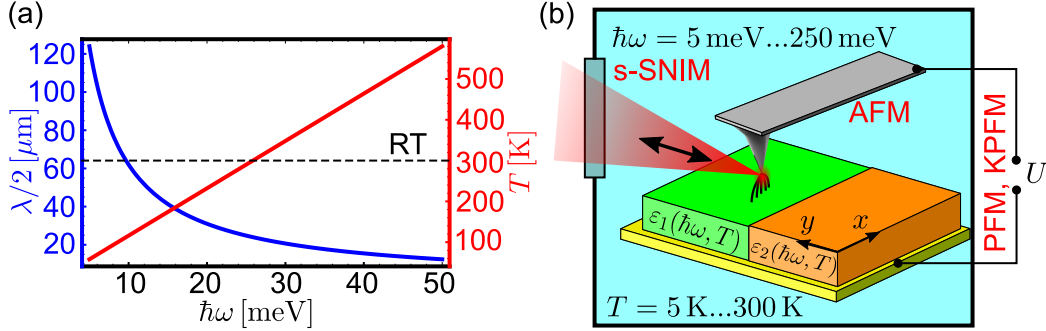


Figure 3.1: (a) For photon energies  $\hbar\omega < 27$  meV, the temperature corresponding to the thermal energy  $k_B T$  drops below 300 K. On the other hand, the resolution limit increases rapidly to the order of 100  $\mu\text{m}$  for decreasing  $E$ . (b) Scheme of the LT s-SNIM that includes atomic force microscopy (AFM), piezoresponse force microscopy (PFM), and Kelvin-probe force microscopy (KPFM) for complimentary information of the sample system. Adapted from [61].

in multiferroic materials [13, 62, 68], or low-energy transitions [72, 73], require a cryogenic environment. Because the spatial resolution of traditional infrared and THz spectroscopy is highly limited by diffraction (see Chapter 2.2.1), it is necessary to apply a near-field technique at low temperatures to study the above mentioned phenomena on the nanometer scale.

The red curve in Figure 3.1 (a) shows the photon energy  $\hbar\omega$  corresponding to the temperature, i. e. the thermal energy scaling with  $k_B T$ , where  $k_B$  is the Boltzmann constant. As can be seen, this temperature is well below room temperature for photon energies in the meV range. Therefore, cryogenic temperatures are advantageous or, in some cases, even indispensable to observe fundamental low-energy transitions. The resolution given by the diffraction limit of about  $\lambda/2$  (blue curve), however, decreases drastically for low photon energies to the order of 100  $\mu\text{m}$ . These correlations demonstrate the fundamental importance of performing FEL-based nanospectroscopy at cryogenic temperatures.

A conceptionally similar technique to low-temperature scattering scattering scanning near-field infrared microscopy (LT s-SNIM) is low-temperature scanning tunneling microscopy (STM) combined with laser illumination, which has been reported in various studies before. For instance, Wu et al. [74] investigated light-induced electron tunneling of single molecules by using an STM that oper-

ates at 9.5 K. Tip-enhanced Raman spectroscopy at low temperatures has been presented by Jiang et al. [75] and Zhang et al. [76]. Recently, the tracking of the intrinsic tunneling dynamics of single molecules was enabled by the combination of cryogenic STM with strong fs-pulses [77, 78].

Since the focus of this work is specifically on s-SNIM, the development of LT s-SNIM is sketched in the following. In 2011, Moldovan-Doyen et al. [79] used an s-SNIM-like approach at  $T = 100$  K to map the near-field of the emitted infrared-to-THz radiation from a active surface emitting quantum cascade laser based on photonic-crystal resonators. Yang et al. [16] investigated insulating domains in  $V_2O_3$  single crystals that nucleate around topographic defects by applying LT s-SNIM at about  $T = 200$  K. A detailed mapping of the  $V_2O_3$  insulator-to-metal transition has been demonstrated by McLeod et al. at about 160 K [13]. Very recently, Ni et al. [10] imaged plasmon polaritons in encapsulated graphene by s-SNIM at temperatures down to 60 K. Due to the reduction of dielectric losses, they reach a high intrinsic plasmonic propagation length exceeding 10  $\mu\text{m}$ .

In contrast to previous work, the performance of the LT s-SNIM presented here is demonstrated at temperatures below 10 K and is, to the best of our knowledge, the only existing LT s-SNIM system in combination with an FEL. Furthermore, different *in situ* electrical AFM techniques have been established, i. e. PFM and KPFM in order to gain complementary informations. In Figure 3.1 (b), the basic principle of our LT s-SNIM system is illustrated. Infrared radiation is focused on the AFM tip in close vicinity to the sample, which are both in a cryogenic environment and electrically connected to perform KPFM or PFM measurements. We extract the near-field radiation scattered by the tip to map the surface or take spectra at particular positions. Hence, we measure a contrast in the back-scattered signal depending on the complex permittivity  $\varepsilon$  as a function of e. g. the photon energy  $\hbar\omega$  or the temperature  $T$ .

## 3.2 Samples

For s-SNIM adjustment and as reference we use crystalline (100) Si that is covered by an 100 nm to 150 nm thick layer of evaporated Au. The Au layer is highly reflective for the complete infrared spectral range due to the permittivity  $\varepsilon'$  being

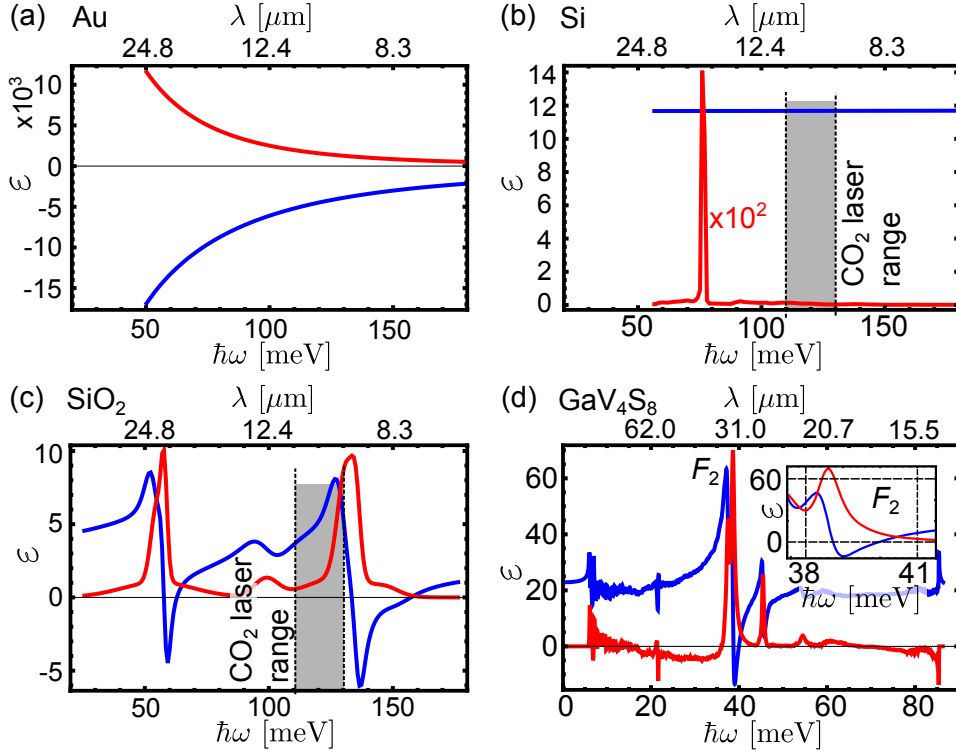


Figure 3.2: Real part  $\varepsilon'$  (blue) and imaginary part  $\varepsilon''$  (red) of the IR permittivity  $\varepsilon$  in dependence of the photon energy  $\hbar\omega$  (respectively wavelength  $\lambda$ ) for (a) evaporated Au (from [80]), (b) crystalline Si [81], (c) SiO<sub>2</sub>/fused silica [82], and (d) GaV<sub>4</sub>S<sub>8</sub> [83]. The inset in (d) is a zoom at the strongest of the  $F_2$  phonon modes [84]. All spectra (a)-(d) were measured at room temperature and fitted by an appropriate model (for details see the references).

negative as depicted in Figure 3.2(a). The high reflectivity also results in an increased signal of the interfering far-field contribution  $E_{bg}$  (see Section 2.2.2). Hence, the Au sample gives a reliably large, wavelength-independent s-SNIM signal for the complete FEL spectral range [42].

Beside planar Au, we investigate a structured Si/SiO<sub>2</sub> sample to demonstrate the functionality and resolution at  $T = 7$  K and  $\hbar\omega = 128$  meV. The Si/SiO<sub>2</sub> sample is commercially produced as part of dynamic random access memory (DRAM) technology. This sample was used to demonstrate the high resolution of the LT s-SNIM since it contains sub-wavelength sized structures and small topography steps at the same time (see Figure 3.3). The structure was produced by etching

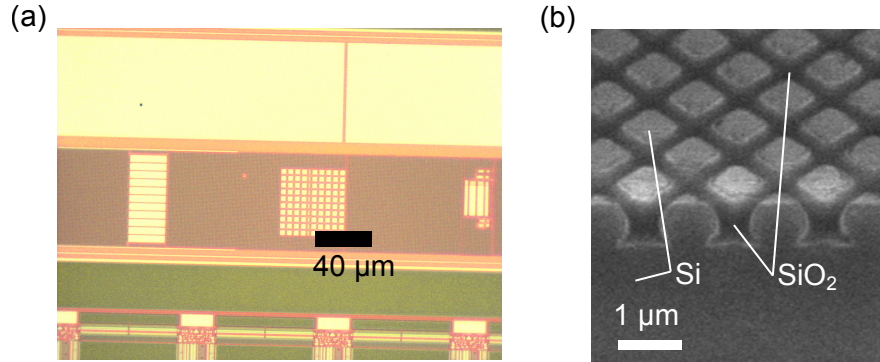


Figure 3.3: (a) Top-view optical microscopy image of the structured Si/SiO<sub>2</sub> sample that shows the structured areas with different sizes. (b) Side-view scanning electron microscopy image on a cleaved edge showing the SiO<sub>2</sub>-filled trenches.

into Si after lithographic masking. Subsequently, the trenches have been filled with amorphous SiO<sub>2</sub> by chemical vapor deposition. Afterwards, the lithographic mask was removed and the surface polished to achieve a smooth surface. The depth of the trenches and, accordingly, the thickness of SiO<sub>2</sub> is about 400 nm, which is much larger than the s-SNIM sensing depth of about 20 nm to 100 nm. Figure 3.2 (b) and (c) shows the permittivity spectra  $\varepsilon(\omega)$  of Si and SiO<sub>2</sub>, respectively. The Si spectrum is mostly flat within the MIR spectral range as shown by Figure 3.2 (b) and hence Si can serve as a reference for s-SNIM. In contrast, SiO<sub>2</sub> shows several strong phonon modes. At photon energies of about 62 meV and 150 meV, the permittivity matches the condition for a resonantly enhanced s-SNIM signal (see Section 2.2.2).

As a more intriguing example for the demonstration of our LT s-SNIM, we study the skyrmion-hosting, multiferroic material gallium vanadium sulfide (GaV<sub>4</sub>S<sub>8</sub>) [85, 86] that was grown by the chemical vapour transport method. GaV<sub>4</sub>S<sub>8</sub> undergoes a structural phase transition, the Jahn-Teller transition, at  $T_c = 42$  K where the unit cell geometry changes from a cubic phase at high temperatures to a rhombohedral phase at lower temperatures. In the low-temperature phase, ferroelectric domains are formed with electric polarizations pointing along any of the four  $\langle 111 \rangle$ -type axes. Here, we investigate the (111) surface of a GaV<sub>4</sub>S<sub>8</sub> crystal, which results in a lamellar domain pattern, observable in various *in situ* channels of the setup: KPFM, PFM, and s-SNIM. A detailed discussion of the

exact domain pattern is given in references [55, 87]. For the s-SNIM measurements, we choose a photon energy around the strongest phonon mode  $F_2$  [84] at about 39 meV [see Figure 3.2 (d)]. At this photon energy we expect a strongly enhanced s-SNIM signal and hence a contrast on the domain pattern due to optical anisotropy [49].

### 3.3 Experimental details

In this section, the components of the complex LT s-SNIM setup are explained in detail. This includes low-temperature atomic force microscopy (LT AFM), as well as the optical setup.

#### 3.3.1 Low-temperature atomic force microscopy

The custom-made LT AFM is based on a liquid helium bath cryostat<sup>1</sup> with optical access that contains an LT-compatible AFM<sup>2</sup>. In the following, only the most important aspects of the LT AFM will be explained. A detailed description that also includes calibrations and operational instructions can be found in [55, pp. 67 sqq.].

The bath cryostat [see Figure 3.4 (a)] consists of an outer reservoir for liquid nitrogen ( $\text{LN}_2$ ) and an inner reservoir. The latter can be filled either with  $\text{LN}_2$  or LHe, which depends on the minimal required temperature for the experiment (78 K for  $\text{LN}_2$  and  $\sim 5$  K for LHe). A high vacuum (pressure of about  $10^{-7}$  mbar) serves as thermal isolation in between the reservoirs, to the outer wall, and to the sample tube in the center. The sample tube contains the AFM and is filled with He exchange gas at a pressure of about 80 mbar at 300 K. To cool down the sample, first the inner reservoir is closed to build up overpressure. When the needle valve gets opened, the wall of the sample tube cools down due to cold liquid streaming through the heat exchanger. Subsequently, the temperature of both the He gas and the whole AFM inside the sample tube equalize. Optical access to the AFM is given by up to four pairs of openings, two of which each are

---

<sup>1</sup>Janis Research Company, type SVT-400.

<sup>2</sup>Attocube Systems AG.

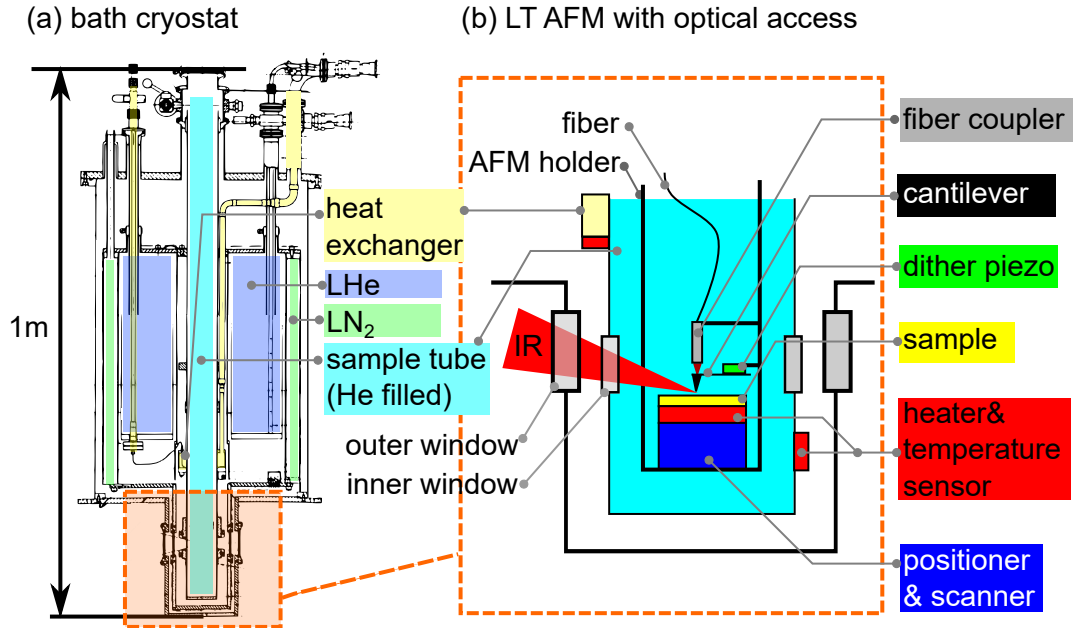


Figure 3.4: (a) Technical drawing of the LHe bath cryostat (adapted from [61]). (b) Schematic side view of the lower part, containing the AFM inside the sample tube.

equipped by a pair of windows in the presented work<sup>3</sup> (described in Section 3.3.3). In total, there are three pairs of heater/temperature-sensors inside the cryostat: one pair at the heat exchanger, one pair at the sample tube's wall at the height of the AFM, and one pair directly beneath the AFM's sample holder (see next paragraph). All pairs are connected to a temperature controller to achieve the thermal equilibrium with a precision of about 0.1 K.

The AFM is placed at the end of a rod cage (AFM holder) inside the about 1 m long sample tube, as depicted in Figure 3.4 (b). The motion of the AFM cantilever is detected by an optical-fiber interferometer ( $\lambda_{\text{fiber}} = 1310 \text{ nm}$ ), where the back-reflected light from the fiber's end interferes with the back-reflected light from the cantilever (see Section 2.1.1). This technique enables a direct, sub-nanometer precision measurement of the cantilever's relative position and movement. Because this interferometric system is very space efficient and there is no need for readjustment after cooling down the AFM, it is commonly used in cryogenic AFM systems. However, it only allows for the detection of the out-of-

<sup>3</sup>The other two pairs of openings are closed, but can be equipped with further windows.

plane movement of the cantilever and not for its torsion. A piezoelectric actuator (dither piezo) is used to adjust the distance of the cantilever with respect to the fiber. For tapping mode, the dither piezo also excites an oscillation of the cantilever at its resonance frequency  $\Omega$ , which is in the order of 150 kHz to 190 kHz for the cantilevers used in this work<sup>4</sup>. The peak-to-peak oscillation amplitude is typically set to 100 nm.

The sample stage that is located underneath the tip is a stack consisting of several elements for positioning and scanning. Three stick-slip positioner elements (lowest position in the stage) are used to move the lateral sample position and for rough approaching. All positioners have a maximum range of 5 mm with a minimal step size of 50 nm. Above the positioner, a piezoelectric *xyz* scanner is placed. The maximal lateral range of the scanner is  $(42 \times 42) \mu\text{m}^2$  and the maximal  $z$  range is 4  $\mu\text{m}$ . Note that all ranges given here are for room temperature and change (decrease) at lower temperatures. Additionally, a combined heater/temperature-sensor element is located in between the sample holder on top of the stage and the scanner below. The heater/temperature-sensor element is thermally isolated to the scanner by a thin teflon plate.

All electrical inputs and outputs of the LT AFM, as well as the optical fiber, are connected to electronic interconnection devices and controllers from *Attocube*. Subsequently, these signals will be passed to the actual AFM controller<sup>5</sup>. The *RHK* controller is operated by a network-connected computer via the associated *Rev9* software that records all data.

### 3.3.2 Optical setup

Figure 3.5 depicts the layout of the optical table and the beam path of the available laser sources to the LT s-SNIM. All optical elements are first adjusted by an expanded, collimated red laser diode (LD) with a beam diameter of about 3 cm. The red LD is in particular useful to roughly adjust the focus of the s-SNIM's off-axis parabolic mirror (OAM) to the AFM tip *via* its characteristic shadow image.

---

<sup>4</sup>We use non-contact AFM cantilevers PPP-NCLPt from *Nanosensors* that are coated with 25 nm of PtIr5 on both sides and have a pyramidal tip shape.

<sup>5</sup>*RHK R9* from RHK Technology.



The CO<sub>2</sub> laser (see Section 2.3.1), which is initially p-polarized (p-pol, green arrow/cross), is attenuated and the polarization is rotated by 90° to s-polarization (s-pol, blue arrow) using a  $\lambda/2$  plate in order to reach the same initial polarization as the FEL (see Section 2.3.2). A collinear overlap of the infrared lasers (FEL or CO<sub>2</sub> laser) with the well-aligned red laser is achieved by aligning the beam through two centered iris apertures (elliptical rings in Figure 3.5) by means of an infrared beam profiling camera. The FEL and the CO<sub>2</sub> lasers show different beam profiles as well as different beam divergences. The CO<sub>2</sub> laser has a symmetrical, Gaussian-like beam shape that expands in diameter along the beam path. Hence, the diameter of the CO<sub>2</sub> laser close to the beam splitter (BS) is about 4 cm. On the other hand, the FEL has a non-symmetrical shape and has a intermediate focus that is located roughly at the second iris aperture in Figure 3.5. The FEL beam diameter at the position of the BS is typically in the order of 1 cm to 3 cm, strongly depending on the wavelength.

Furthermore, the optical table contains mirror arrangements (named s-pol/p-pol) to set the polarization of the lasers. In the case of s-polarization (parallel to the table), the initial polarisation is retained. In the case of p-polarisation (perpendicular to the table), a periscope optic with 4 mirrors<sup>6</sup> rotates the polarization by 90°. We usually use p-polarization in our s-SNIM measurements, since it typically results in a higher near-field signal (see Section, 2.2.2) and thus better signal-to-noise ratio. However, s-polarization can be useful in some cases, for example to be sensitive to the in-plane domain anisotropy close to the phonon resonance of a ferroelectric material [47].

Note that we exclusively use non-dispersive optical elements, i. e. Au-coated mirrors covering the whole spectral range of the FEL. The only exception are the cryostat windows, which are discussed in the following section.

### 3.3.3 Low-temperature scattering scanning near-field infrared microscopy

The optical setup of the LT s-SNIM is depicted as blue part of Figure 3.5. The incoming beam is split up by a geometrical BS, an about 0.5 mm thick Si plate with an 150 nm thick Au coating. Half of the beam is guided to an infrared power

---

<sup>6</sup>For the sake of clarity, not all mirrors are shown in Figure 3.5.

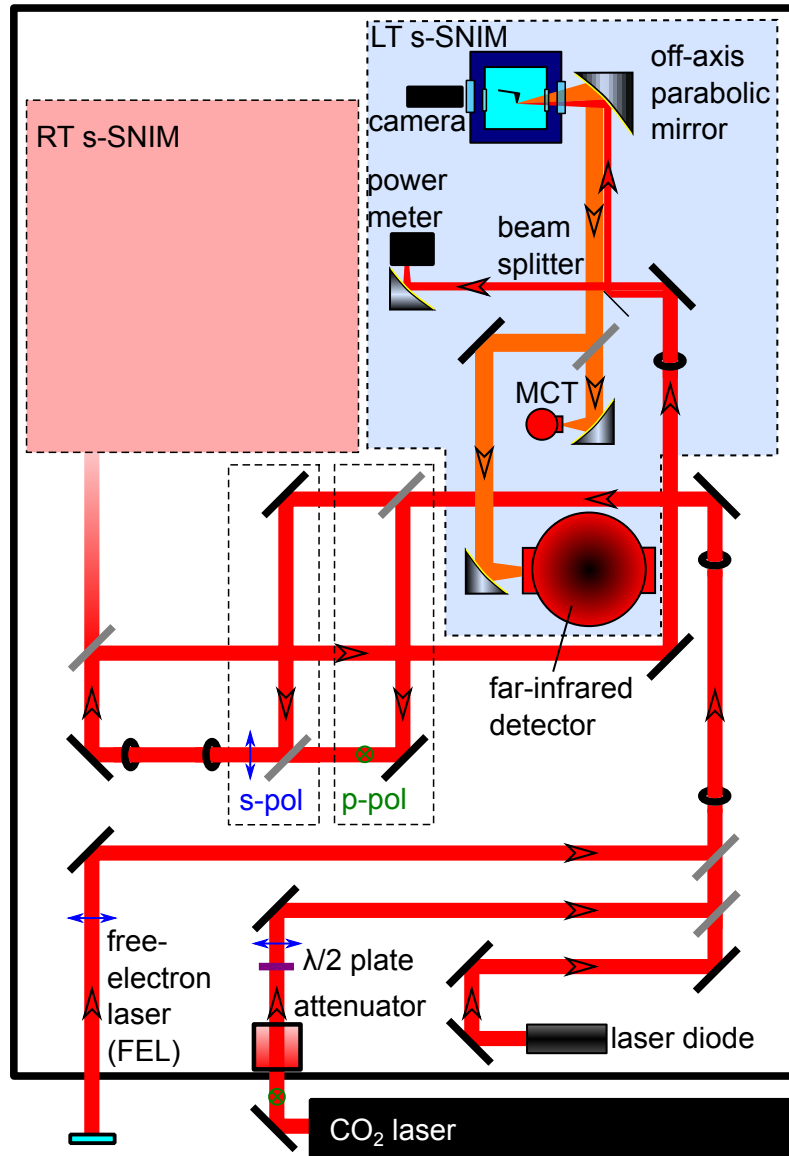


Figure 3.5: Layout of the optical table (not to scale). The fixed-mounted mirrors are indicated black, magnetic removable-mounted mirrors are grey. Iris apertures for alignment are represented by black ellipses. See both Sections 3.3.2 and 3.3.3 for details. The red area (room-temperature setup) is described in the next Chapter 4, Section 4.3.2.

meter, whereas the other part is focused on the AFM tip *via* a 3'' OAM. The effective focus length of the OAM is 6'', which results in a maximal numerical aperture of 0.17 for a perfectly collimated beam with 2'' beam diameter.

Table 3.1: Different window materials and their infrared transparency ranges (only for FEL spectral range) in units of wavelength  $\lambda$ , wavenumber  $\Lambda$ , photon energy  $\hbar\omega$  and frequency  $f$  (narrow-band absorptions within these ranges are not included).

Material	$\lambda$ [ $\mu\text{m}$ ]	$\Lambda$ [ $\text{cm}^{-1}$ ]	$\hbar\omega$ [meV]	$f$ [THz]
z-cut quartz	$> 50$	$< 200$	$< 25$	$< 6$
KRS-5	$< 50$	$> 200$	$> 25$	$> 6$
ZnSe	$< 18$	$> 550$	$> 69$	$> 17$
diamond	(complete FEL spectral range)			

On the way to the tip, the beam passes through two windows: the outer window and the inner window. The outer window can be exchanged easily between the materials quartz, ZnSe, or thallium bromo-iodide (KRS5), depending on the wavelength range of interest (see Table 3.1). Changing the inner windows is, however, much more difficult since it requires the disassembly of the lower cryostat part. Moreover, the inner window is also cooled down to  $T \geq 5$  K and has to be sealed with indium wire. Hence, a custom-made diamond window<sup>7</sup> is assembled as inner window since diamond transmits infrared and THz radiation over a wide spectral range. On the way to the tip (and also back) the radiation gets attenuated by a factor of about two due to the reflections on each of the four window surfaces. Hence, the power on the tip  $P_t = P/2$ , where  $P$  is the power measured on the power meter throughout this work. The position of the sample with respect to the tip is observed by a microscope camera through the two quartz windows at the opposite side of the cryostat.

The back-scattered radiation from the oscillating tip is collected by the same OAM and passes the BS once again. Afterwards, the scattered radiation is focused by another OAM either on an LN<sub>2</sub> cooled mercury cadmium telluride (MCT) detector<sup>8</sup> for the MIR spectral range ( $\hbar\omega > 46$  meV) or on a liquid-helium cooled

<sup>7</sup>Custom-made window with holder from *Diamond Materials GmbH*.

<sup>8</sup>*Teledyne Judson Technologies*, models *MCTJ15D5* - *MCTJ15D26*, depending on the wavelength.

far-infrared detector<sup>9</sup> ( $\hbar\omega < 52\text{ meV}$ ). The far-infrared detector contains two separate detectors for different spectral regimes, respectively: a Ga-doped Ge photoconductor (about 9.5 meV to 52 meV) and an InSb hot-electron bolometer ( $< 12\text{ meV}$ ). All detectors and their respective amplifiers are sufficiently fast to detect at higher harmonic frequencies of the tip  $n\Omega$ . This means for example 0.45 MHz to 0.57 MHz if we consider the third harmonic  $3\Omega$  of the cantilever resonance (for details see [88, pp. 85 sqq.]).

The pre-amplified output voltage of the detector is fed into the *R9* AFM controller. Here, the signal is processed by internal lock-in amplifiers that are synchronized to the excitation frequency of the tip  $\Omega$ . Hence, we record the demodulated optical signals at  $n\Omega : n = 1, 2, 3$  in terms of amplitudes  $s_{n\Omega}$  and phases  $\phi_{n\Omega}$ . Note that the amplitude  $s$  phase  $\phi$  we measure here do not correspond to the optical amplitude and phase as one would get for example in pseudo-heterodyne interferometric detection with a defined optical reference beam [57]. In the here applied self-homodyne detection,  $s$  represents a mixed signal of optical amplitude and phase (see Section 2.2.4), whereas  $\phi$  represents the phase with respect to the mechanical oscillation of the cantilever. As discussed in Section 2.2.2, measuring at higher-harmonic orders suppresses the far-field scattering contributions more efficiently. Since the signal strength, however, decreases rapidly with higher orders, which leads to a lower signal-to-noise ratio, we usually demodulate the 2<sup>nd</sup>-harmonic of  $\Omega$  and refer to  $s_{2\Omega}$  as s-SNIM signal.

### 3.3.4 Measurement modes and data acquisition

We typically apply three different modes for our measurements: 2D mapping of the surface, line scanning, and retracting from the sample.

In order to take a map of the sample surface [Figure 3.6 (a)], one line is scanned in forward and backward direction (fast axis,  $y$ ). After one line, the sample moves in the perpendicular direction (slow axis,  $x$ ), and scans the next line (and so on). A typical scan speed (fast axis) is  $3\text{ }\mu\text{m/s}$ , which results in a scan duration of 8.5 min for 128 lines and a scan range of  $6\text{ }\mu\text{m}$ . However, the duration of a scan can vary between a few minutes up to hours, strongly depending on the requirements of the particular measurement. Since all parameters (photon energy, power, ...)

<sup>9</sup>*QMC Instruments Ltd.*, model *QFI/3BI(2+Ge:Ga)*.

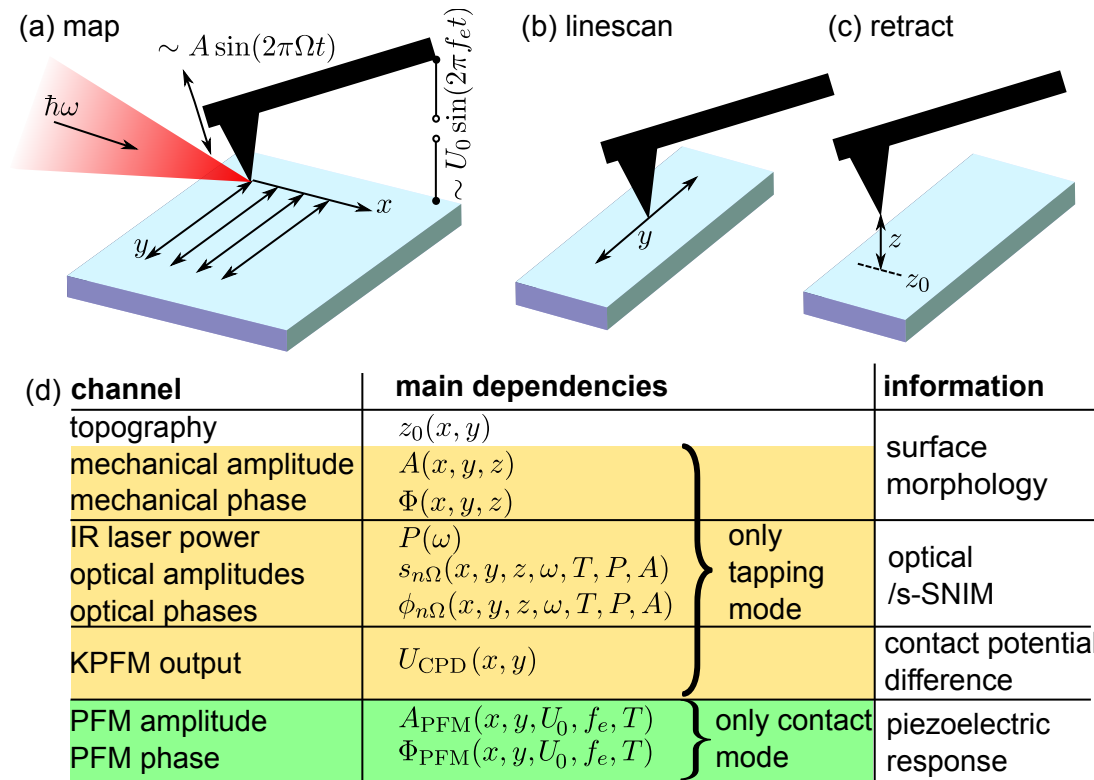


Figure 3.6: The most common measurement modes in s-SNIM: (a)  $(x, y)$  map of the surface, (b) line scan along  $y$  with fixed other axis  $x$ , (c) retract the sample from the tip. For each measurement, a set of channels (d) that contain complementary information is acquired.

are fixed during a scan, it may take very long to gain a full set of data with a full set of parameters.

For a line scan [Figure 3.6 (b)] the slow axis  $x$  is fixed. The  $y$  direction is scanned back and forth repeatedly, while another parameter (e.g.  $\hbar\omega$ ) is varied after a few lines. This mode is commonly used to measure a contrast dependence, where no full  $(x, y)$  information is required. Typically 5 or 10 lines are scanned for each parameter to increase the statistical evidence. Hence, the time for one parameter reduces to about 30 s to 60 s.

The last common measurement mode is to retract the sample from the oscillating tip [Figure 3.6 (c)] at a particular lateral position. This mode is mainly applied to investigate the tip-sample distance dependence of the s-SNIM amplitude and phase signals  $s_{n\Omega}$  and  $\Phi_{n\Omega}$ . When the sample retracts from the tip,

a characteristic nonlinear decay of  $s_{n\Omega}(z)$  for all  $n > 1$  within 10 nm to 100 nm should be visible (compare Section 2.2.2). The time to acquire a retract curve is typically 10 s to 30 s.

Figure 3.6 (d) lists all relevant channels recorded during a measurement. Whereas PFM only applies for contact mode, s-SNIM and KPFM are used simultaneously in tapping mode. Both in contact mode and in tapping mode, the topography is recorded *in situ* to the other channels. Figure 3.6 (d) also reveals the most important parameters of the channels (possible cross talk not included). Some parameters can also affect other parameters again: for example the temperature  $T$  underneath the tip can depend on the power  $P$  and photon energy  $\hbar\omega$  of the infrared laser, as we will discuss in Section 3.4.1.

## 3.4 Results and discussion

### 3.4.1 Performance and IR heating calibration

We demonstrate the LT s-SNIM performance on the structured Si/SiO<sub>2</sub> sample for a photon energy of  $\hbar\omega = 128$  meV (CO<sub>2</sub> laser), a nominal temperature<sup>10</sup> of  $T = 7$  K, a power at the tip of  $P_t = 14$  mW, and 100 nm tip oscillation amplitude. Figure 3.7 (a) shows a map of the topography (tapping mode) that contains sub-wavelength sized stripes and rectangles. The SiO<sub>2</sub> is about 15 nm higher in topography than the Si. The white rectangle in Figure 3.7 (a) indicates the area for the zoomed-in topography map in Figure 3.7 (b). We obtain a surface root-mean-square roughness of about 0.5 nm to 1 nm on both Si and SiO<sub>2</sub>, which demonstrates the high stability of the AFM at LHe operation.

The maps of the s-SNIM signal  $s_{2\Omega}$  are measured *in situ* and are visualized in Figures 3.7 (c) and (d). They reveal a reversed contrast with respect to the topography: here, Si appears brighter than SiO<sub>2</sub>. The permittivities of the two materials at 128 meV are  $\epsilon_{\text{Si}} = 11.8 + 2 \cdot 10^{-4}i$  for Si [81], and  $\epsilon_{\text{SiO}_2} = 6.9 + 7.9i$  for SiO<sub>2</sub> [89]. Hence, the s-SNIM signal on Si is expected to be higher due to the significantly higher absorption of SiO<sub>2</sub> (imaginary part of  $\epsilon$ , see Figure 2.7 in

<sup>10</sup>The exact temperature at the position of the tip might be higher due to the infrared irradiation as discussed later.

Section 2.2.2). We obtain a signal-to-noise ratio<sup>11</sup> of  $s_{2\Omega}$  of about 10 at Si, which is sufficient to observe even the small, grid-like substructures in the map [see top-left and bottom right areas in Figure 3.7 (a) and (b)]. The residual particles, marked by the red circles in Figure 3.7 (a) and (b), show a very low s-SNIM signal, which is typically observed in s-SNIM for non-resonant particles.

The s-SNIM signals decay rapidly when the respective material (plane Au<sup>12</sup>, Si, or SiO<sub>2</sub>) gets retracted from the tip at a fixed lateral position, as depicted in Figure 3.7 (e). All retract curves show roughly the same decay to  $s_{2\Omega}(z = 0)/e$  within 25 nm. The signal on Au is more than 10 times larger than on SiO<sub>2</sub> or Si due to the high infrared reflectivity of Au, which results in a higher s-SNIM signal. Since the decay length of the retract curve scales with the tip diameter (see Section 2.2.5), the retract curves in Figure 3.7 (e) indicate a small tip radius and thus a high spatial resolution.

Figure 3.7 (f) shows the profile (i) across a rectangle, marked by the white lines in Figure 3.7 (b) and (c). The slope of  $s_{2\Omega}$  is slightly steeper than the topography slope between the materials Si and SiO<sub>2</sub>. This implies that the material contrast of the s-SNIM is possibly even sharper than suggested by surface topography. Since the sharpness of the crossing between Si and SiO<sub>2</sub> is not known precisely, the spatial resolution can only be estimated to be in the order of 50 nm, which is in good agreement with the retract curves and previous FEL s-SNIM studies [42]. If we consider the wavelength of  $\lambda = 9.7 \mu\text{m}$  ( $\hbar\omega = 128 \text{ meV}$ ), we hence achieve a lateral optical resolution of about  $\lambda/200$ .

As reported in Section 3.3.1, the sample temperature sensor measures the temperature  $T_s$  directly underneath the sample holder. The focused infrared radiation, however, locally heats the sample at the position of the tip, which cannot be detected directly by the sample sensor. Hence, the actual temperature at the tip may vary significantly from the value of  $T_s$ . This local heating depends on the thermal conductivity, heat capacity, and the wavelength-dependent absorption of the investigated sample.

In order to quantify and calibrate the heat impact of the focused infrared radiation, we chose the multiferroic GaV<sub>4</sub>S<sub>8</sub> as a sample due to its well-defined phase

<sup>11</sup>For a power of  $P_t = 14 \text{ mW}$ , a lock-in amplifier integration time of 20 ms, and a scan speed of  $1 \mu\text{m/s}$ .

<sup>12</sup>Extra sample, scan images not shown here.

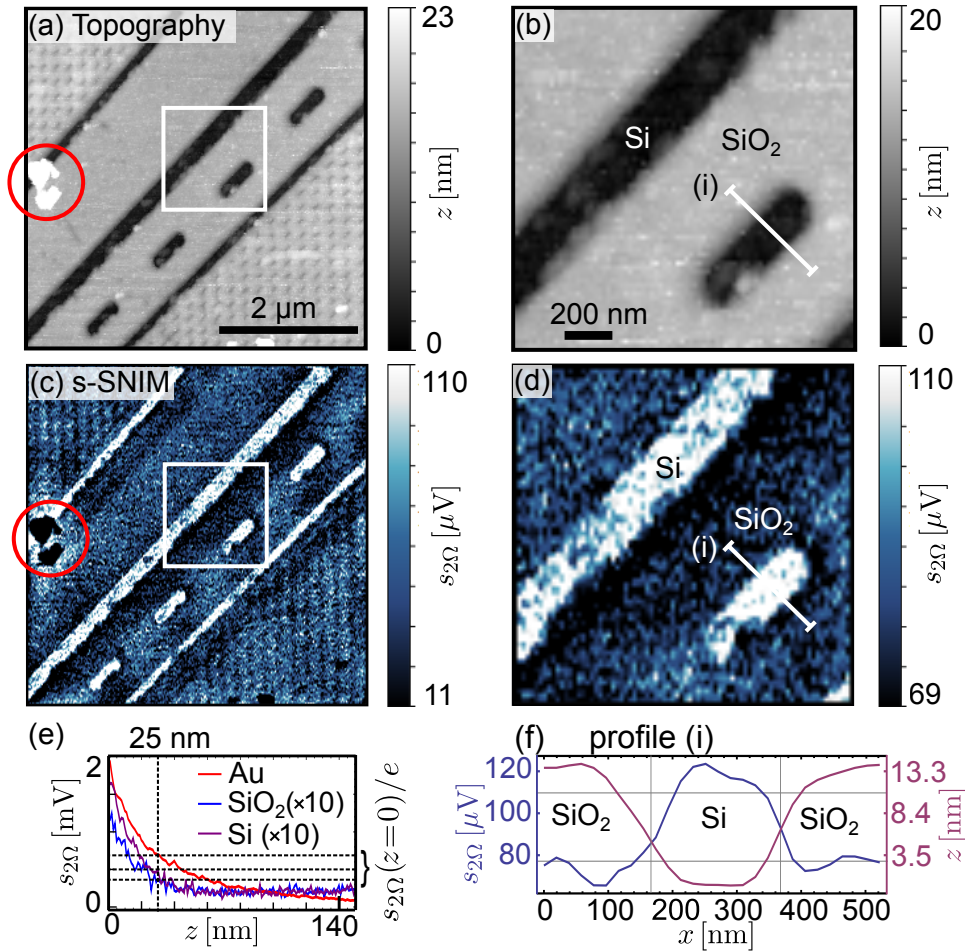


Figure 3.7: (a) Topography map of the structured Si/SiO<sub>2</sub> sample and (b) zoomed-in area [white box in (a)]. (c) s-SNIM  $s_{2\Omega}$  maps of the same area and (d) zoom [white box in (c)]. (e) Retract curves of  $s_{2\Omega}$  for Au (different sample), Si, and SiO<sub>2</sub>. (f) Profiles from white lines (i) in (b) and (d) of  $z$  and  $s_{2\Omega}$ , respectively. All measurements at 7K and at  $\hbar\omega = 128$  meV (CO<sub>2</sub> laser). Adapted from [61].



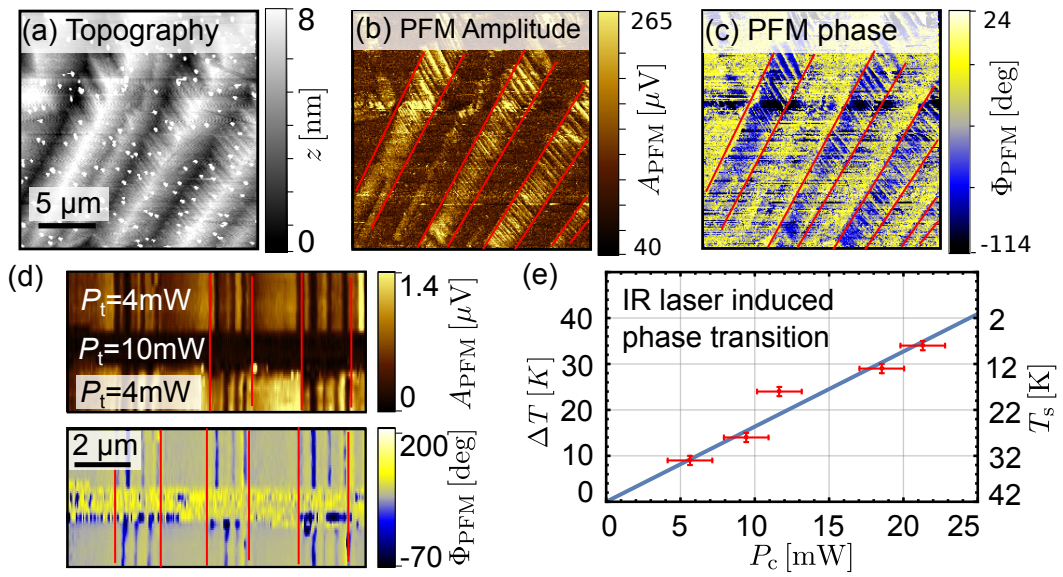


Figure 3.8: (a) Topography map, (b) PFM amplitude  $A_{\text{PFM}}$ , and (c) PFM phase  $\Phi_{\text{PFM}}$  of the (111) surface of a  $\text{GaV}_4\text{S}_8$  single crystal at  $T_s = 20$  K. The red lines indicate stripe domains that contain a substructure of lamella domains. (d) Exemplary linescan at  $T_s = 35$  K of  $A_{\text{PFM}}$  and  $\Phi_{\text{PFM}}$  under infrared irradiation that demonstrates the dis- and reappearing of domains at different infrared laser powers  $P_t$ . (e) Measured points (red) and linear fit (blue) of heating  $\Delta T$  to the phase transition at power  $P_c$ , where  $T_s$  denotes the starting sample temperature, respectively. Adapted from [61].

transition, the Jahn-Teller transition at  $T_c = 42$  K. Below  $T_c$ , the material is in its ferroelectric phase and hence shows characteristic ferroelectric domains [87] with polarizations pointing along any of the four  $\langle 111 \rangle$ -type axes. These domains can be visualized by applying PFM as long as their out-of-plane piezoelectric response varies<sup>13</sup>. Figure 3.8 (a) depicts the topography that already indicates larger domain stripes with a characteristic variation of the surface slope. Both PFM amplitude  $A_{\text{PFM}}$  [Figure 3.8 (b)] and PFM phase  $\Phi_{\text{PFM}}$  [Figure 3.8 (c)] reveal a lamellar-shaped ferroelectric domain pattern within the large stripes.

When we focus the CO<sub>2</sub> laser on the tip, we observe that the characteristic domain pattern disappears at a certain critical power  $P_c$ . Figure 3.8 (d) depicts an exemplary line scan at  $T_s = 35$  K. Starting with a power on the tip of  $P_t = 4$  mW, the stripes disappear in both amplitude and phase for an increased power of 10 mW. The domains reappear again after reducing the power to 4 mW. In general we note that the domain structure after the laser-induced local heating is either identical or strongly correlates with the initial domain structure.

In order to quantify the heating more precisely, the power  $P_t$  is increased gradually, starting from  $P_t = 0$  at various  $T_s$ , until the domain pattern disappears. At this particular critical power  $P_c$ , we know that the phase transition temperature  $T_c = 42$  K is reached and hence the local heating is given by

$$\Delta T = 42 \text{ K} - T_s. \quad (3.1)$$

By repeating this type of measurement for different starting temperatures  $T_s$ , we find a linear increasing correlation between  $P_c$  and  $\Delta T$  [see Figure 3.8 (e)]. Hence, we can define a laser-heating coefficient  $\xi$  of

$$\xi := \frac{\Delta T}{P_c} = (1.6 \pm 0.1) \frac{\text{K}}{\text{mW}}. \quad (3.2)$$

If we apply the same method at a photon energy close to the phonon resonance of GaV<sub>4</sub>S<sub>8</sub> at 37.6 meV using the FEL, we observe an increased coefficient of  $\xi \approx 2.4$ . Note that the spot size of the FEL's focus at this photon energy is expected to be about three times larger than for the CO<sub>2</sub> laser due to its larger wavelength. Hence, the power density is reduced by a factor of about 9. This indicates that the

---

<sup>13</sup>Note that we are only sensitive to the out-of-plane response due to the interferometric detection of the cantilever deflection (see Section 3.3.1).

absorption is actually much higher than for the nonresonant excitation heating represented by Equation (3.2).

Although the temperature-calibration values presented here are only valid for the particular material properties of  $\text{GaV}_4\text{S}_8$ , it gives a rough estimation of the infrared-heating impact in our setup. Moreover, the local laser-induced heating may be used to manipulate the domain structure in a controlled manner.

### 3.4.2 s-SNIM study of gallium vanadium sulfide

We investigate the (111) surface of gallium vanadium sulfide ( $\text{GaV}_4\text{S}_8$ ) by s-SNIM within the reststrahlen band between the strongest infrared-active phonon modes  $F_2$  at  $\hbar\omega_{\text{TO}} = 38.9 \text{ meV}$  and  $\hbar\omega_{\text{LO}} = 40.4 \text{ meV}$  (at 80 K [84]). The real part (blue) and the imaginary part (red) of the permittivity  $\varepsilon_{\text{GaV}_4\text{S}_8}$  are depicted in Figure 3.9 (a) for  $T = 300 \text{ K}$  [83]. We expect the highest s-SNIM signal at negative  $\text{Re}(\varepsilon)$ , where  $\text{Im}(\varepsilon)$  is still low (see Figures 2.7 and 2.9), which is in between 39 meV and 40 meV.

Figure 3.9 (b) shows s-SNIM spectra  $s_{2\Omega}(\omega)$  for Au (orange squares) and  $\text{GaV}_4\text{S}_8$  at 300 K (green rhombi), respectively, and an extended spectrum for  $\text{GaV}_4\text{S}_8$  at 10 K (red triangles). Indeed, the s-SNIM signal  $s_{2\Omega}$  on  $\text{GaV}_4\text{S}_8$  is strongly enhanced for photon energies lower than  $\hbar\omega = 39.8 \text{ meV}$ . Hence, we can clearly assign this s-SNIM resonance to the phonon mode  $F_2$ . However, the maximum of the s-SNIM signal is expected to be at slightly higher  $\hbar\omega$ , meaning closer to the longitudinal optical (LO) phonon frequency, since the imaginary part of  $\varepsilon$  is smaller<sup>14</sup>. Possible reasons for this deviation are:

- The far-field fourier-transform infrared spectroscopy (FTIR) study [83] uses a different  $\text{GaV}_4\text{S}_8$  crystal (but the same crystal orientation).
- The normalization of the s-SNIM spectrum (in this case to the power and the detector sensitivity) can be problematic due to the undefined optical phase and possible interferences for the self-homodyne detection method [57].

Figure 3.9 (c) presents the KPFM map in the ferroelectric phase at  $T_s = 10 \text{ K}$ . Just like the PFM maps in Figure 3.8, the KPFM image clearly reveals the lamel-

<sup>14</sup>At low temperatures, the deviation is even more pronounced since the phonon resonance should shift to higher  $\hbar\omega$  (see [83]).

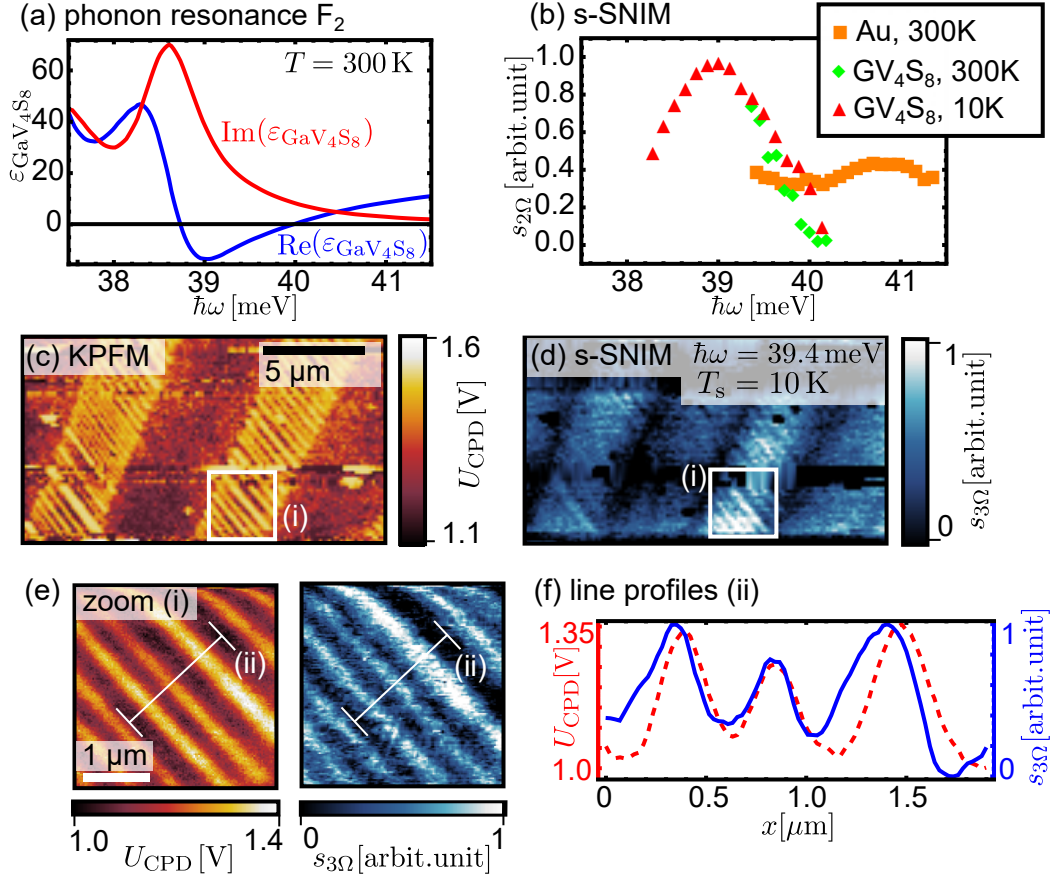


Figure 3.9: (a) Real part (blue) and imaginary part (red) of the GaV<sub>4</sub>S<sub>8</sub> permittivity  $\varepsilon(\omega)$  at  $T = 300$  K (measured data with permission from Reschke et al., compare reference [83]). (b) s-SNIM spectra  $s_{2\Omega}(\omega)$  of Au at  $T_s = 300$  K, as well as GaV<sub>4</sub>S<sub>8</sub> at  $T_s = 300$  K and  $T_s = 10$  K respectively (compare to [55], page 124). (c) KPFM and (d) resonant s-SNIM map in the ferroelectric phase at  $T_s = 10$  K (equivalent to [55], page 125). (e) Zoom (i) of KPFM (c) and s-SNIM (d), respectively, at the lamellar domains (compare to [55], page 127). (f) Profiles of  $U_{\text{CPD}}$  (red, dashed) and  $s_{3\Omega}$  (blue) along the line (ii) in (e). Adapted from [61].

lar domains within the larger stripes. Here, the contrast stems from surface screening of the ferroelectric domains that creates a surface-potential difference between the tip and the sample surface [90]. The s-SNIM map shows a contrast at the lamella-shaped domain structure due to differences in the out-of-plane component of the permittivity for different domains [55, pp. 125 sqq.]. Both channels, s-SNIM and KPFM, prove that we are in the ferroelectric phase below 42 K at the laser power of  $P_t = 12$  mW used here, which is in agreement with the estimated heating  $\Delta T = \xi P$  of about 20 K to 30 K (see Figure 3.8).

The zoomed-in maps of both KPFM  $U_{\text{CPD}}$  and s-SNIM  $s_{3\Omega}$  at position (i) are depicted in Figure 3.9 (e). The contrast of both channels is very similar, although the positions of the maxima and minima are not exactly at the same position, as revealed by the line profiles (ii) in Figure 3.9 (f). This could be due to the different depth sensitivities of KPFM and s-SNIM: since the domains are oriented obliquely to the surface, a deviation of the maxima for different effective scanning depths would be expected. The lateral distance between maxima and minima in  $s_{3\Omega}$  is about 250 nm. This means that the lateral optical resolution at the wavelength of  $\lambda = 31.5$   $\mu\text{m}$  is better than  $\lambda/126$ .

### 3.5 Conclusion

We have demonstrated the operation of our LT s-SNIM at liquid helium temperatures ( $T_s = 7$  K) using a structured Si/SiO<sub>2</sub> sample. This measurement reveals an excellent sub-nm stability of the AFM and a lateral resolution of the s-SNIM better than  $\lambda/200$ .

Moreover, we have experimentally quantified and calibrated the heat impact upon focused infrared radiation on the sample system of GaV<sub>4</sub>S<sub>8</sub> at its phase transition at 42 K. This example demonstrates that the infrared laser may be used to actively heat the sample on a local scale to intentionally write ferroelectric domains. In the ferroelectric phase at  $T < 42$  K, a clear contrast in all *in situ* accessible channels of our LT s-SNIM, namely topography, PFM, KPFM, and s-SNIM, has been demonstrated. Although PFM, KPFM, and s-SNIM reveal the same contrast at the example of (111) GaV<sub>4</sub>S<sub>8</sub>, these channels probe fundamentally different sample properties.



# 4 Infrared nanospectroscopy on semiconductor nanowires

This chapter contains comprehensive, infrared-nanospectroscopic results on semiconductor nanowires (NWs), in particular GaAs/InGaAs core/shell NWs and modulation doped InGaAs/InAlAs NWs. The results on the GaAs/InGaAs core/shell NWs, in particular the observed nonlinear plasmonic response at high field strengths, have been published in *Nanotechnology* **30**, 084003 (2018) [91].

## 4.1 Introduction

Over the past few years, semiconductor NWs have emerged as highly promising building blocks for future (opto-)electronic nanodevices. This includes, for instance, light-emitting diodes [92, 93], lasers [94], solar cells [95, 96], detectors [97, 98], transistors [99], and polarizers [100]. More specifically, epitaxially grown NWs based on III-V compounds such as GaAs are suitable for ultrafast optoelectronic applications due to their direct bandgap and high electron mobility. An important advantage of epitaxial GaAs-based NWs is the achievable compatibility with complementary metal-oxide-semiconductor (CMOS) technology despite the large lattice mismatch [101]. Ternary compounds such as  $\text{In}_x\text{Ga}_{1-x}\text{As}$  furthermore open up the possibility to tune the direct band gap by changing the composition  $x$ . Thus, any NW-based device (for example an detector or emitter) can be conveniently optimized for the aimed spectral range [102].

A possible way to determine the electronic properties of semiconductors is to measure their Hall coefficients by a four-point [103] or even three-point probe method [104]. To fabricate several ohmic contacts for an individual NWs is, however, challenging from a technological point of view. This becomes even more crit-

ical, when the electrical properties of many NWs should be probed in the frame of quality control. Alternatively, terahertz time-domain spectroscopy (TDS) enables a contactless determination of charge carrier density, mobility, and carrier lifetime for NW ensembles [105, 106]. This is achieved by probing the plasmonic response in the THz frequency range and extracting the free-carrier THz conductivity.

THz conductivity spectra information of NWs in the aforementioned works have been , however, limited to large assemblies of wires. Since the spot of focused THz radiation is about three orders of magnitude larger than the NWs, near-field techniques are required to determine the electrical properties locally on the nanometer scale. To this end, the unique capabilities of s-SNIM were previously employed by several groups:

- Stiegler et al. [12] measured the carrier distribution along a partially doped InP NW. Later on [107], they applied s-SNIM in combination with transmission electron microscopy to characterize the cross sections of zinc oxide NWs.
- Eisele et al. [14] performed time-resolved measurements on photoexcited charge carriers in an InAs NW, which also provided access to the carrier lifetimes.
- Arcangeli et al. [108] utilized an electrical gate to locally tune the plasma frequency in an InAs NW, which they probe by s-SNIM.
- Choi et al. [109] used both s-SNIM and scanning microwave impedance microscopy (sMIM) to analyze the profile of a lateral multi p-n junction GaAs NW.
- Recently, Zhou et al. [110] observed surface plasmon polariton (SPP) standing wave patterns on an InAs NW.

Except for the investigations on photoexcited carriers [14], all studies so far reported on linear optical properties. In fact, there are no observations of nonlinear effects so far that are directly induced by a mid-infrared probe beam. This may be related to the fact that typical mid-infrared (MIR) and THz sources used in



combination with s-SNIM yield low powers prohibiting the observation of nonequilibrium states, even though the field of the tip in proximity to the surface can be strongly enhanced.

Here, we investigated GaAs core-shell NWs, where the much thicker InGaAs shell is strongly n-doped with Si. Firstly, we observe a strong plasmonic resonance at about 125 meV by using the CO<sub>2</sub> laser as IR light source. Secondly, we find a pronounced red shift by about 20 meV to 40 meV and strong damping of the plasma resonance in the case of using the FEL. The plasmonic shift strongly depends on the power, i. e. the peak power density, of the FEL, which indicates a significant heating of electrons in the nonparabolic conduction band of InGaAs. This heating effectively increases the effective mass and hence decreases and broadens the plasmonic resonance.

Additionally, we investigate NW cross sections fabricated by the focused ion beam (FIB) technique. This cross sections include the InGaAs/GaAs core/shell NWs mentioned above, and modulation doped NWs based on InGaAs/InAlAs containing a Si delta-doped layer. The s-SNIM measurements on the NW cross sections were performed at the group of Prof. T. Taubner, Rheinisch-Westfälische Technische Hochschule (RWTH) Aachen, where we used a commercial *Neaspec* s-SNIM system. The latter contains a pseudo-heterodyne detection [57], which effectively suppresses parasitic background interference at edges and trenches of the cross-section sample.

## 4.2 Samples

All presented NWs are grown by molecular beam epitaxy (MBE) at the Institute of Ion Beam Physics and Materials Research at HZDR. This Section summarizes the most important informations about the growth and properties of the NWs.

### 4.2.1 GaAs/InGaAs core/shell nanowires

The GaAs/InGaAs core/shell NWs were grown by MBE on Si(111) substrates in multiple steps. First, GaAs cores were grown with a diameter of 25 nm and a length of 2 μm [111, 112]. Figure 4.1 (a) shows a scanning electron microscopy (SEM) image of the NWs after the core growth. Secondly, the cores

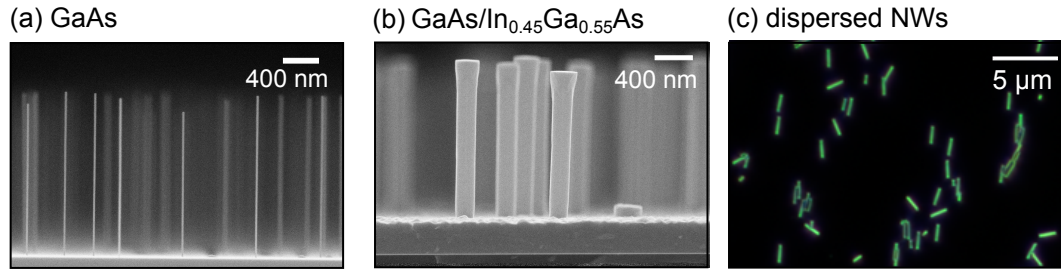


Figure 4.1: (a) SEM image after the GaAs core growth. (b) SEM image after the InGaAs shell growth. (c) Dark-field optical microscopy image of the dispersed NWs on Si(100). Adapted from [91].

were overgrown with a 80 nm thick Si-doped  $\text{In}_{0.45}\text{Ga}_{0.55}\text{As}$  shell, as depicted in Figure 4.1 (b). The nominal Si concentration is about  $9 \times 10^{18} \text{ cm}^{-3}$  [113, 114]. The NW cross sections have a hexagonal shape and the shell reveals a largely homogeneous composition along and perpendicular to the NW axis [114]. For s-SNIM measurements, the NWs are dispersed on a Si(100) substrate, as shown on the dark-field optical microscopy image in Figure 4.1 (c). The Si substrate also acts as a reference for the s-SNIM measurements since it shows no spectrally noticeable behavior in the MIR spectral range of interest [see Figure 3.2 (b)].

## 4.2.2 Modulation doped nanowires

Modulation doping is a semiconductor fabrication method aiming to separate the charge carriers from the donors [115]. The separation should minimize the impurity scattering to achieve a high carrier mobility [106, 116, 117].

Our MBE-grown modulation doped NWs have about the same overall dimensions ( $\sim 2 \mu\text{m}$  length,  $\sim 200 \text{ nm}$  diameter) as the GaAs/InGaAs core/shell NWs. Figure 4.2 (a) shows an exemplary SEM image of the grown NWs on Si(111) substrate. In contrast to the core/shell NWs, the modulation doped NWs yield a more complex composition as depicted in Figure 4.2 (b). The GaAs core with a diameter of 25 nm is overgrown by 40 nm thick  $\text{In}_{0.45}\text{Ga}_{0.55}\text{As}$ . Subsequently, an additional 10 nm thick  $\text{In}_{0.44}\text{Al}_{0.56}\text{As}$  spacer is grown, followed by the delta-doped Si sheet with a nominal sheet density of  $4 \times 10^{12} \text{ cm}^{-2}$ . Finally, the delta-doped sheet gets overgrown by a 30 nm thick  $\text{In}_{0.44}\text{Al}_{0.56}\text{As}$  barrier and an  $\text{In}_{0.45}\text{Ga}_{0.55}\text{As}$  capping layer. The latter should prevent oxidation of  $\text{In}_{0.44}\text{Al}_{0.56}\text{As}$  at the surface.

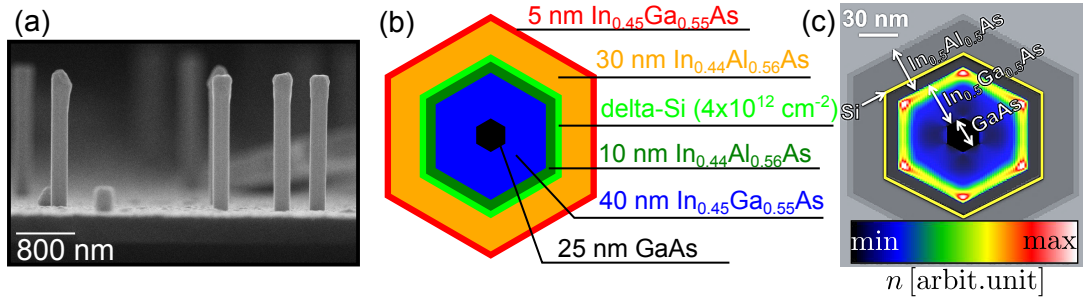


Figure 4.2: (a) SEM image of modulation doped NWs grown on Si(111) substrate. (b) Schematic drawing of the modulation doped NW's cross section including the composition. (c) *Nextnano* simulation of the carrier distribution for a similar composition. The simulation predicts a high carrier density at the edge of the inner InGaAs shell with additional hot spots at the corners of the hexagon.

The band structure of the NW heterostructure leads to a redistribution of the introduced charge carriers. Both band structure and carrier distribution can be simulated by using the *Nextnano* software. Figure 4.2 (c) shows such a simulation for a modulation doped NW with a similar composition ( $\text{In}_{0.5}\text{Ga}_{0.5}\text{As}$  and  $\text{In}_{0.5}\text{Al}_{0.5}\text{As}$ ) compared to the grown NWs. According to this simulation, the carriers localize on the outer edge of the inner InGaAs shell, thus forming a channel within the NW. More specifically, hot spots of highest carrier density appear at each of the hexagon corners following the crystal symmetry.

### 4.2.3 Nanowire cross sections

In order to perform s-SNIM measurements on NW cross sections, individual NWs have to be precisely cut at the middle position of the NW long axis. The latter is important since the middle of a NW typically yields the best crystal quality and lowest impurity density. Such a preparation of cross sections can be achieved by a focused ion beam procedure as described in the following:

1. The starting point are dispersed NWs on (undoped) Si(100) substrate, as described in Section 4.2.1. Proper NWs close to the cleaved edge of the Si substrate can be found by using *in-situ* SEM of the ion beam microscope. The corresponding NWs should be located about halfway over the edge and

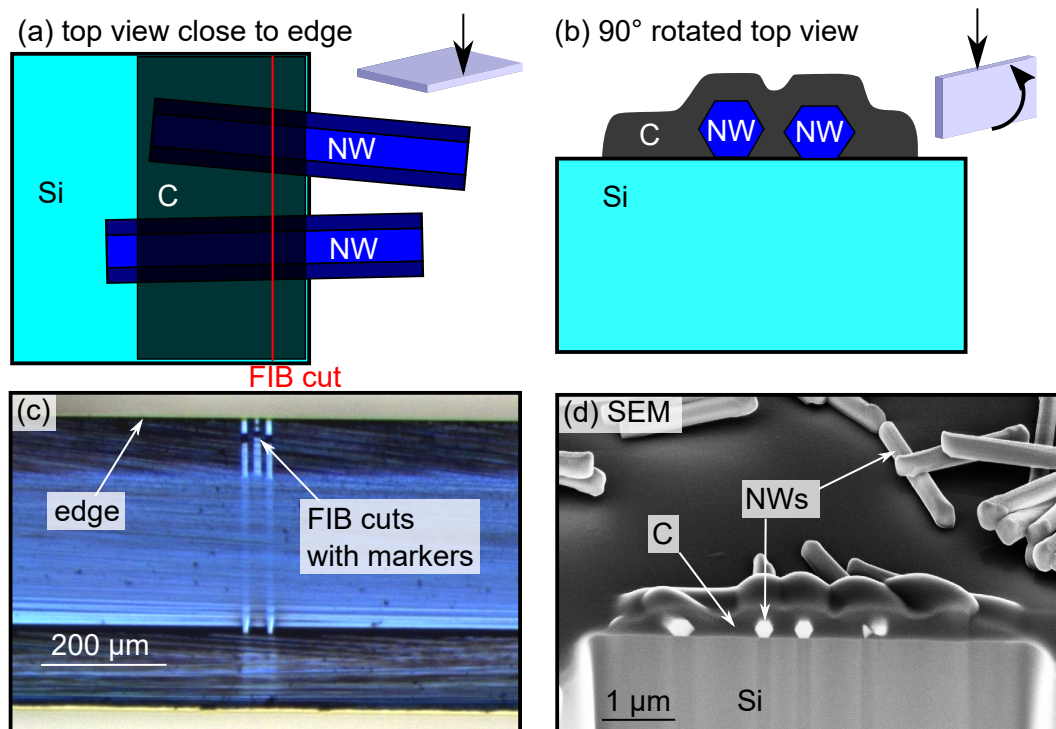


Figure 4.3: FIB procedure to produce NW cross sections for s-SNIM: (a) NWs at the edge covered by amorphous carbon. (b) Top view with NW cross sections of the rotated sample after FIB sputtering. (c) Optical microscopy image of the edge with trenches from the FIB sputtering (middle trench includes NWs, left and right are markers). (d) SEM image at the edge after the FIB procedure with two cleanly cut modulation doped NWs.

aligned approximately perpendicular to the edge (skewed NWs later lead to a distortion of the cross section).

2. The NWs get covered by a few 100 nm thin layer of amorphous carbon by electron-beam deposition from a phenanthrene precursor gas in order to fix them, protect them from damage through highly energetic ions, and to guarantee a perpendicular FIB cut in spite of the Gaussian Ga-beam profile as well [Figure 4.3 (a)].
3. Ion-beam sputtering at a high beam current removes the excess parts of the NWs and a low current polishing creates a smooth surface. This leads to a trench-like structure at the Si substrate edge along the ion beam trajectory. Additionally, further trenches can be sputtered as markers to find the right position in the s-SNIM.
4. For s-SNIM measurements we rotate the sample by  $90^\circ$ . Hence, the cross sections face to the top and can be accessed by the AFM tip [Figure 4.3 (b)].

Figure 4.3 (c) shows a sample with modulation doped NWs after the FIB procedure, looking on top of the cleaved edge. The trenches of the FIB sputtering are clearly visible. Here, the middle trench includes the NW cross sections, whereas the left and right trenches serve as markers. Figure 4.3 (d) reveals the cross sections of the middle trench. The two central NW cross sections yield a symmetric cross section suitable for s-SNIM measurements, whereas the cross section on the left shows a large distortion.

#### 4.2.4 Infrared response of doped nanowires

In the following, the expected infrared response is discussed using the example of the doped GaAs/InGaAs core/shell NWs of Section 4.2.1.

The infrared response of the NWs in terms of the permittivity  $\varepsilon_{\text{NW}}$  can be described by the InGaAs permittivity since the InGaAs shell is significantly larger than the tip radius and also much thicker than the GaAs core. Hence,

the frequency-dependent permittivity is given by the Lorentz-Drude model as

$$\varepsilon_{\text{NW}}(\omega) = \varepsilon_{\text{optic}} - \underbrace{\frac{\omega_{\text{TO}}^2(\varepsilon_{\text{static}} - \varepsilon_{\text{optic}})}{\omega^2 - \omega_{\text{TO}}^2 + i\omega\gamma_p}}_{\text{optical phonon}} - \underbrace{\frac{\omega_{\text{pl}}^2\varepsilon_{\text{optic}}}{\omega^2 + i\omega\gamma_{\text{el}}}}_{\text{plasmonic}}. \quad (4.1)$$

The second term in Equation (4.1) describes the optical phonon response<sup>1</sup> by the Lorentz oscillator model [119]. Here,  $\varepsilon_{\text{optic}} = 11.5$  is the high-frequency permittivity,  $\varepsilon_{\text{static}} = 13.7$  is the static permittivity [120],  $\omega_{\text{TO}} = 28 \text{ meV}/\hbar$  is the frequency of the transversal optical (TO) phonon [118], and  $\gamma_p = 0.25 \text{ meV}/\hbar$  is the phonon damping [121]. Note that the longitudinal optical (LO) phonon frequency  $\omega_{\text{LO}}$  is determined by the Lyddane-Sachs-Teller relation [122]:

$$\frac{\omega_{\text{LO}}^2}{\omega_{\text{TO}}^2} = \frac{\varepsilon_{\text{static}}}{\varepsilon_{\text{optic}}}. \quad (4.2)$$

The last term in Equation (4.1) is the Drude model [123] that describes the response of the charge carriers (plasmonic part). Here,  $\omega_{\text{pl}}$  is the plasma frequency and  $\gamma_{\text{el}}$  denotes the electronic damping. The plasma frequency is given by

$$\omega_{\text{pl}}^2 = \frac{ne^2}{m^*\varepsilon_0\varepsilon_{\text{optic}}}, \quad (4.3)$$

where  $n$  is the carrier density,  $e$  is the elementary charge,  $m^*$  is the effective mass, and  $\varepsilon_0$  is the vacuum permittivity. The electronic damping is given as

$$\gamma_{\text{el}} = \frac{e}{\mu m^*}, \quad (4.4)$$

where  $\mu$  is the carrier mobility.

Figure 4.4 (a) depicts the real part  $\text{Re}(\varepsilon)$  (blue) and the imaginary part  $\text{Im}(\varepsilon)$  (red) of the permittivity according to Equation (4.1) for doped InGaAs. The sharp feature at about 28 meV is the phonon resonance, whereas the shallow slope of the curves stems from the Drude response of the charge carriers. For the  $n$ ,  $m^*$ , and  $\mu$  values given in this example, the resonance condition for s-SNIM

<sup>1</sup>Note that the optical phonon spectrum of the ternary alloy InGaAs is actually more complex [118] than, for example, GaAs. For the sake of clarity we show here the simplified GaAs-like phonon behavior.

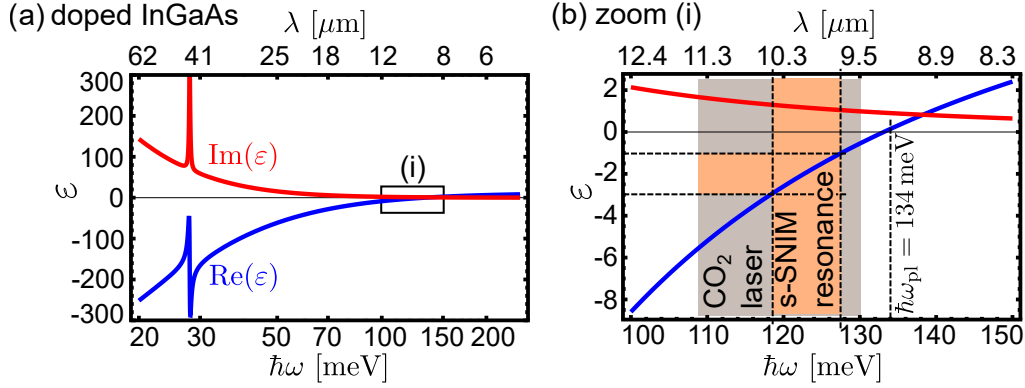


Figure 4.4: (a) Frequency dependence of the infrared permittivity for doped InGaAs according to Equation (4.1) with  $n = 9 \times 10^{18} \text{ cm}^{-3}$ ,  $m^* = 0.06m_e$ , and  $\mu = 1000 \text{ cm}^2/(\text{V s})$ . (b) Zoom of area (i) for the spectral resonant range for s-SNIM (see Section 2.2.2), which overlaps with the  $\text{CO}_2$  laser tuning range.

(see Section 2.2.3) is fulfilled for photon energies of roughly 120 meV to 130 meV. Note that the s-SNIM resonance is always shifted towards lower photon energies with respect to the plasma frequency (in this case  $\omega_{\text{pl}} = 134 \text{ meV}/\hbar$ ). Moreover, the plasma frequency does not exactly equal the zero-crossing of  $\text{Re}(\varepsilon)$  due to the finite imaginary part.

## 4.3 Experimental details

All of the s-SNIM measurements on the NWs were performed at room temperature (RT), mostly with the room-temperature scattering scanning near-field infrared microscopy (RT s-SNIM) setup at the HZDR. Here, the infrared sources ( $\text{CO}_2$  laser and FEL, see Section 2.3) as well as the layout of the optical table are identical to the LT s-SNIM (see Section 3.3). Just the cross sections have been studied using a commercial *Neaspec* s-SNIM with interferometric detection at the group of Prof. T. Taubner, RWTH Aachen.

### 4.3.1 Room-temperature atomic force microscopy

The RT s-SNIM is based on a home-made AFM [Figure 4.5 (a)] with particularly good optical access, reduced scattering of mechanical parts close to the tip, and

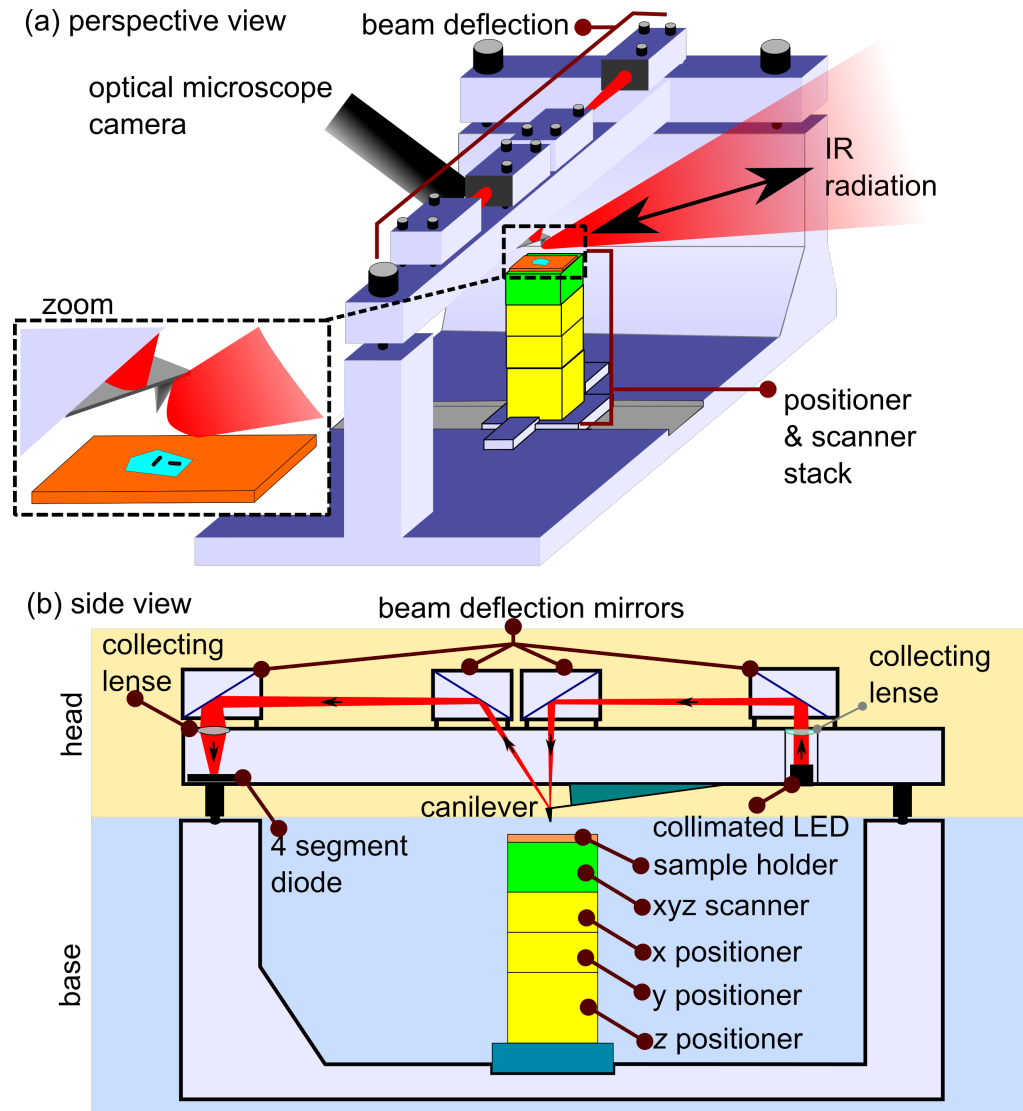


Figure 4.5: Schematic drawings of the home-built room-temperature atomic force microscope (RT AFM): (a) Perspective view of the AFM with optical access for infrared radiation from one side and an optical microscope camera from the other side. (b) Side view of the AFM. The cantilever's motion is detected by the beam-deflection method. The sample is scanned and positioned by a stack of scanner and positioner elements [similar to Figure 3.4 (b)].



a high mechanical stability. Furthermore, the AFM yields sufficient space from both sides to illuminate the tip with the infrared radiation (see next Section 4.3.2) on one side and observe the approached tip with a optical microscope camera on the other side. In contrast to the LT s-SNIM, the motion of the tip is detected by the beam-deflection method (see Section 2.1.1). Figure 4.5 (b) shows a side-view scheme of the AFM. A red, collimated laser diode ( $\lambda = 635 \text{ nm}$ ,  $P \sim 1 \text{ mW}$ ) is focused onto the cantilever's<sup>2</sup> back side and the reflected light is detected by a four segment diode. Hence, vertical as well as horizontal displacements of the cantilever can be recognized. For tapping mode (and therefore also s-SNIM), the metallized tip is excited resonantly at  $\Omega \sim 150 \text{ kHz}$  to  $190 \text{ kHz}$  by a piezoelectric actuator.

The sample is positioned and scanned by a stack of several positioner and scanner elements from *Attocube* with a sample holder on top. The three stick-slip positioners for  $x$ ,  $y$  and  $z$  yield a maximal range of  $(5 \times 5 \times 5) \text{ mm}^3$  with a minimal step size of  $50 \text{ nm}$ . The maximal range of the  $xyz$  scanner is  $(40 \times 40 \times 24) \mu\text{m}^3$  with a sub-nm precision. The control of the AFM as well as the data acquisition is provided by the *RHK R9* AFM controller (see Section 3.3.4). Similar to the LT AFM, the RT AFM supports the electrical modes PFM (see Section 2.1.2) and KPFM (see Section 2.1.3) since both tip and sample holder are electrically contacted.

### 4.3.2 Room-temperature scattering scanning near-field infrared microscopy

The layout of the optical table can be found in Figure 3.5 of Section 3.3.2. In contrast to this scheme, the infrared radiation (see Section 2.3) is guided to the red-colored area, where the RT s-SNIM is located. The RT s-SNIM setup follows basically the same principle as the LT s-SNIM (see Section 3.3.3). Figure 4.6 (a) depicts a schematic drawing of the s-SNIM beam path. The beam is split up into one part towards the power meter and another part that is focused onto the apex of the metallized tip. The back-scattered radiation is collected by the same parabolic mirror and detected by a LN<sub>2</sub>-cooled mercury cadmium telluride

<sup>2</sup>We use non-contact AFM cantilevers PPP-NCLPt from *Nanosensors*.

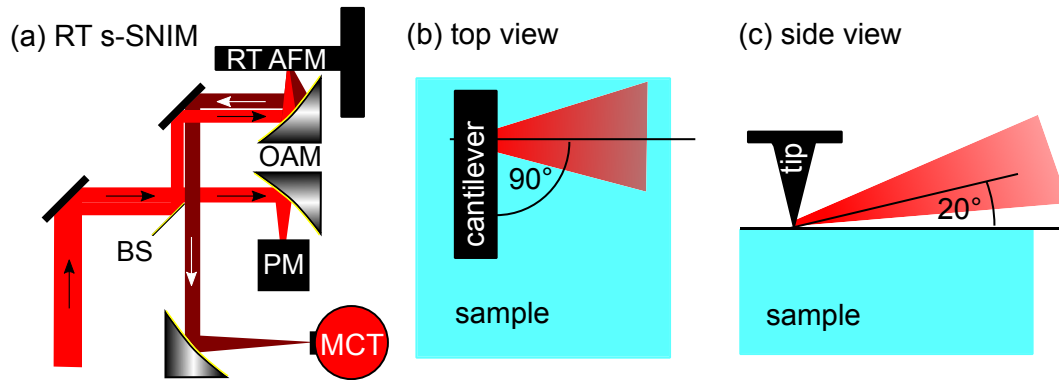


Figure 4.6: (a) RT s-SNIM beam path with RT AFM (see Figure 4.5), off-axis parabolic mirror (OAM), beam splitter (BS), mercury cadmium telluride (MCT), and power meter (PM). (b) Top view at the cantilever with  $90^\circ$  angle between the incoming infrared laser and the long axis of the cantilever. (c) Front view at the cantilever and tip with an angle of  $20^\circ$  between the laser and the sample surface.

(MCT)<sup>3</sup>.

Figures 4.6 (b) and (c) show the angles of the incoming beam with respect to the cantilever and sample, respectively. We focus the infrared radiation with an 2" off-axis parabolic mirror with 7.5 cm focus length. This results in a (maximal) numerical aperture (NA) of 0.32 for a perfectly collimated beam with a diameter of 2".

The RT s-SNIM has some clear practical advantages over the LT s-SNIM, even when using the LT s-SNIM at room temperature. These advantages are:

- the RT s-SNIM signal strength (and signal-to-noise ratio) is typically higher due to the significantly better NA and the lack of additional cryogenic windows,
- the microscope camera is closer to the tip, which makes it easier to find a particular sample position.

For these reasons – also considering the limited FEL beam time – RT s-SNIM is always preferable to LT s-SNIM if low temperatures are not essential.

<sup>3</sup>Teledyne Judson Technologies, models *MCTJ15D5* - *MCTJ15D26*, depending on the wavelength.

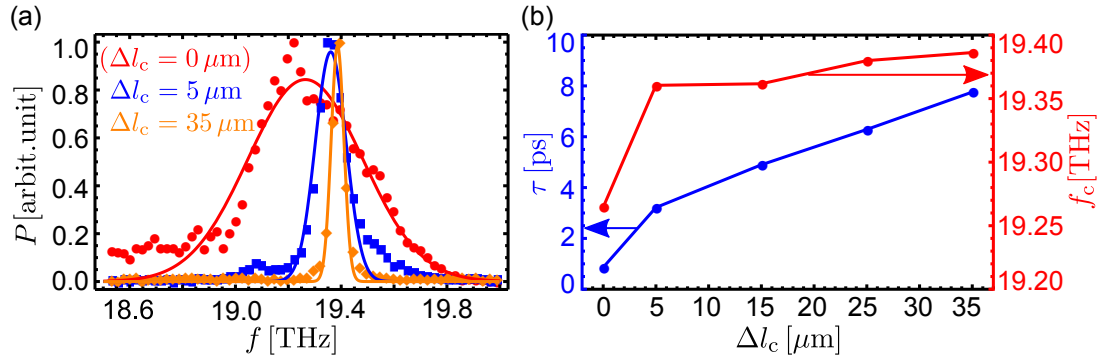


Figure 4.7: (a) Exemplary FEL spectra at about 80 meV (19.3 THz) for different relative cavity lengths  $\Delta l_c$ . The measured spectra are represented by the dots whereas the solid lines are the fitted Gaussian functions. (b) Extracted pulse durations  $\tau$  (blue) and center frequencies  $f_c$  as function of the relative cavity length  $\Delta l_c$ .

### 4.3.3 Properties of the free-electron laser pulses

The basic principle and most important parameters of the FEL have already been discussed in Section 2.3.2. This section treats the experimental properties of the FEL pulses with regard to the achievable pulse energy as well as the peak values of power, intensity, and electric field, respectively. Those pulse properties are particularly important for the observed nonlinear effect.

Generally, we only measure the average power  $P_{\text{avg}}$  by a power meter and the spectral distribution  $I(f)$  by a grating spectrometer, while we assume a constant repetition rate of  $f_{\text{rep}} = 13 \text{ MHz}$ . The average power and the repetition rate can be used to directly determine the pulse energy:

$$\mathcal{E}_{\text{pulse}} = \frac{P_{\text{avg}}}{f_{\text{rep}}}. \quad (4.5)$$

A determination of the pulse peak values, such as the peak power  $P_p$  or the peak electric field  $E_p$ , require more informations on the pulse duration and the laser spot size. The pulse duration  $\tau$  can be estimated from the spectral width  $\Delta f$  of the pulse. The relation between both is given by the time bandwidth product for transform-limited Gaussian-shaped pulses to  $\tau \Delta f = 0.44$  [both  $\tau$  and  $\Delta f$  are full width at half maximum (FWHM) values].

Figure 4.7(a) shows FEL spectra (dots) for different detuning  $\Delta l_c$  of the FEL

cavity length  $l_c$ . Here,  $\Delta l_c = 0$  denotes the cavity length with the highest emitted laser power [red dots in Figure 4.7 (a)]. Note that the cavity length with the highest power is slightly shorter than  $l_c = c/f_{\text{rep}}/2$  [124, 125], which means that the cavity is already detuned at this point. If  $l_c$  is increased, the FEL stops lasing rapidly. On the other hand, an decreasing cavity length gradually decreases the total power and, more importantly, the width of the spectrum decreases rapidly. This means that the pulse duration increases with increasing  $l_c$ . To quantify this behavior, the spectra can be approximated by Gaussian functions:

$$P(f) \propto \text{Exp} \left[ \frac{-(f - f_c)^2}{2\sigma_f^2} \right], \quad (4.6)$$

where  $f_c$  is the center frequency and  $\sigma_f$  is the standard deviation. The FWHM can be calculated as  $\Delta f = 2\sqrt{2\ln 2}\sigma \approx 2.355\sigma$ . The corresponding pulse durations are depicted as blue curve in Figure 4.7 (b). The bandwidth and hence the pulse duration spans over nearly one order of magnitude resulting in an achievable  $\tau$ -range of about 1 ps to 8 ps. Since we neglect the slightly inhomogeneous shape of the spectrum, general deviations from the Gaussian shape, and any chirp of the pulses, the actual pulse durations might be longer and the given values can be treated as lower limit. Also note that not only the spectral width changes for the cavity detuning but also the center frequency, as depicted by the red curve of Figure 4.7 (b).

Knowledge on the pulse energy and pulse duration enables the calculation of the peak power  $P_p$ , which is given for a Gaussian pulse shape by

$$P_p = \sqrt{\frac{4\ln 2}{\pi}} \frac{\mathcal{E}_{\text{pulse}}}{\tau} \approx 0.94 \frac{\mathcal{E}_{\text{pulse}}}{\tau} = 0.94 \frac{P_{\text{avg}}}{\tau f_{\text{rep}}}. \quad (4.7)$$

The factor  $0.94/(\tau f_{\text{rep}})$  describes the enhancement factor of the peak power compared to the average power and is, for example, in the order of  $10^4$  for  $\tau = 7.2$  ps and  $f_{\text{rep}} = 13$  MHz.

The peak electric field  $E_p$  can be calculated by

$$E_p = \left( \frac{2I_p}{cn\varepsilon_0} \right)^{1/2}, \quad (4.8)$$

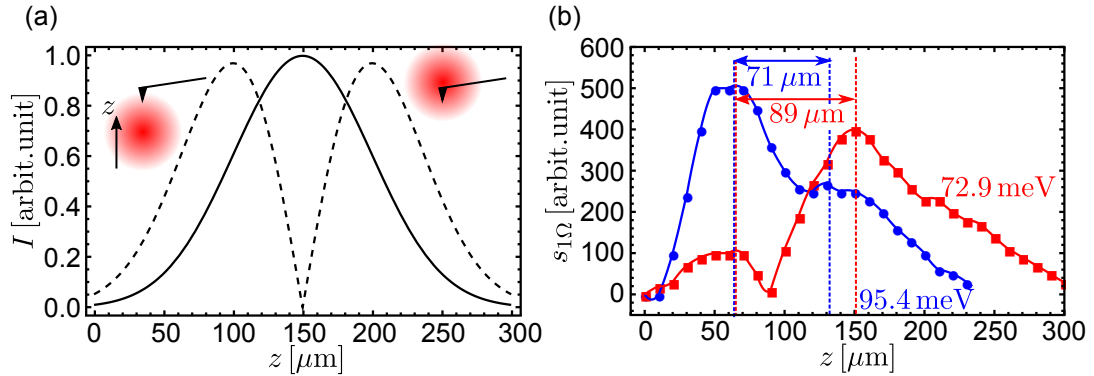


Figure 4.8: (a) Exemplary Gaussian beam shape (solid line) and its first derivative (dashed line; absolute, rescaled value) for a beam width of  $w = 50 \mu\text{m}$ . The schematic insets demonstrate the motion of the beam spot with respect to the oscillating cantilever. (b) Measured curves with the FEL of  $s_{1\Omega}$  for  $\hbar\omega = 72.9 \text{ meV}$  (red) and  $\hbar\omega = 95.4 \text{ meV}$  (blue) that reveal an asymmetric shape.

where  $n$  is the refractive index and  $I_p$  is the peak intensity. The latter depends on the beam size and is, for a Gaussian profile, given by

$$I_p = \frac{2P_p}{\pi w^2}, \quad (4.9)$$

where  $w$  is the beam width (radius). To roughly estimate the beam width at the position of the tip, the oscillation of the latter can be used. The focus is moved in the  $z$  direction perpendicular to the cantilever and the backscattered demodulated signal is recorded at the tip's resonance frequency  $f = \Omega$  (here, the sample is far away from the tip). The modulation of the signal is highest when the gradient of the beam profile is steepest, i. e. the first derivative has a maximum. For a (spatially) Gaussian shaped beam profile with a width of  $w = 50 \mu\text{m}$  and a maximum at  $z = 150 \mu\text{m}$ , as depicted by the black solid line in Figure 4.8 (a), the absolute value of the first derivative shows a symmetric shape (dashed line) with maxima at  $z_1 = 100 \mu\text{m}$  and  $z_2 = 200 \mu\text{m}$ . The measured optical signal  $s_{1\Omega}$ , demodulated at the first harmonic of the cantilever oscillation, shows a highly asymmetric shape for the FEL, as depicted in Figure 4.8 (b). The distance between the maxima are  $71 \mu\text{m}$  for  $\hbar\omega = 95.4 \text{ meV}$  and  $89 \mu\text{m}$  for  $\hbar\omega = 72.9 \text{ meV}$ . Since the spot size scales linearly with the wavelength, it should hold

that  $\lambda_1/\lambda_2 = \omega_2/\omega_1 = w_1/w_2$ . Indeed,  $\omega_2/\omega_1 \approx 1.31$  is close to  $w_1/w_2 \approx 1.25$  for the measured curves.

Taking into account all estimated parameters, such as pulse duration and spot size, it is possible to calculate the pulse energy  $\mathcal{E}_{\text{peak}}$ , the peak power  $P_p$ , and the peak electric field  $E_p$  using the above mentioned equations. In Table 4.1 these values are given for an s-SNIM typical average power range of 5 mW to 50 mW and different pulse durations  $\tau$ . The electric field strength  $E_p$  is calculated for a focused Gaussian beam with  $w = 50 \mu\text{m}$  in vacuum ( $n = 1$ ).

Table 4.1: Typical FEL values for  $P_{\text{avg}} = 5 \text{ mW}$  to  $P_{\text{avg}} = 50 \text{ mW}$  of the pulse energy  $\mathcal{E}_{\text{pulse}}$ , peak power  $P_p$ , peak intensity  $I_p$  and peak electric field  $E_p$  (both  $I_p$  and  $E_p$  for  $w = 50 \mu\text{m}$ ).

$\tau$ [ps]	$\mathcal{E}_{\text{pulse}}$ [nJ]	$P_p$ [kW]	$I_p$ [ $\text{GWcm}^{-2}$ ]	$E_p$ [ $\text{kVcm}^{-1}$ ]
2		0.18-1.81	0.46-4.60	59-186
4	0.4-3.8	0.09-0.90	0.23-2.30	41-132
6		0.06-0.60	0.15-1.5	34-107
8		0.05-0.45	0.12-1.15	29-93

Note that the actual electric field may be significantly higher due to the strong field confinement. The latter typically appears at the very end of the antenna-shaped, metallized tip in proximity to the surface. However, an exact determination of the electric field at the tip apex requires a more complex simulation. For example, Huth et al. [126] predict a field enhancement of up to  $20\times$  for a similar wavelength range (MIR), tip geometry (pyramidal), and angle of incidence between laser and tip (see Figure 4.6).

## 4.4 Results and discussion

### 4.4.1 GaAs/InGaAs core/shell nanowires

Figure 4.9 (a) shows an exemplary map of two perpendicular NWs on Si substrate. Here, the s-SNIM signal  $s_{2\Omega}$ , measured with the FEL at a photon energy of 90 meV, is illustrated in a false color scale and the topography is represented by the relief. The NWs yield a length of  $2 \mu\text{m}$  and thickness of about 200 nm. In this example, the NWs appear clearly brighter than the Si substrate whereas the

edges and particularly the ends of the NWs appear dark. For the s-SNIM spectra, we usually extract the value of the NW from the geometrical middle position. For the p-polarized radiation used in this studies, we find no significant impact of the NW orientation with respect to the plane of incidence. Hence, we can exclude a geometrical resonance and claim that we only probe the local carrier-induced permittivity variations  $\varepsilon(n, m^*, \mu)$ .

Figure 4.9 (b) depicts s-SNIM maps of a NW at two different photon energies measured with the CO<sub>2</sub> laser at a power of about 20 mW. The NW appears almost four times brighter with respect to Si at  $\hbar\omega = 117$  meV. The contrast reverses for higher photon energy of 129 meV, where the NW is clearly darker than the surrounding Si. Additional s-SNIM contrast values  $s_{NW}/s_{Si}$  are depicted as blue dots in Figure 4.9 (d) as a function of the photon energy  $\hbar\omega$ . The spectrum yields the characteristic resonant shape with a contrast reversal  $s_{NW}/s_{Si} = 1$  at 122 meV and a contrast maximum  $s_{NW}/s_{Si} = 3.9$  at 117 meV.

The spectrum can be fitted with the point-dipole model [see Equations (2.25) and (2.20)] including the permittivities of the NW and Si (see Section 4.2.1). The fitted model is represented by the blue curve in Figure 4.9 (d), with the light-blue area being the confidence interval including both plasma frequency and damping. Here, we find a plasma frequency of  $\omega_{p,0} = (126 \pm 5)$  meV and a plasmonic damping of  $\hbar\gamma_{p,0} = (18 \pm 5)$  meV. The corresponding electronic properties are a carrier density of  $n = (8.3 \pm 0.50) \times 10^{18} \text{ cm}^{-3}$  and an electron mobility of  $\mu = (1020 \pm 300) \text{ cm}^2(\text{Vs})^{-1}$ , if we assume an effective mass of  $m^* = 0.063 \cdot m_e$  (value for  $m^*$  explained later). We do not observe a shift of the contrast for higher powers of the laser (up to  $\sim 100$  mW) and therefore denote this resonance as linear plasmonic resonance.

The behavior of the s-SNIM contrast differs significantly if the NW is probed by the pulsed FEL, where much higher (peak) powers can be achieved. Figure 4.9 (c) shows exemplary s-SNIM maps for two different peak powers  $P_p$ . Here, we observe a reversal of the contrast  $s_{NW}/s_{Si}$  by increasing  $P_p$  from 0.27 kW up to 0.77 kW. The contrast spectrum in Figure 4.9 (d), represented by the red dots, reveals the significant redshift and increased damping of the plasmonic resonance for the FEL measurement. For the different points of the spectrum, the peak power varied in the range of 0.3 kW to 0.6 kW, which could explain deviations to the fitted model (red curve). The latter is obtained by keep all values fixed with

respect to the linear resonance, and only fit the plasmonic parameters. Hence, we find the plasma frequency to be  $\omega_p = (95 \pm 5)$  meV and the damping equal to  $\hbar\gamma_p = (40 \pm 5)$  meV. Since the carrier density should be constant, this means that the effective mass has to increase to

$$m^* = 0.063 m_e \cdot \left( \frac{125 \text{ meV}}{95 \text{ meV}} \right)^2 = 0.11 m_e . \quad (4.10)$$

According to Equation (4.4), the increased effective mass and damping must also reduce the carrier mobility significantly to  $\mu = (260 \pm 30) \text{ cm}^2(\text{Vs})^{-1}$ .

The s-SNIM contrast  $s_{\text{NW}}/s_{\text{Si}}$  depends both on the photon energy and the (peak) power, as depicted in the color-map in Figure 4.9 (e). The dashed line (as a guide to the eye) indicates how the plasma resonance, represented here by the contrast reversal  $s_{\text{NW}}/s_{\text{Si}} = 1$ , gradually shifts towards lower photon energies for increasing peak powers. The dashed line should merge the value of  $\hbar\omega = 122$  meV for very low peak powers, where the contrast reversal is observed with the CO<sub>2</sub> laser. However, the peak power range in between the CO<sub>2</sub> laser and FEL measurements is not accessible experimentally since it requires either very high average powers of the CO<sub>2</sub> laser (disturbs or even destroys the tip) or very low average powers of the FEL (signal too small to detect).

According to Equation (4.10), the strong redshift can be explained by an increase of the effective mass of the free carriers upon the strong, pulsed infrared illumination. Such behavior has been observed in various far-field studies before, for example on photoexcited GaAs [127] as well as on n-doped InGaAs [128]. Both studies explain their findings by intervalley scattering, i. e. from the  $\Gamma$ - to the L-valley, in the strong electric field of (few cycle) THz radiation. As part of this model, electrons in the low-effective mass  $\Gamma$ -valley get accelerated by a high electric field and gain enough energy to scatter to the high-effective mass L-valley, just before the ac-field reverses and electrons move back in the opposite direction. In our case, however, the photon frequency is about one order of magnitude higher than in references [127, 128]. Accordingly, the cycle-averaged quiver energy of electrons, also known as ponderomotive energy is

$$\mathcal{E}_{\text{pon}} = \frac{e^2 E^2}{4m^* \omega^2} \approx 2 \text{ meV} \quad (4.11)$$



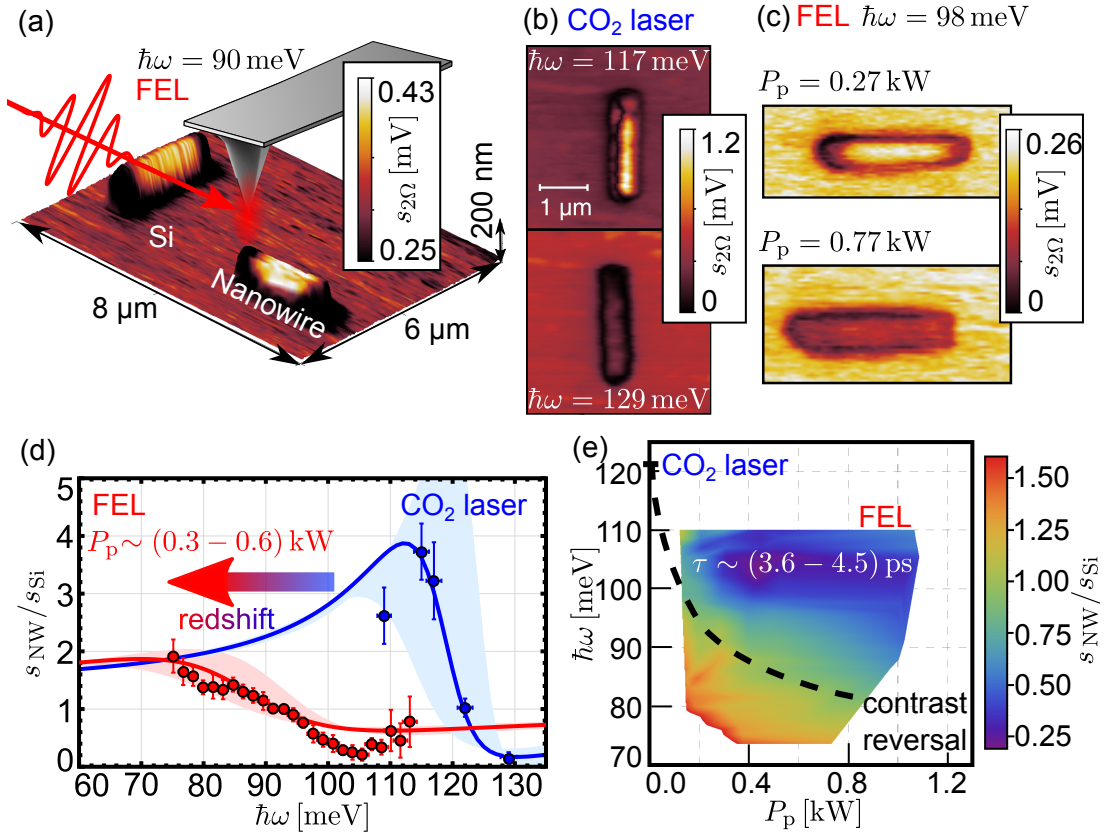


Figure 4.9: (a) Exemplary map with s-SNIM signal  $s_{2\Omega}$  (color scale) and topography (relief). The cantilever, tip and incoming FEL pulse are added schematically. (b) s-SNIM maps for two different photon energies measured with the CO<sub>2</sub> laser. (c) s-SNIM maps at two different peak powers  $P_p$  measured with the FEL. (d) Spectral dependence of s-SNIM contrast (points) and fitted curves (lines) for CO<sub>2</sub> laser (blue) and FEL (red), respectively. (e) Measured s-SNIM dependence on both photon energy and peak power. The color map visualizes the gradual spectral shift for the FEL measurements. At very low peak powers, the resonance should converge towards the CO<sub>2</sub> laser resonance, as indicated by the dashed line. Adapted from [91].

for an electric field of  $E = 100 \text{ kVcm}^{-1}$  and  $\omega = 2\pi \cdot 30 \text{ THz}$ . Since the energy difference between the  $\Gamma$ - and the L-valley is way larger (400 meV [129]), direct intervalley-scattering is very unlikely or should only occur for unrealistically high field values.

Tyborski et al. [130] found a plasmonic redshift and broadening in n-doped ZnO attributed to a significant heating of the carriers in the nonparabolic conduction band and a subsequent increase of the effective mass. Analogous to ZnO, InGaAs reveals a nonparabolicity of the  $\Gamma$ -valley that can be described by [131]

$$\mathcal{E}(1 + \alpha\mathcal{E}) = \frac{\hbar^2 k^2}{2m_\Gamma}, \quad (4.12)$$

where  $\alpha = 1.33 \text{ eV}^{-1}$  is the nonparabolicity factor and  $m_\Gamma = 0.044m_e$  is the effective mass at the  $\Gamma$ -point<sup>4</sup> [132]. Figure 4.10 (a) reveals the nonparabolic approximation of the conduction band (CB) in comparison to the parabolic approximation ( $\alpha = 0$ , dashed line). According to [133, 134], the effective mass depends linearly on the energy (see Appendix C.1):

$$m(\mathcal{E}) = m_\Gamma(1 + 2\alpha\mathcal{E}). \quad (4.13)$$

The energy-dependent distribution  $n_e$  of free carriers in the CB is described by the product of the Fermi-Dirac distribution and the density of states (DOS, see Appendix C.2) as

$$n_e(\mathcal{E}) = \frac{1}{2\pi^2} \left( \frac{2m_\Gamma}{\hbar^2} \right)^{3/2} \frac{[\mathcal{E}(1 + \alpha\mathcal{E})]^{1/2}(1 + 2\alpha\mathcal{E})}{e^{(\mathcal{E}-\mathcal{E}_F)/(k_B T)} + 1}, \quad (4.14)$$

where  $k_B$  is the Boltzmann constant,  $\mathcal{E}_F$  is the chemical potential, and  $T$  is the temperature of the electron gas. The average effective mass can be calculated considering both the energy-dependent effective mass (4.13) and the carrier distribution (4.14) as

$$\frac{1}{m^*} = \frac{1}{n} \int_0^\infty d\mathcal{E} \frac{n_e(\mathcal{E})}{m(\mathcal{E})}, \quad (4.15)$$

where  $n = \int_0^\infty d\mathcal{E} n_e$  is the total carrier density in the CB. The latter has been

---

<sup>4</sup>Note that these literature values are, technically, for a slightly different composition ( $\text{In}_{0.53}\text{Ga}_{0.47}\text{As}$ ).

found to be  $n_e = 8.3 \times 10^{18} \text{ cm}^{-3}$  according to the linear plasma resonance fit, where the temperature of the electron gas is  $T \approx 300 \text{ K}$ . By considering equations (4.14) and (4.15), we obtain an average effective mass of  $m_0^* = 0.063m_e$  at a chemical potential of  $\mathcal{E}_F = 250 \text{ meV}$ . For the nonlinear, redshifted plasma resonance, where the effective mass increased to  $0.113m_e$ , we can estimate a temperature of  $T = 3900 \text{ K}$  at  $\mathcal{E}_F = -465 \text{ meV}$ . Figure 4.10 (b) depicts the carrier distributions for both cases: the cold (blue) and hot (red) electron plasma. Accordingly, the significant increase of the effective mass for the latter results from the increased number of electrons with higher energy and hence higher mass.

For a more detailed estimation of the heating effect, one should also take into account the satellite valleys in InGaAs, such as the  $X$ - or  $L$ -valley that would probably decrease the simulated temperature since the effective masses are typically higher in these valleys. Moreover, holes in the valence band may have an additional impact at high temperatures of the Fermi-distribution since the chemical potential tends to decrease for increasing  $T$ . However, the impact of holes should still be small due to the much higher effective mass of the heavy holes ( $m_{\text{hh}}^* \approx 0.36m_e$  [120]), and to the low DOS for the light holes. Due to the mentioned possible effects, the estimated temperature of  $T = 3900 \text{ K}$  can be considered as an upper limit.

According to Equation (4.14) we can directly calculate the difference between the energy densities of the electron gas<sup>5</sup> to

$$\begin{aligned} \mathcal{E}_{3900 \text{ K}} - \mathcal{E}_{300 \text{ K}} &= \int_0^\infty d\mathcal{E} [n_e(3900 \text{ K}) - n_e(300 \text{ K})] \cdot \mathcal{E} \\ &\approx 8.4 \times 10^5 \text{ J/m}^3. \end{aligned} \quad (4.16)$$

Alternatively, the FEL dissipation can be estimated by Joule's law and the frequency dependent Drude model as

$$\mathcal{E}_{\text{diss}} = \frac{\sigma_0}{1 + (\omega/\gamma_{\text{el}})^2} \frac{\tau \cdot E_{\text{p}}^2}{2}, \quad (4.17)$$

where  $\sigma_0 = ne^2/(m^*\gamma_{\text{el}})$  is the zero-frequency conductivity. By assuming  $\omega = 95 \text{ meV}/\hbar$  and  $\tau = 2 \text{ ps}$ , it requires a peak-field strength of  $E_{\text{p}} = 51 \text{ kVcm}^{-1}$  to

<sup>5</sup>A simple estimation is given by  $\mathcal{E} = (3/2)Nk_{\text{B}}(3900 \text{ K} - 300 \text{ K}) \approx 6.2 \times 10^5 \text{ J/m}^3$ , which is close to the numerically calculated value.

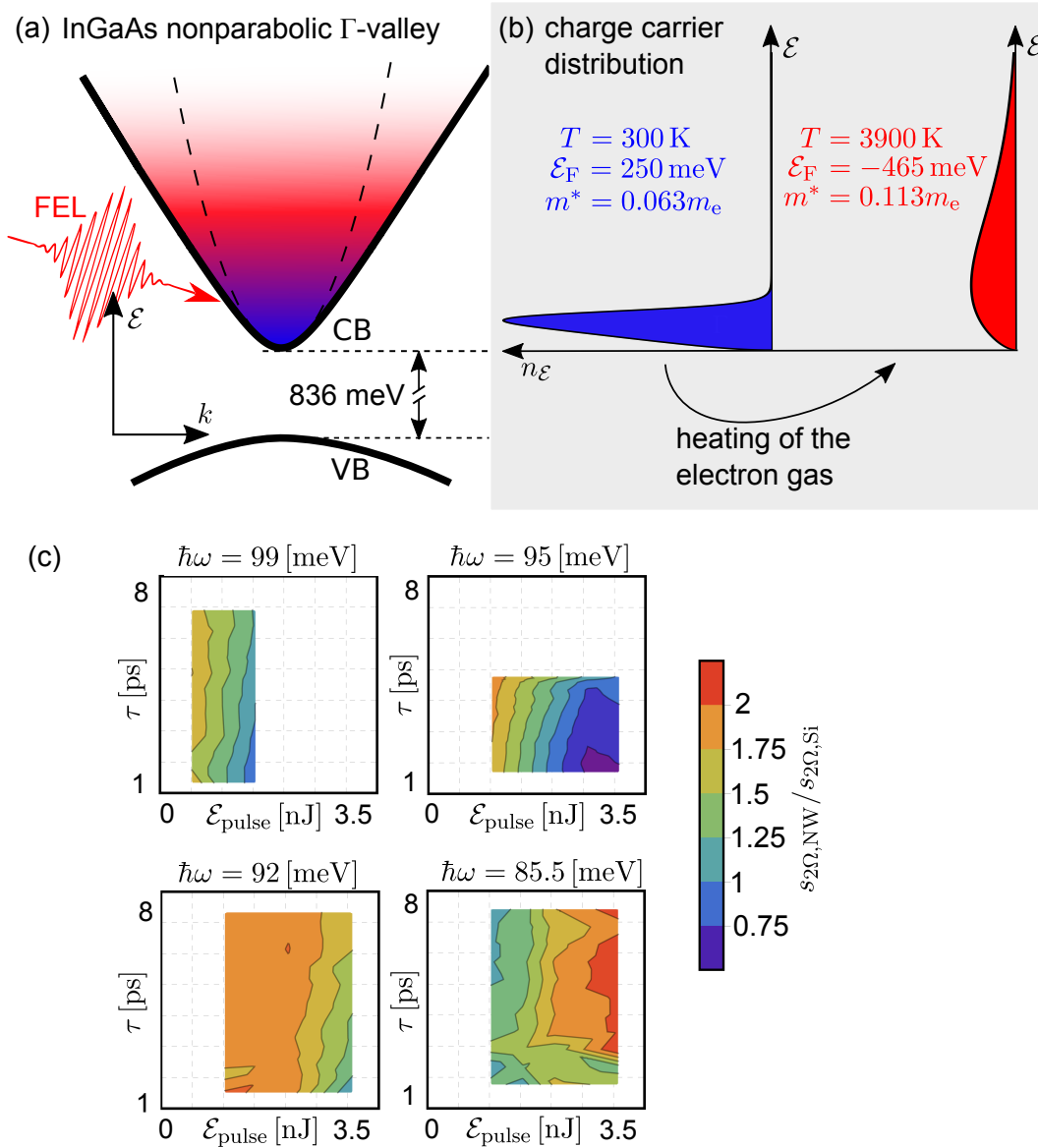


Figure 4.10: (a) Schematic drawing of the nonparabolic InGaAs  $\Gamma$ -valley. (b) Charge carrier distributions for both linear plasmonic response (blue) and nonlinear plasmonic response (red), where the electron gas is heated up to 3900 K by the intense FEL pulses. (c) Maps of the s-SNIM contrast  $s_{\text{NW}}/s_{\text{Si}}$  in dependence of the pulse energy  $\mathcal{E}_{\text{pulse}}$  and the pulse duration  $\tau$  for different photon energies  $\hbar\omega$ , respectively. Adapted from [91].

heat the electron gas to  $T = 3900$  K, according to the dissipated energy estimated in Equation (4.16). In fact, the estimated peak field value is in good accordance to the FEL field values specified in Section 4.3.3.

In order to prove the heating scenario we varied the pulse duration  $\tau$  (see Section 4.3.3) while keeping the pulse energy  $\mathcal{E}_{\text{pulse}}$  constant. Figure 4.10 (c) depicts the s-SNIM contrast in dependence of the  $\tau$  and  $\mathcal{E}_{\text{pulse}}$  for four different photon energies, respectively. For a particular, fixed pulse duration, the resonance shifts to lower photon energies for an increasing pulse energy, according to the tendency observed in Figure 4.9 (e). At a photon energy of  $\hbar\omega = 85.5$  meV, the contrast slope even reverses (that means  $s_{\text{NW}}/s_{\text{Si}}$  increases for increasing  $\mathcal{E}_{\text{pulse}}$ ). Hence, the opposite (and more shallow) edge of the plasmonic resonance is reached here.

For all photon energies, the impact of the pulse duration is very weak, i. e. much weaker than the influence of the pulse energy, although a slight slope is visible in all graphs. This behavior supports our theory that the dissipation of FEL pulses is the relevant mechanism here. Since the initially dissipated energy is transferred to the lattice within the pulse duration, the resonance should still be influenced by  $\tau$ . The strongest energy transfer should happen via LO phonon emission at much shorter time scales with respect to the FEL pulse duration, i. e. at sub-ps time scales [135]. Consequently, excitation and relaxation should be (almost) in an equilibrium for all measured pulse durations, which could explain the very weak observed  $\tau$ -dependence. The minor slope of  $\tau$  could still indicate that the shorter pulses lead to a slightly higher electron heating with less energy transfer to the lattice (smaller pulse energy is needed to observe the same effect).

#### 4.4.2 Nanowire cross sections

We studied cross sections of both GaAs/InGaAs core/shell NWs (see Section 4.2.1) and modulation doped NWs (see Section 4.2.2). All cross sections have been prepared by FIB fabrication as discussed in Section 4.2.3. The s-SNIM maps have been recorded by pseudo-heterodyne detection [57] using a commercial *Neaspec* s-SNIM<sup>6</sup> in the group of Prof. Taubner, RWTH Aachen. Here, pseudo-heterodyne detection was necessary since the measurement at the direct sample edge and the

<sup>6</sup>The infrared source used here is a commercial laser system tunable in the MIR (QCL based): *DRS Daylight solutions*, model *MIRcat-QT*.

FIB grooves lead to strong background interference that cause artifacts in the case of non-interferometric, i. e. self-homodyne, detection (see Appendix D).

The SEM image in Figure 4.11 (a) shows five cross sections (white) of GaAs/InGaAs core/shell NWs, surrounded by carbon towards the edge (black) and Si towards the sample (grey). The topography and s-SNIM maps are recorded at the position of the marked area (white rectangle) in the SEM image. The topography map in Figure 4.11 (b) reveals about 14 nm deep trenches (also visible in SEM) towards the Si, starting from the actual NWs position. In the s-SNIM amplitude map [Figure 4.11 (c)], the edges of these trenches are also visible. The NW cross sections reveal a clear contrast to the surrounding carbon, although the exact hexagonal shape is hardly visible due to a slight distortion of the cross sections. We could not find any contrast to the undoped core that measures only 25 nm in diameter. The s-SNIM phase map [Figure 4.11 (d)] shows a blurry contrast of the cross sections, which is differently pronounced for each of the NWs. We observe only a very weak spectral dependence of both s-SNIM amplitude [Figure 4.11 (e)] and phase [Figure 4.11 (f)] between the NWs and the Si for a photon energy range of about 105 meV to 140 meV. Hence, there is no clear evidence for a plasmonic resonance. Since usually all NWs of this type (that have not been cut) showed a plasmonic resonance at about 120 meV, it is likely that the surface has been damaged during the FIB treatment.

Two cross sections of the modulation doped NWs are depicted in the SEM image of Figure 4.12 (a). The white rectangle again marks the position of the topography and s-SNIM maps. The topography map [Figure 4.12 (b)] shows a trench depth of about 12 nm. The s-SNIM map [Figure 4.12 (c)] reveals a clear contrast in between the outer NW shell (mostly  $\text{In}_{0.44}\text{Al}_{0.56}\text{As}$ ) and the inner part of the NW (mostly  $\text{In}_{0.45}\text{Ga}_{0.55}\text{As}$  with GaAs core). This contrast could be an indication that an increased charge carrier concentration has formed in the middle region of the NW. In contrast, the phase map [Figure 4.12 (c)] shows no clear difference between the inner and the outer NW, although the hexagonal outer edge remains roughly recognizable. However, the s-SNIM spectrum of both amplitude [Figure 4.12 (e)] and phase [Figure 4.12 (f)] shows no clear spectral dependence. It is therefore questionable whether the observed contrast is even caused by charge carriers or if it is just material contrast of InAlAs, InGaAs, and carbon, respectively.

Finally, there are several possible reasons why we do not find evidence for a

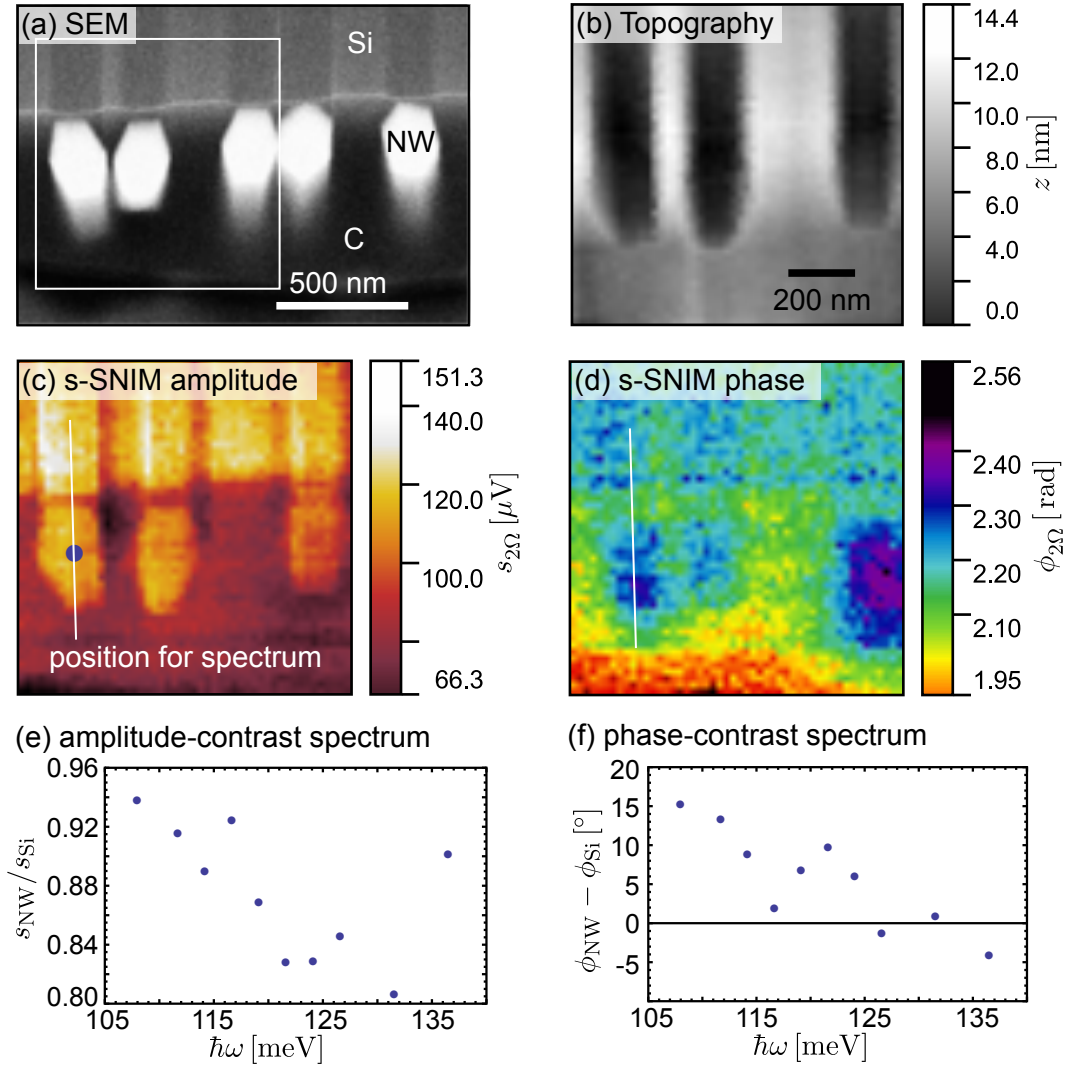


Figure 4.11: Cross sections of GaAs/InGaAs core/shell NWs: (a) SEM image with zoom selection for s-SNIM (white rectangle). (b) Topography map. (c) s-SNIM amplitude map at  $\hbar\omega = 116.5$  meV. (d) s-SNIM phase map. (e) Spectrum of the s-SNIM amplitude contrast between Si and the left NW [blue dot in (c)]. (f) Spectrum of the s-SNIM phase contrast [same position as (e)].

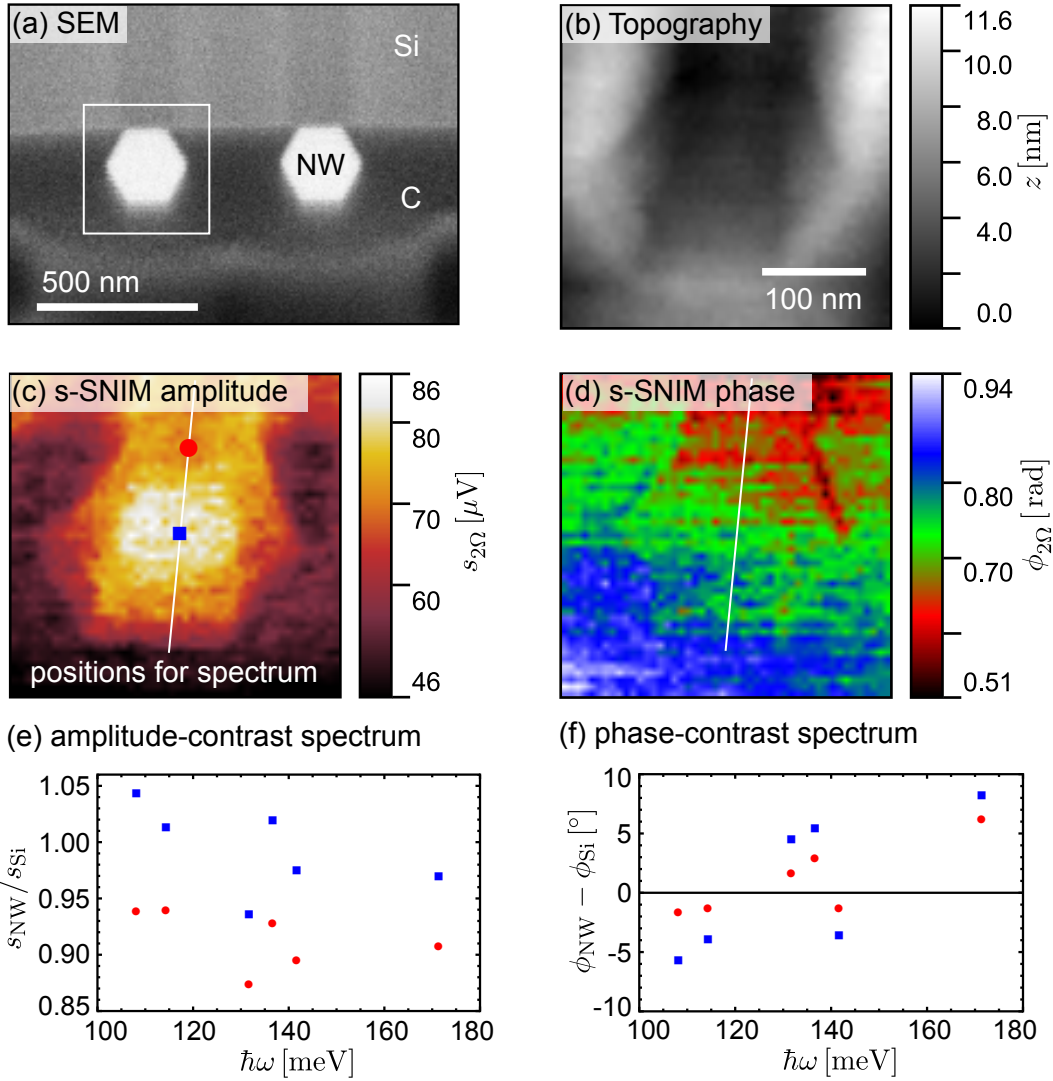


Figure 4.12: Cross sections of the modulation doped NWs: (a) SEM image with zoom selection for s-SNIM (white rectangle). (b) Topography map. (c) s-SNIM amplitude map at  $\hbar\omega = 136.4$  meV. (d) s-SNIM phase map. (e) Spectrum of the s-SNIM amplitude contrast between Si and the inner NW [blue rectangle in (c)] as well as contrast between Si and the outer NW [red dot in (c)]. (f) Spectrum of the s-SNIM phase contrast [same positions as (e)].



plasmonic resonance in any of the cross sections:

- The FIB process, in particular the introduction of Ga atoms as additional impurities, decreases the carrier density and/or the mobility. Moreover, FIB processing typically forms a  $\sim 10$  nm thick amorphous layer [136], disrupting completely the electronic structure close to the surface,
- for the modulation doped NWs: the spatial resolution ( $\sim 25$  nm) is too low, i. e. the number of electrons in the effective probe volume [ $\sim (25 \text{ nm})^3$ ] is too low,
- the plasma frequency is not in (or close) to the probed frequency range of about 105 meV to 170 meV.

## 4.5 Conclusion

In this chapter, s-SNIM studies have been presented on GaAs/InGaAs core/shell NWs lying flat on Si, as well as on NW cross sections of core/shell NWs and modulation doped NWs, respectively.

The linear plasmonic response of the highly Si-doped core/shell NWs, measured on Si substrate with the cw CO<sub>2</sub> laser, yield a sharp resonance at about  $\omega_{\text{pl}} = 125 \text{ meV}/\hbar$ . Hence, we can quantify the charge carrier density to  $8 \times 10^{18} \text{ cm}^{-3}$  and the mobility of about  $1000 \text{ cm}^2\text{V}^{-1}\text{s}^{-1}$ , which demonstrates the excellent quality of the MBE-grown nanowires. For the first time, we observe a nonlinear plasmonic response induced by the intense pulses of the FEL. This manifests itself in a significant redshifted of the plasmonic resonance to about 95 meV, which corresponds to an increase of the effective mass by about 74 %. The latter can be explained by energy dissipation of the FEL pulses and thus heating of the electron gas in the nonparabolic conduction band of InGaAs. The variation of the pulse duration while keeping the pulse energy constant shows only a weak effect, which underlines the dissipation hypothesis. We further estimate the total dissipated energy and hence quantify the electric field at the s-SNIM tip apex to be in the order of  $50 \text{ kVcm}^{-1}$ . Our findings open up the possibility not only to passively probe, but rather actively manipulate the s-SNIM contrast by the intense and (in

this wide frequency tuning range) unique radiation of the FEL. Thus, a new path to explore nonlinear plasmonics on the nanometer scale is enabled.

Furthermore, cross sections of two kinds of NWs have been produced by FIB technique. The cross sections of the highly Si-doped GaAs/InGaAs core/shell NWs show, in contrast to those lying flat on Si, no pronounced plasmonic resonance for the same frequency range. Similarly, no indication of free charge carriers could be found for the modulation doped NWs, in which the expected position of the resonance was not known before. The lack of resonance, especially in the case of the homogeneously doped NWs, could be due to damage to the surface and/or amorphization during FIB processing. The FIB may induce additional impurities that increase the scattering and hence reduce the mobility at the surface. However, we could achieve a contrast on both type of NWs, which is probably a material contrast between the NWs and the surrounding carbon and Si. In the case of the modulation doped NWs, we can even distinguish between the inner InGaAs and the outer InAlAs shell, principally demonstrating the high resolution and sensitivity of the s-SNIM.

# 5 Summary and outlook

In this work, two main aspects were addressed: the development of a cryogenic s-SNIM system, and the room-temperature investigations on semiconductor NWs at high electric fields. Both topics are connected by the use of the FEL as a uniquely intense and widely tunable IR radiation source.

The LT s-SNIM setup, based on the LT AFM (Section 3.3.1) and the infrared-optical setup (Section 3.3.2), has been described in detail. Thus, our LT s-SNIM is able to operate in the temperature range from 5 K to 300 K and, in combination with the FEL, in the spectral range from 5 meV to 250 meV. To the best of our knowledge, it is the only cryogenic s-SNIM system worldwide that combines these characteristics. Furthermore, with our s-SNIM system it is also possible to apply complementary AFM modes like PFM or KPFM with one and the same tip. In particular, KPFM can be used *in-situ* to s-SNIM in order to effectively prevent artifacts caused by surface charges. We demonstrated the performance of all modes, i. e. topography, s-SNIM, PFM, and KPFM, at LHe temperatures. For this purpose, standard samples such as structured Si-SiO<sub>2</sub> and Au, as well as the interesting multiferroic material GaV<sub>4</sub>S<sub>8</sub> have been measured. The latter reveals a subtle ferroelectric domain pattern below its structural phase transition at  $T_c = 42$  K. This domain pattern showed signatures in all previously mentioned measurement channels. With the help of the FEL we were able to spectrally identify the near-field resonance of GaV<sub>4</sub>S<sub>8</sub> in the vicinity of the phonon resonance at about  $\hbar\omega = 39$  meV. Finally, this made it possible to measure domain patterns in the s-SNIM signal. Furthermore, we could utilize the clearly defined phase transition to quantify the influence of the infrared radiation on the local temperature under the tip. The local impact of the IR beam could also be used in the future to specifically create domain structures. Moreover, a possible correlation between the formation of the ferroelectric domains and its skyrmion phase could be a point of future investigations.

The measurements on semiconductor NWs, which make up the second part of the work, have been investigated with the room-temperature scattering scanning near-field infrared microscopy (RT s-SNIM) setup at FELBE. The room-temperature scattering scanning near-field infrared microscopy (RT s-SNIM), which is based on an home-built AFM, has been described in Section 4.3.2. Our s-SNIM study with the tunable CO<sub>2</sub> laser revealed a strong plasmonic resonance at about  $\hbar\omega = 126$  meV. This resonance has been found on MBE-grown GaAs/InGaAs core/shell NWs with a homogenous shell doping of about  $9 \times 10^{18} \text{ cm}^{-3}$ . By fitting the plasmonic resonance with the analytic point-dipole model (PDM), we could extract a carrier density of  $n = 8.3 \times 10^{18} \text{ cm}^{-3}$  and a mobility of  $\mu \approx 1000 \text{ cm}^2/\text{Vs}$ , which demonstrates the high quality of our NWs. Investigating the same NWs with intense FEL radiation reveals a pronounced redshift to  $\hbar\omega < 100$  meV and increased damping of the resonance. The observed nonlinear effect could be explained reasonably well by strong heating of the electron gas in the nonparabolic  $\Gamma$ -valley of InGaAs. Hence we could estimate a heating of the electron gas to  $T \approx 3900$  K during the FEL pulse, which causes the necessary increase in the effective mass by 75%. Measurements at different pulse durations and at constant pulse energy confirmed our hypothesis. The observed nonlinear effect is an interesting example system for investigating FEL-induced non-equilibrium states using s-SNIM. In our experiment pump and probe pulses have been in both cases the FEL itself. In the future, it would be interesting to synchronize another probe laser with the FEL in order to be able to investigate time-resolved non-equilibrium phenomena.

The final Section 4.4.2 of the work was devoted to the s-SNIM study of NW cross sections, conducted at RWTH Aachen. Here, the aim was to study the spatial localization of the plasmon within the cross section. To this end, we fabricated cross sections by FIB technique of the aforementioned core/shell NWs as well as modulation doped NWs. The s-SNIM images of all cross sections revealed a significant contrast. In particular, the modulation doped NWs showed a pronounced contrast within the cross section. Unfortunately, no pronounced spectral behavior with respect to a plasmonic resonance could be found in any of the cases. This fact may be due to the fabrication by means of FIB and subsequent damage to the NWs. Future efforts in this direction could therefore either try to change the FIB process or even consider an alternative method of

cutting cross sections. If it should be possible to detect charge carriers in the modulation doped NWs, an investigation at (different) low temperatures could be useful, since charge carriers could redistribute depending on the exact band structure.



## A Citation metrics

Figure A.1 (a) shows the citation metrics containing the terms “s-SNOM” and/or “s-SNIM”, as well as “nanospectroscopy” according to the *Web of Science*<sup>1</sup>. It demonstrates the tremendous increase of citations of about one order of magnitude within the last ten years. Note that “nanospectroscopy” actually also contains different methods/techniques than s-SNIM. However, it certainly demonstrates the increasing interest of the scientific community in s-SNIM or related techniques.

Figure A.1 (b) reveals the relative amount of citations according to the scientific discipline (for the term “s-SNIM” ). It becomes clear that in addition to materials science disciplines, physics, optics and nanosciences, s-SNIM is also commonly used in chemistry and physical chemistry. Biology, in which e. .g. optical (confocal) microscopy is used by default, is not represented here (or perhaps sorted into “multidisciplinary”).

---

<sup>1</sup><http://wokinfo.com/>

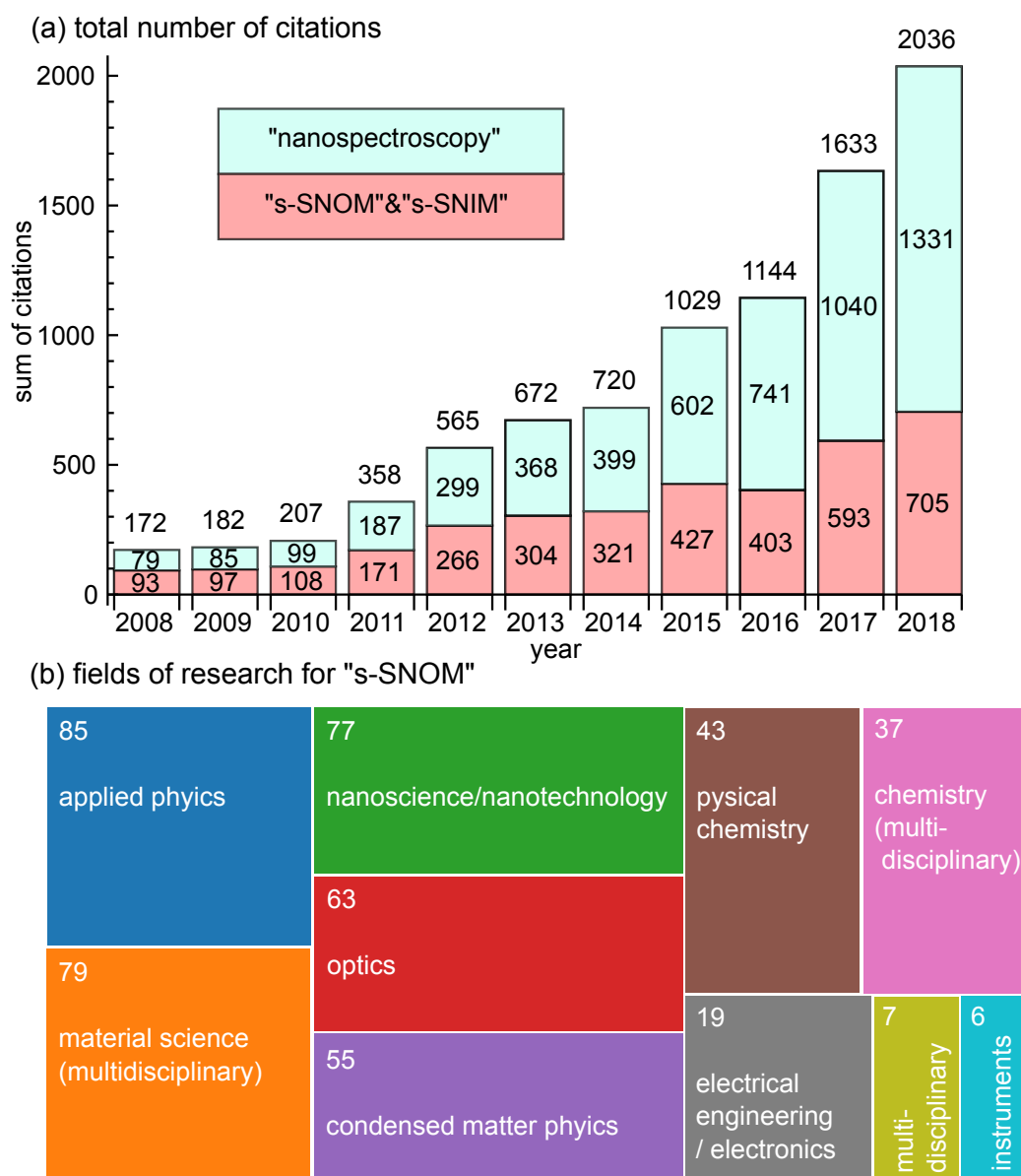


Figure A.1: (a) Citation metrics of the terms “s-SNOM” and/or “s-SNIM” (red) and “nanospectroscopy” (blue) according to the *Web of Science*. (b) Relative distribution of citations of “s-SNOM” to different scientific fields.



# B Additional nanospectroscopic studies

This chapter is dedicated to projects that could not be completed, show negative results for various reasons, or simply do not fit into the frame of the work. Nevertheless, the preliminary work in these areas may be helpful for future projects that are heading in a similar direction.

## B.1 Silicon carbide nanoparticle probes

The aim of this project is to fabricate resonant near-field probes for the mid-infrared (MIR) wavelength range, in particular for the wavelength range of the CO<sub>2</sub> laser of 9.6  $\mu\text{m}$  to 11.4  $\mu\text{m}$ , in order to significantly enhance the s-SNIM signal and thus also the sensitivity for non-resonant samples. According to the point-dipole model (PDM), the effective polarizability of a scattering sphere (in air) is given by Equation (2.12) of Section 2.2.2. A suitable material for the desired wavelength range is silicon carbide (SiC [137]) that has a strong phonon resonance [138–140] with  $\epsilon' = -2$  at  $\lambda = 10.8 \mu\text{m}$  [see Figure B.1 (a)]. Our approach to fabricate SiC probes for resonant s-SNIM is to attach SiC nanoparticles (NPs)<sup>1</sup> on standard Si tapping-mode AFM tips. Since the procedure of attaching Au NPs to Si tip was well known before, the procedure of attaching SiC NPs is closely oriented on it:

1. The SiC powder (1 mg) is dissolved in ethanol (20 ml) using an ultrasonic probe for about 1 h. Subsequently, about 5 drops of the solution are dropped on a glass (or Si) substrate and dried out by annealing at 250 °C for 2 h. A

---

<sup>1</sup>Nanopowder with SiC particles, primarily beta phase, diameter < 100 nm from Sigma Aldrich.

thin Au layer ( $\sim 1$  nm Cr,  $\sim 3$  nm Au) is now evaporated on the sample containing the SiC particles. The thin Au layer is later needed for bonding.

2. The AFM tip's end is flattened intentionally to have a defined,  $\sim 100$  nm wide plateau for collecting the NPs later on. This is achieved by controlled pressing of the tip against a Si sample in contact-mode AFM. The tip has to be imaged by SEM afterwards to check the plateau quality [see Figure B.1 (d)].
3. The "flattened" Si tip is dipped for 30 s into a solvent of 5 parts of distilled H<sub>2</sub>O to 1 part of the silane APTMS<sup>2</sup>. Afterwards, the tip is dipped for another 30 s into pure distilled H<sub>2</sub>O. The thin layer of the silane on the tip should ensure a strong chemical bonding in between the Si tip and the Au (the latter has been evaporated on the SiC before). This chemical procedure is based on the experience of attaching Au NPs in the group of Prof. L. Eng, TU Dresden.
4. Directly after the silane treatment, a individual SiC NP should be picked with the prepared tip. To this end, the sample containing the NPs is scanned in tapping-mode AFM to find a proper NP. The tip is now placed on the NP and pressed against it in contact mode. The same area is scanned again to ensure that the particle has disappeared and, hence, is now attached to the tip. If this is not the case, the picking should be tried again with more pressure or at another particle. Finally, the AFM tip with the attached NP should be checked again by SEM [see Figure B.1 (d)].

Although it was possible to produce at least one AFM tip with a single SiC NP attached, the procedure turned out to be very inefficient and no strongly enhanced s-SNIM signal could be found with the tip. The following list comments on the challenges that occurred concerning the steps in the previous list that would have to be solved in subsequent studies:

1. Although individual NPs were fabricated by using this method, the SiC powder still tends to form big clusters with a average size of several micrometers. This, later on, makes it difficult to find the (much fewer) individual

---

<sup>2</sup>(3-Aminopropyl)trimethoxysilane from Sigma Aldrich.

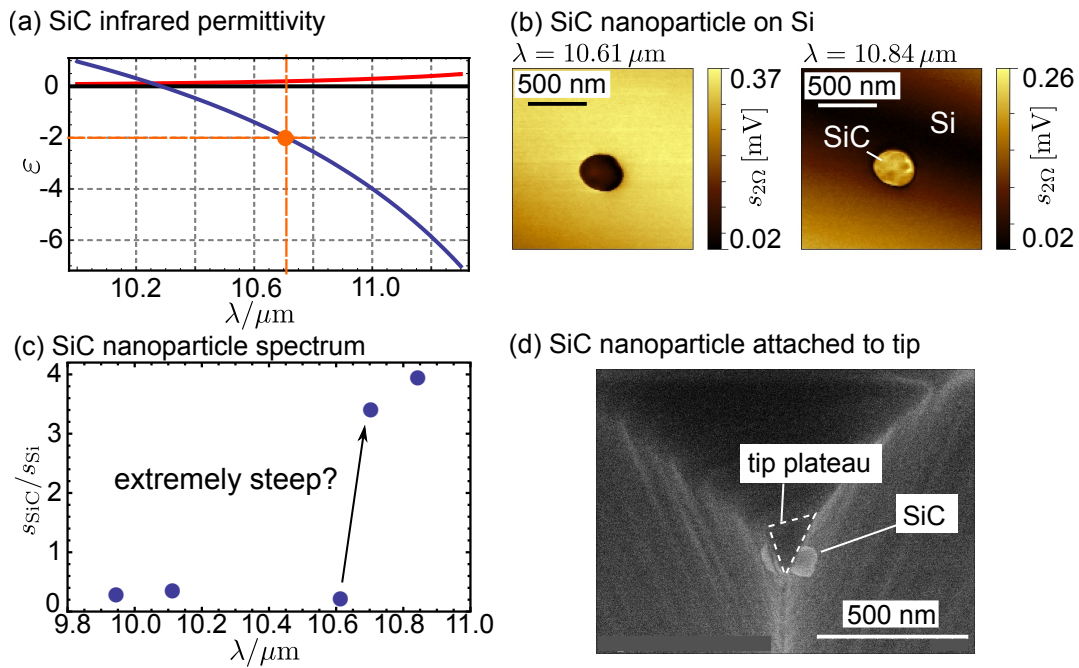


Figure B.1: (a) SiC infrared permittivity (real part=blue, imaginary part=red) including the Fröhlich resonance for  $\epsilon' = -2$  (orange). (b) s-SNIM maps of a SiC NP on Si substrate, revealing contrast reversal. (c) Spectrum of the SiC particle with respect to Si. The strong increase at  $\lambda \sim 10.7 \mu\text{m}$  fits to the resonance from (a). (d) SEM image of a SiC NP [not the same as in (b)] attached to a Si AFM tip.

NPs and also increases the probability to damage the tip. Figure B.1 (b) depicts the s-SNIM maps of a single nanoparticle on Si at  $\lambda = 10.61 \mu\text{m}$  and  $\lambda = 10.84 \mu\text{m}$ , measured with a conventional metal coated tip and the  $\text{CO}_2$  laser. Indeed, a contrast reversal occurs at the expected wavelength, as depicted in the spectrum in Figure B.1 (c).

2. The flattening of the tip is, generally, an unproblematic step. However, the subsequent control of every single tip *via* SEM is still necessary, which is time consuming and increases the risk of tip damage.
3. It is still unclear, how much of the silane is attached to the tip and if/how it could influence the s-SNIM performance. We were able to observe significant residues at some tips by SEM, which is probably due to the silane treatment.
4. The problem of the SiC cluster formation is critical at this point, since it is likely to attach the big clusters before finding a individual NP. Additionally, the particles often tend to attach at one side of the AFM tip plateau and not central at the end. The points mentioned here are the main reason why most of the produced tips are not useful.

Based on the observations we gained so far, we suggest to tackle the following issues:

- Find a better procedure to reliably produce well separated, individual NPs, i. e. suppress the formation of large clusters.
- Prove the SiC resonance by FTIR spectroscopy on the powder and further s-SNIM spectra on single NPs (i. e. increase the statistical evidence).
- Finally, prove the s-SNIM performance of a SiC probe in terms of resolution and signal strength both on non-resonant and resonant samples to confirm the predictions.

## B.2 Individual impurities in Si

Isolated atoms or ions, typically confined in traps, are ideal systems for studying fascinating coherent quantum effects such as photon echos. Likewise, isolated donor impurity atoms in semiconductors like silicon show a hydrogen-like spectrum, shifted to the far infrared due to the small effective mass and high dielectric constant [141]. Excited hydrogenic states are of particular interest for the development of quantum computation and quantum information, because they allow to prepare long living microscopic polarization states. For instance Greenland et al. demonstrated the coherent control of impurity wavefunctions in phosphorus-doped silicon (Si:P, see Fig. B.2) [73].

In contrast to previous far-field spectroscopy studies, which probed ensembles of many impurities, the aim of this project is to study individual impurity centers by means of low-temperature scattering scanning near-field infrared microscopy (LT s-SNIM). To this end, we investigate silicon samples containing different donors (P,Bi) or acceptors (Mg) with different defect densities, respectively. For instance, the low-temperature FTIR absorption spectra of Si:P and Si:Bi are depicted in Figure B.3(a) and (b). Both (a) and (b) show clear distinct peaks that can be attributed to the transitions (from the ground state to the respective marked state) of isolated impurities. The temperature dependence shows that the absorption drops drastically for temperatures  $> 30$  K, where the probability of electrons to get thermally excited to the conduction band increases. Hence, LT s-SNIM measurements should also be performed at  $T < 30$  K. The linewidth of the Si:Bi spectrum is much larger than for the Si:P since the donor density is about one order of magnitude larger for Si:Bi.

Even though the frequency of the transitions can be measured easily for all samples *via* low-temperature FTIR, there are several difficulties when it comes to s-SNIM measurements that are:

1. FTIR absorption spectra measure the bulk, whereas s-SNIM exclusively probes impurities close to the surface. The transition energies of these near-surface impurities could be shifted. Even more critically, the Fermi level pinning and the subsequent band bending at the surface may lead to a significant depletion of carriers at the surface. Approaches and attempts to overcome this surface depletion are described later.

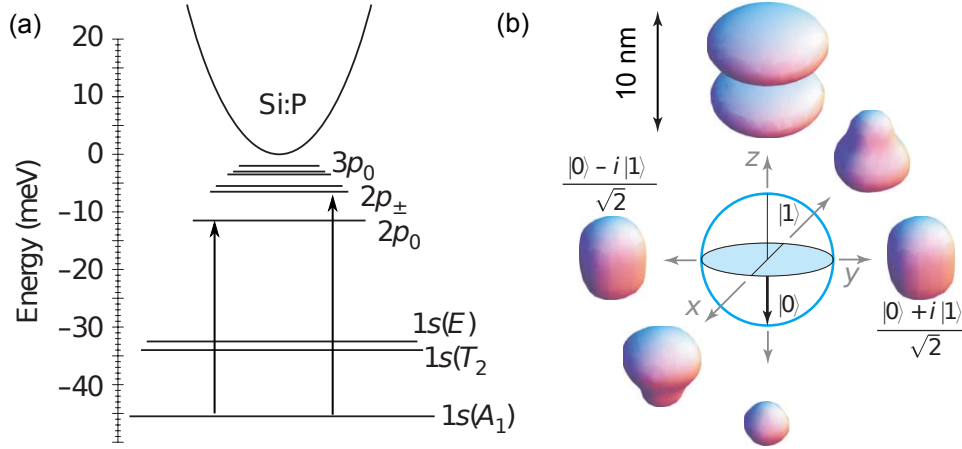


Figure B.2: (a) Energy level diagram for an isolated P donor in Si (Si:P). Only certain, sharp transition in the THz spectral range (e. g.  $1s(A_1) \rightarrow 2p_0$  at  $\sim 34$  meV) are allowed. (b) Bloch sphere with simulated wave packets, demonstrating the large spatial extent of  $\sim 10$  nm of the excited state  $|1\rangle$ . (Both images from [73]).

2. The effective size of the impurities is significantly smaller than the s-SNIM resolution. With a sufficiently large scattering cross section, it might still be possible to find a signature. Conceptually, an s-SNIM study on intersub-level transitions in quantum dots by Jacob et al. [29] is nearest. However, the contrast mechanism is not dealt with exactly, and a use of the simplified point-dipole model is questionable in this case. Therefore, a straightforward estimate of the expected s-SNIM response is hardly possible.
3. The impurity transitions are outside the spectral range of the CO<sub>2</sub> laser. Consequently, all measurements must be made with the FEL, whereby the restricted beam time and the significantly higher noise level must be taken into account. Specifically, the transitions in Si:P lie in an unfavorable spectral range for the far-infrared detector (see Section 3.3.3). Since we usually have to work with comparatively high laser powers of 20 mW to 50 mW (on the tip), there is also the danger that the defects are locally ionized.
4. In contrast to [29] there is no other AFM channel that can serve as an indicator for finding the lateral position of the impurities. However, a small signature may be possible in the KPFM signal: for example, Logowski et

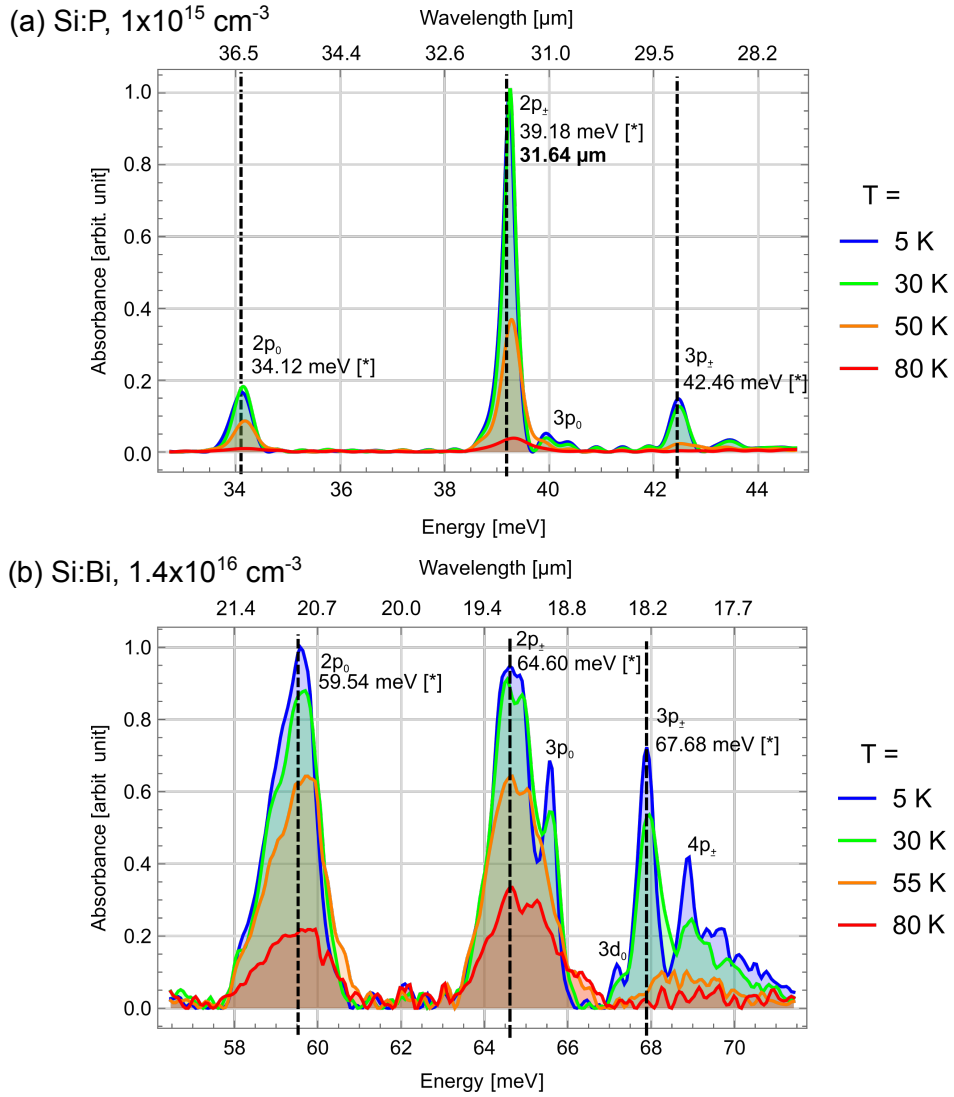


Figure B.3: (a) Absorption spectra of Si:P with  $n_{\text{P}} = 1 \times 10^{15} \text{ cm}^{-3}$  for different temperatures with assigned transitions. (b) Absorption spectra of Si:Bi with  $n_{\text{Bi}} = 1.4 \times 10^{16} \text{ cm}^{-3}$ . [For all spectra the background is subtracted and interference fringes of the Si substrate are filtered out.]

al. [142] claim that they have detected single impurities by means of LT KPFM. However, these measurements are based on a much higher doped sample and require excellent KPFM resolution.

There are several approaches to the first issue in the above list, i. e. how to passivate the surface:

- Thermal deposition of a thin layer of  $\text{SiO}_2$  on the surface. Unfortunately, a suitably thin thermal layer ( $< 50$  nm) could not be realized by the ion beam center.
- Illumination with visible light (with low penetration depth, e. g. green light) to repopulate the depleted area.
- A metal-insulator-semiconductor (MIS) structure as depicted by Figure B.4 (a) to be able to actively populate the surface by applying a bias.

The MIS structure [sketched in Figure B.4 (a)] has been realized, which required several processing steps:

1. Remove of the natural  $\text{SiO}_x$  layer of the doped Si sample with hydrofluoric acid.
2. Evaporate a thick Al layer (serves as ohmic back contact) on the sample back side, followed by annealing.
3. Remove the natural  $\text{SiO}_x$  layer again.
4. Sputter about 5 nm to 10 nm  $\text{SiO}_2$  on the top side.
5. Fabricate the Au top-gate structures on the  $\text{SiO}_2$  by electron beam lithography.

The basic idea of the top-gate structure is to leave a small gap so that the tip can get close to the Si and hence the impurities. In our sample, the gap distance varied from 0 to a about 10  $\mu\text{m}$ . Both the current-voltage characteristic [Figure B.4 (b)] as well as the capacitance-voltage characteristic (not shown) indeed show a typical behavior for a Schottky junction.



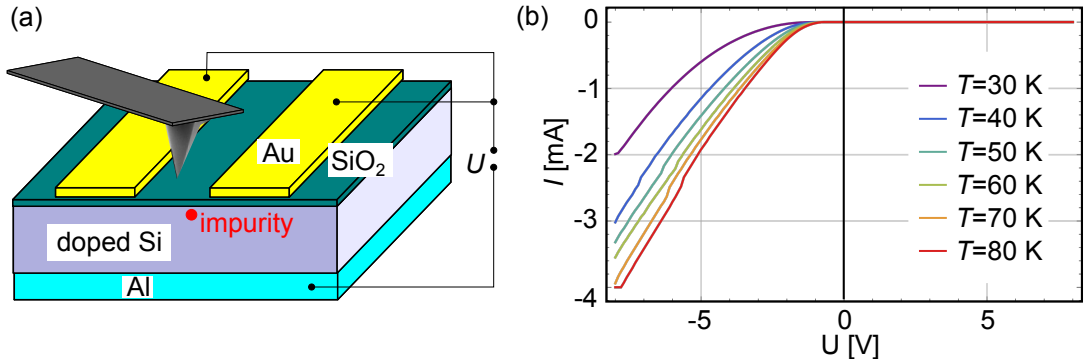


Figure B.4: (a) MOS gate structure for tuning of the surface depletion. (b)  $I(U)$  curves at low temperatures for a sample designed as proposed in (a).

In addition to the sample structure mentioned, we studied various other things by LT s-SNIM, e.g. different donors (Si), additional illumination, different temperatures, different reference structures (Si, Au), etc. Unfortunately, despite all efforts, no evidence for impurity transitions could be found in the s-SNIM measurements. In particular, the numerous possible difficulties (see list above) and the large parameter space (such as temperature, laser power and wavelength, bias voltage, bias illumination, etc.) make a systematic investigation very time consuming. In contrast, the FEL beam time, more specifically the time in which both FEL and LT s-SNIM together provide sufficient signal quality, is comparatively low. Therefore, we propose to perform this challenging experiment with a suitable table-top laser, allowing for a more thorough analysis of all possibilities, less laser power and higher signal stability.

## B.3 Surface phonon polaritons in molybdenum disulfide

The following introduction is adapted from our FEL beam time proposal, mainly written by T. Venanzi, HZDR:

“Layered van der Waals (vdW) crystals have attracted a lot of interest in the last decade. An appealing and promising application is the possibility to create heterostructures made of different materials bound to each other by vdW forces. This technology offers the possibility of engineering the physical properties of the samples. In the library of layered vdW materials, transition metal dichalcogenides (TMDs) are a very exciting class not only due to direct bandgap in the K-valley that is important for several optoelectronics applications [143], but also due to intriguing physical properties such as strong Coulomb interactions and distinctive spin valley physics [144].

Different studies have been performed with s-SNOM on TMDs but all of them have concentrated on the near-infrared detection of the photoluminescence (PL) from the exciton relaxation [145]. On the other hand Basov et al. [146] have studied the surface phonon polariton (SPhP) on few-layers (up to three layers) of hexagonal Boron Nitride (h-BN) by s-SNOM technique providing new and interesting knowledge about the phonon-light interaction in the near-field. SPhP are quasiparticles originated from the coupling of a phonon and a photon in polar crystals. More and more research is looking at SPhP because of the possibility of sub-diffraction limited light confinement, reduced optical losses with respect to surface plasmon polaritons and the possibility to use them in the mid-infrared and THz range.

For h-BN the phonon resonance is in the mid-infrared that is spectrally much easier to access. For TMDs, however, a FEL source at far-infrared wavelengths is needed.”

The MoS<sub>2</sub> sample has been prepared by mechanical exfoliation on a Si substrate. Hence, flakes with different sizes and thicknesses are randomly distributed over the sample. As depicted in Figure B.5, we could measure a clear dip in the s-SNIM signal at about 471 cm<sup>-1</sup>, which can be identified as the out-of-plane phonon (A<sub>2u</sub>) [147]. However, we found no such feature for the other in-plane phonon mode

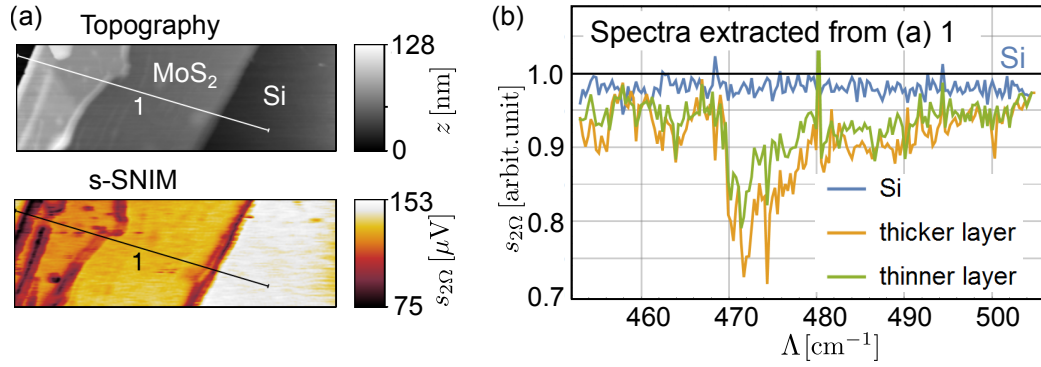


Figure B.5: (a) Topography and s-SNIM ( $\Lambda = 472 \text{ cm}^{-1}$ ) maps of a MoS<sub>2</sub> flake on Si substrate. (b) Spectra, extracted from line 1 of (a), normalized to Si, reveal a clear signature at the phonon resonance  $A_{2u}$ .

( $E_{1u}$ ) at  $385 \text{ cm}^{-1}$ , even though we tested both p-polarization and s-polarization. Finally, no clear indication of the SPhP could be found. The small response in the s-SNIM signal suggests that the phonon resonances are actually very weak. Recently, near-field spectra have been published by Kathib et al. [148], showing also a very weak spectral contrast even for thick layers.



# C Derivation of the nonparabolic effective mass and density of states

## C.1 Effective mass

The most common definition of the effective mass is given by the second derivative of the dispersion relation:

$$m^* = \left( \frac{\partial^2 \mathcal{E}}{\partial p^2} \right)^{-1}, \quad (\text{C.1})$$

where  $p = \hbar k$  is the momentum. However, this definition is only useful for a parabolic approximation while an alternative definition is suggested for the nonparabolic case.

An alternative approach is sketched, for example, by Ariel et al. in [133], starting with the momentum of a one-dimensional wave-packet:

$$p = m^* v_g, \quad (\text{C.2})$$

where  $v_g = \partial \mathcal{E} / \partial p$  is the group velocity and  $m^*$  is the effective mass. Hence, we can define the effective mass to

$$m^* = p \left( \frac{\partial \mathcal{E}}{\partial p} \right)^{-1}. \quad (\text{C.3})$$

For example, by applying Equation (C.3) to the relativistic dispersion  $\mathcal{E}^2 = (pc)^2 + (m_0 c^2)^2$ , where  $m_0 c^2$  is constant, we get the correct relation  $m^* = p/c$  [in contrast to Equation (C.1)]. Equation (C.3) also holds for a linear isotropic dispersion, such as in the vicinity of the Dirac point in graphene.

In our case, applying Equation C.3 to the nonparabolic dispersion  $\mathcal{E}(1 + \alpha\mathcal{E}) = \hbar^2 k^2 / (2m_\Gamma)$  results in the linear dependence

$$m(\mathcal{E}) = m_\Gamma(1 + 2\alpha\mathcal{E}) . \quad (\text{C.4})$$

## C.2 Density of states

In the following, a derivation of the density of states (DOS) for a parabolic dispersion relation  $\mathcal{E} = (\hbar k)^2 / (2m^*)$  is sketched. The calculation of the non-parabolic case then takes place analogously with the corresponding dispersion relation.

The three-dimensional DOS for a parabolic dispersion  $\mathcal{E} = (\hbar k)^2 / (2m^*)$  is described as

$$n(\mathcal{E}) = \frac{N(\mathcal{E})}{V} = \frac{1}{2\pi^2} \left( \frac{2m^*}{\hbar^2} \right)^{3/2} \sqrt{\mathcal{E}} , \quad (\text{C.5})$$

where  $m^*$  is the effective mass at the  $\Gamma$  point.

The derivation of Equation (C.5) uses

$$N(k) dk = \left( \frac{V k^2}{\pi^2} \right) dk \quad (\text{C.6})$$

as a result of the number of  $k$  states within a spherical shell, where each  $k$  state can hold two electrons of opposite spins and, moreover, wave functions differing only in sign are indistinguishable. Now we consider the dispersion relation and its derivative to  $\mathcal{E}$ :

$$k^2 = \frac{2m^* \mathcal{E}}{\hbar^2} \quad (\text{C.7})$$

$$(2k) dk = \frac{2m^*}{\hbar^2} d\mathcal{E} . \quad (\text{C.8})$$

Combining the two latter Equations (C.7) and (C.8) leads to

$$dk = \frac{m^*}{\hbar \sqrt{2m^* \mathcal{E}}} d\mathcal{E} . \quad (\text{C.9})$$

Plugging both (C.7) and (C.9) into (C.6) results in the DOS (C.5):

$$\begin{aligned}
 N(k) dk &= \frac{V}{\pi^2} k^2 \frac{m^*}{\hbar \sqrt{2m^* E}} d\mathcal{E} \\
 &= \frac{V}{2m^*} \frac{2m^* \mathcal{E}}{\hbar^2} \frac{m^*}{\hbar \sqrt{2m^* \mathcal{E}}} d\mathcal{E} \\
 &= \frac{V}{2\pi^2} \underbrace{\left( \frac{2m^*}{\hbar^2} \right)^{3/2}}_{=N(\mathcal{E})} \sqrt{\mathcal{E}} d\mathcal{E} .
 \end{aligned} \tag{C.10}$$

Likewise, the nonparabolic DOS can be deduced by substituting the dispersion (C.7) by the nonparabolic approach:

$$k^2 = \frac{2m^* \mathcal{E} (1 + \alpha \mathcal{E})}{\hbar^2} \tag{C.11}$$

$$\hbar^2 k dk = m^* (1 + 2\alpha \mathcal{E}) d\mathcal{E} , \tag{C.12}$$

where  $\alpha$  is the nonparabolicity factor. Combining both Equations (C.11) and (C.12) results in

$$dk = \frac{m^* (1 + 2\alpha \mathcal{E})}{\hbar \sqrt{2m^* \mathcal{E} (1 + \alpha \mathcal{E})}} d\mathcal{E} . \tag{C.13}$$

Finally, using Equations (C.6), (C.11), and (C.13), we find the DOS for the nonparabolic dispersion:

$$\begin{aligned}
 N(k) dk &= \frac{V}{\pi^2} \frac{2m^* \mathcal{E} (1 + \alpha \mathcal{E})}{\hbar^2} \frac{m (1 + 2\alpha \mathcal{E})}{\hbar \sqrt{2m^* \mathcal{E} (1 + \alpha \mathcal{E})}} d\mathcal{E} \\
 &= (...) \\
 &= \frac{V}{2\pi^2} \underbrace{\left( \frac{2m^*}{\hbar^2} \right)^{3/2} \sqrt{\mathcal{E} (1 + \alpha \mathcal{E})} (1 + 2\alpha \mathcal{E})}_{=N(\mathcal{E})} d\mathcal{E} .
 \end{aligned} \tag{C.14}$$

A comparison between the parabolic (C.10) and nonparabolic (C.14) DOS in particular shows that both DOS are the equivalent for  $\alpha = 0$ .





# D Comparison of self-homodyne and pseudo-heterodyne detection

Non-interferometric s-SNIM (also denoted as self-homodyne) detects a mixed signal of both scattered amplitude  $s$  and phase  $\phi$ , as discussed in Section 2.2.4. In contrast, pseudo-heterodyne detection utilizes the interference of the scattered signal to a well defined reference signal, which enables the separation of the optical amplitude and phase.

We can compare both detection schemes –self-homodyne and pseudo-heterodyne– by the *Neaspec* setup, which we used for the NW cross section sample in Section 4.4.2. The pseudo-heterodyne detection, e. g. described in Reference [57], is the standard s-SNIM mode for the *Neaspec*. Here, we detect both the pseudo-heterodyne amplitude  $s^{\text{ph}}$  and phase  $\phi^{\text{ph}}$ , as depicted in Figures D.1 (a) and (b). The amplitude map shows a clear contrast for the cross sections, where the signal of the latter is lower than the Si at the top of the image. The phase, however, shows a blurred contrast at all cross sections. Figure D.1 (c) depicts the map recorded by self-homodyne detection, where we blocked the reference arm of the interferometer. The contrast is, in this case, not directly comparable to either Figure D.1 (a) or (b). In particular, the cross sections appear significantly brighter than the Si, with the entire image overlaid unevenly.

However, it turns out that we can reproduce image (c) quite accurately by mixing the interferometric amplitude and phase signals properly. According to Equation (2.25), we can apply

$$s^{\text{ph}} \cos(\phi^{\text{ph}} - 2.6) , \tag{D.1}$$

where  $s^{\text{ph}}$  is the pseudo-heterodyne amplitude,  $\phi^{\text{ph}}$  is the pseudo-heterodyne phase, and 2.6 is an phase value that we choose intentionally to match the con-

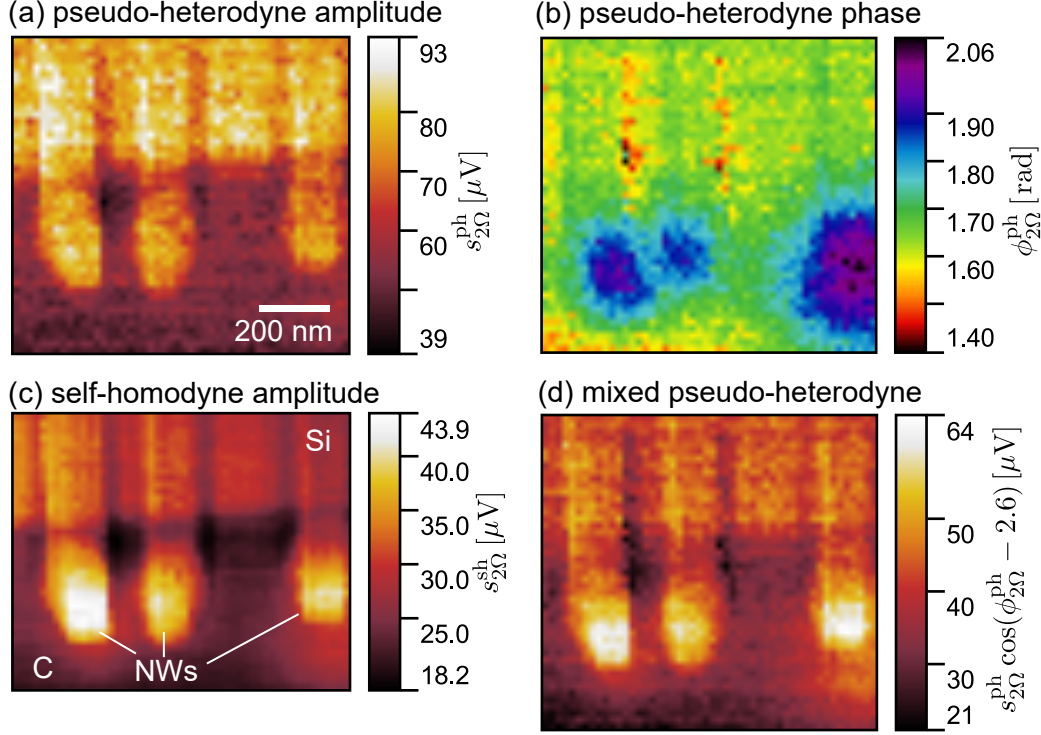


Figure D.1: S-SNIM measurements on GaAs/InGaAs core/shell NW cross sections at  $\hbar\omega = 108$  meV: (a) Amplitude  $s_{2\Omega}^{\text{ph}}$  and (b) phase  $\phi_{2\Omega}^{\text{ph}}$  for pseudo-heterodyne detection. (c) amplitude  $s_{2\Omega}^{\text{sh}}$  for self-homodyne detection, i. e. blocked reference arm. (d) Mixed amplitude and phase signal calculated from (a), (b), and an fitting background offset, reproducing the contrast of (c).

trast. The latter should correspond to the unknown background phase that we assume constant here. As depicted by Figure D.1 (d), this mixing can principally reproduce the contrast of the self-homodyne detection<sup>1</sup>.

Note that we also checked the strong plasmonic resonance of the GaAs/InGaAs core/shell NWs lying flat on Si. Here, the spectral behavior for both self-homodyne and pseudo-heterodyne detection is very similar. However, spatial modulations in the signal seem to occur more likely for self-homodyne detection, hence yielding a further uncertainty (beside the phase mixing).

<sup>1</sup>Apart from a further background interference, which is superimposed only in the self-homodyne amplitude of of Figure D.1 (c).





# Bibliography

- [1] E. Synge, “A suggested method for extending microscopic resolution into the ultra-microscopic region”, *The London, Edinburgh, and Dublin Philosophical Magazine and Journal of Science* **6**, 356–362 (1928).
- [2] L. Novotny, “The History of Near-field Optics”, in *Progress in optics*, edited by E. Wolf (Elsevier, Amsterdam, 2007) Chap. 5, pp. 137–184.
- [3] G. Binnig, C. F. Quate, and C. Gerber, “Atomic Force Microscope”, *Physical Review Letters* **56**, 930–933 (1986).
- [4] T. Taubner, D. Korobkin, Y. Urzhumov, G. Shvets, and R. Hillenbrand, “Near-Field Microscopy Through a SiC Superlens”, *Science* **313**, 1595–1595 (2006).
- [5] S. C. Kehr, Y. Liu, L. Martin, P. Yu, M. Gajek, S.-Y. Yang, C.-H. Yang, M. Wenzel, R. Jacob, H.-G. von Ribbeck, M. Helm, X. Zhang, L. M. Eng, and R. Ramesh, “Near-field examination of perovskite-based superlenses and superlens-enhanced probe-object coupling”, *Nature Communications* **2**, 249 (2011).
- [6] B. J. Bohn, M. Schnell, M. A. Kats, F. Aieta, R. Hillenbrand, and F. Capasso, “Near-Field Imaging of Phased Array Metasurfaces”, *Nano Letters* **15**, 3851–3858 (2015).
- [7] G. X. Ni, H. Wang, J. S. Wu, Z. Fei, M. D. Goldflam, F. Keilmann, B. Özyilmaz, A. H. Castro Neto, X. M. Xie, M. M. Fogler, and D. N. Basov, “Plasmons in graphene moiré superlattices”, *Nature Materials* **14**, 1217–22 (2015).

- 
- [8] M. A. Huber, F. Mooshammer, M. Plankl, L. Viti, F. Sandner, L. Z. Kastner, T. Frank, J. Fabian, M. S. Vitiello, T. L. Cocker, and R. Huber, “Femtosecond photo-switching of interface polaritons in black phosphorus heterostructures”, *Nature Nanotechnology* **12**, 207–211 (2016).
- [9] D. N. Basov, M. M. Fogler, and F. J. Garcia de Abajo, “Polaritons in van der Waals materials”, *Science* **354**, aag1992 (2016).
- [10] G. X. Ni, A. S. McLeod, Z. Sun, L. Wang, L. Xiong, K. W. Post, S. S. Sunku, B. Y. Jiang, J. Hone, C. R. Dean, M. M. Fogler, and D. N. Basov, “Fundamental limits to graphene plasmonics”, *Nature* **557**, 530–533 (2018).
- [11] A. J. Huber, F. Keilmann, J. Wittborn, J. Aizpurua, and R. Hillenbrand, “Terahertz Near-Field Nanoscopy of Mobile Carriers in Single Semiconductor Nanodevices”, *Nano Letters* **8**, 3766–3770 (2008).
- [12] J. M. Stiegler, A. J. Huber, S. L. Diedenhofen, J. Gomez Rivas, R. E. Algra, E. P. A. M. Bakkers, and R. Hillenbrand, “Nanoscale Free-Carrier Profiling of Individual Semiconductor Nanowires by Infrared Near-Field Nanoscopy”, *Nano Letters* **10**, 1387–1392 (2010).
- [13] A. S. McLeod, E. van Heumen, J. G. Ramirez, S. Wang, T. Saerbeck, S. Guenon, M. Goldflam, L. Anderegg, P. Kelly, A. Mueller, M. K. Liu, I. K. Schuller, and D. N. Basov, “Nanotextured phase coexistence in the correlated insulator  $V_2O_3$ ”, *Nature Physics* **13**, 80–86 (2016).
- [14] M. Eisele, T. L. Cocker, M. A. Huber, M. Plankl, L. Viti, D. Ercolani, L. Sorba, M. S. Vitiello, and R. Huber, “Ultrafast multi-terahertz nanospectroscopy with sub-cycle temporal resolution”, *Nature Photonics* **8**, 841–845 (2014).
- [15] M. Wagner, A. S. McLeod, S. J. Maddox, Z. Fei, M. Liu, R. D. Averitt, M. M. Fogler, S. R. Bank, F. Keilmann, and D. N. Basov, “Ultrafast Dynamics of Surface Plasmons in InAs by Time-Resolved Infrared Nanospectroscopy”, *Nano Letters* **14**, 4529–4534 (2014).
- [16] H. U. Yang, E. Hebestreit, E. E. Josberger, and M. B. Raschke, “A cryogenic scattering-type scanning near-field optical microscope”, *Review of Scientific Instruments* **84**, 023701 (2013).

- 
- [17] G. Binnig and H. Rohrer, “Scanning tunneling microscopy”, *Surface Science* **126**, 236–244 (1983).
- [18] J. E. Jones, “On the Determination of Molecular Fields — II. From the Equation of State of a Gas”, *Proceedings of the Royal Society A: Mathematical, Physical and Engineering Sciences* **106**, 463–477 (1924).
- [19] R. A. Buckingham, “The Classical Equation of State of Gaseous Helium, Neon and Argon”, *Proceedings of the Royal Society A: Mathematical, Physical and Engineering Sciences* **168**, 264–283 (1938).
- [20] P. J. James, M. Antognozzi, J. Tamayo, T. J. McMaster, J. M. Newton, and M. J. Miles, “Interpretation of Contrast in Tapping Mode AFM and Shear Force Microscopy. A Study of Nafion”, *Langmuir* **17**, 349–360 (2001).
- [21] P. Güthner and K. Dransfeld, “Local poling of ferroelectric polymers by scanning force microscopy”, *Applied Physics Letters* **61**, 1137–1139 (1992).
- [22] E. Soergel, “Piezoresponse force microscopy”, *Journal of Applied Physics D* **44**, 464003 (2010).
- [23] R. Nath, S. Hong, J. A. Klug, A. Imre, M. J. Bedzyk, R. S. Katiyar, and O. Auciello, “Effects of cantilever buckling on vector piezoresponse force microscopy imaging of ferroelectric domains in BiFeO<sub>3</sub> nanostructures”, *Applied Physics Letters* **96**, 163101 (2010).
- [24] M. Nonnenmacher, M. P. O’Boyle, and H. K. Wickramasinghe, “Kelvin probe force microscopy”, *Applied Physics Letters* **58**, 2921–2923 (1991).
- [25] U. Zerweck, C. Loppacher, T. Otto, S. Grafström, and L. M. Eng, “Accuracy and resolution limits of Kelvin probe force microscopy”, *Physical Review B* **71**, 1–9 (2005).
- [26] W. Melitz, J. Shen, A. C. Kummel, and S. Lee, “Kelvin probe force microscopy and its application”, *Surface Science Reports* **66**, 1–27 (2011).
- [27] L. Jung, B. Hauer, P. Li, M. Bornhöfft, J. Mayer, and T. Taubner, “Exploring the detection limits of infrared near-field microscopy regarding small buried structures and pushing them by exploiting superlens-related effects”, *Optics Express* **24**, 4431 (2016).

- 
- [28] T. Taubner, F. Keilmann, and R. Hillenbrand, “Nanoscale-resolved sub-surface imaging by scattering-type near-field optical microscopy”, *Optics Express* **13**, 8893 (2005).
- [29] R. Jacob, S. Winnerl, M. Fehrenbacher, J. Bhattacharyya, H. Schneider, M. T. Wenzel, H.-G. von Ribbeck, L. M. Eng, P. Atkinson, O. G. Schmidt, and M. Helm, “Intersublevel Spectroscopy on Single InAs-Quantum Dots by Terahertz Near-Field Microscopy”, *Nano Letters* **12**, 4336–4340 (2012).
- [30] R. Krutokhvostov, A. A. Govyadinov, J. M. Stiegler, F. Huth, A. Chuvilin, P. S. Carney, and R. Hillenbrand, “Enhanced resolution in subsurface near-field optical microscopy”, *Optics Express* **20**, 593 (2012).
- [31] A. P. Engelhardt, B. Hauer, and T. Taubner, “Visibility of weak contrasts in subsurface scattering near-field microscopy”, *Ultramicroscopy* **126**, 40–43 (2013).
- [32] K. Moon, H. Park, J. Kim, Y. Do, S. Lee, G. Lee, H. Kang, and H. Han, “Subsurface Nanoimaging by Broadband Terahertz Pulse Near-Field Microscopy”, *Nano Letters* **15**, 549–552 (2015).
- [33] R. Hillenbrand, T. Taubner, and F. Keilmann, “Phonon-enhanced light-matter interaction at the nanometre scale”, *Nature* **418**, 159–162 (2002).
- [34] E. Abbe, “Beiträge zur Theorie des Mikroskops und der mikroskopischen Wahrnehmung”, *Archiv für Mikroskopische Anatomie* **9**, 413–418 (1873).
- [35] R. S. Lord Rayleigh, “On the theory of optical images, with special reference to the microscope”, *The London, Edinburgh, and Dublin Philosophical Magazine and Journal of Science*, **42**, 167–195 (1896).
- [36] M. J. Nasse and J. C. Woehl, “Realistic modeling of the illumination point spread function in confocal scanning optical microscopy”, *Journal of the Optical Society of America A* **27**, 295 (2010).
- [37] S. W. Hell and J. Wichmann, “Breaking the diffraction resolution limit by stimulated emission: stimulated-emission-depletion fluorescence microscopy”, *Optics Letters* **19**, 780–782 (1994).
- [38] T. A. Klar and S. W. Hell, “Subdiffraction resolution in far-field fluorescence microscopy”, *Optics Letters* **24**, 954 (1999).



- 
- [39] B. Knoll and F. Keilmann, “Electromagnetic fields in the cutoff regime of tapered metallic waveguides”, *Optics Communications* **162**, 177–181 (1999).
- [40] B. Knoll and F. Keilmann, “Enhanced dielectric contrast in scattering-type scanning near-field optical microscopy”, *Optics Communications* **182**, 321–328 (2000).
- [41] F. Keilmann and R. Hillenbrand, “Near-field microscopy by elastic light scattering from a tip”, *Philosophical Transactions of the Royal Society of London. Series A: Mathematical, Physical and Engineering Sciences* **362**, edited by D. Richards and A. Zayats, 787–805 (2004).
- [42] F. Kuschewski, H.-G. von Ribbeck, J. Döring, S. Winnerl, L. M. Eng, and S. C. Kehr, “Narrow-band near-field nanoscopy in the spectral range from 1.3 to 8.5 THz”, *Applied Physics Letters* **108**, 113102 (2016).
- [43] X. Fan, W. Zheng, and D. J. Singh, “Light scattering and surface plasmons on small spherical particles”, *Light: Science & Applications* **3**, e179 (2014).
- [44] J. D. Jackson, *Classical Electrodynamics* (John Wiley and Sons, 1999).
- [45] G. Mie, “Beiträge zur Optik trüber Medien, speziell kolloidaler Metallösungen”, *Annalen der Physik* **330**, 377–445 (1908).
- [46] C. F. Bohren and D. R. Huffman, *Absorption and Scattering of Light by Small Particles* (Wiley-VCH Verlag GmbH, Weinheim, Germany, 1998).
- [47] S. C. Kehr, “Scattering Scanning Near-Field Optical Microscopy on Anisotropic Dielectrics”, PhD thesis (Technische Universität Dresden, 2007).
- [48] T. Taubner, F. Keilmann, and R. Hillenbrand, “Nanomechanical Resonance Tuning and Phase Effects in Optical Near-Field Interaction”, *Nano Letters* **4**, 1669–1672 (2004).
- [49] S. C. Kehr, M. Cebula, O. Mieth, T. Härtling, J. Seidel, S. Grafström, L. M. Eng, S. Winnerl, D. Stehr, and M. Helm, “Anisotropy Contrast in Phonon-Enhanced Apertureless Near-Field Microscopy Using a Free-Electron Laser”, *Physical Review Letters* **100**, 256403 (2008).

- 
- [50] S. C. Schneider, S. Grafström, and L. M. Eng, “Scattering near-field optical microscopy of optically anisotropic systems”, *Physical Review B* **71**, 115418 (2005).
- [51] R. Jacob, S. Winnerl, H. Schneider, M. Helm, M. T. Wenzel, H.-G. von Ribbeck, L. M. Eng, and S. C. Kehr, “Quantitative determination of the charge carrier concentration of ion implanted silicon by IR-near-field spectroscopy”, *Optics Express* **18**, 26206–13 (2010).
- [52] D. E. Tranca, S. G. Stanciu, R. Hristu, C. Stoichita, S. A. M. Tofail, and G. A. Stanciu, “High-resolution quantitative determination of dielectric function by using scattering scanning near-field optical microscopy”, *Scientific Reports* **5**, 11876 (2015).
- [53] P. Patoka, G. Ulrich, A. E. Nguyen, L. Bartels, P. A. Dowben, V. Turkowski, T. S. Rahman, P. Hermann, B. Kastner, A. Hoehl, G. Ulm, and E. Ruhl, “Nanoscale plasmonic phenomena in CVD-grown MoS<sub>2</sub> monolayer revealed by ultra-broadband synchrotron radiation based nano-FTIR spectroscopy and near-field microscopy”, *Optics Express* **24**, 1154–1164 (2016).
- [54] A. Cvitkovic, N. Ocelic, and R. Hillenbrand, “Analytical model for quantitative prediction of material contrasts in scattering-type near-field optical microscopy”, *Optics Express* **15**, 8550–8565 (2007).
- [55] J. Döring, “Low-temperature scattering-type scanning near-field optical microscopy on ferroelectrics”, PhD thesis (Technische Universität Dresden, 2017).
- [56] A. J. Sternbach, J. Hinton, T. Slusar, A. S. McLeod, M. K. Liu, A. Frenzel, M. Wagner, R. Iraheta, F. Keilmann, A. Leitenstorfer, M. Fogler, H.-T. Kim, R. D. Averitt, and D. N. Basov, “Artifact free time resolved near-field spectroscopy”, *Optics Express* **25**, 28589 (2017).
- [57] N. Ocelic, A. Huber, and R. Hillenbrand, “Pseudoheterodyne detection for background-free near-field spectroscopy”, *Applied Physics Letters* **89**, 101124 (2006).
- [58] P. Li, T. Wang, H. Böckmann, and T. Taubner, “Graphene-Enhanced Infrared Near-Field Microscopy”, *Nano Letters* **14**, 4400–4405 (2014).

- [59] M. Fehrenbacher, S. Winnerl, H. Schneider, J. Döring, S. C. Kehr, L. M. Eng, Y. Huo, O. G. Schmidt, K. Yao, Y. Liu, and M. Helm, “Plasmonic superlensing in doped GaAs”, *Nano Letters* **15**, 1057–1061 (2015).
- [60] S. C. Kehr, R. G. P. McQuaid, L. Ortman, T. Kämpfe, F. Kuschewski, D. Lang, J. Döring, J. M. Gregg, and L. M. Eng, “A Local Superlens”, *ACS Photonics* **3**, 20–26 (2015).
- [61] D. Lang, J. Döring, T. Nörenberg, Á. Butykai, I. Kézsmárki, H. Schneider, S. Winnerl, M. Helm, S. C. Kehr, and L. M. Eng, “Infrared nanoscopy down to liquid helium temperatures”, *Review of Scientific Instruments* **89**, 033702 (2018).
- [62] J. Döring, D. Lang, F. Kuschewski, L. Wehmeier, T. Nörenberg, L. M. Eng, and S. C. Kehr, “Low-temperature nanospectroscopy of the structural ferroelectric phases in single-crystalline barium titanate”, *Nanoscale* **10**, 18074–18079 (2018).
- [63] M. Wagner, Z. Fei, A. S. McLeod, A. S. Rodin, W. Bao, E. G. Iwinski, Z. Zhao, M. Goldflam, M. Liu, G. Dominguez, M. Thiemens, M. M. Fogler, A. H. Castro Neto, C. N. Lau, S. Amarie, F. Keilmann, and D. N. Basov, “Ultrafast and Nanoscale Plasmonic Phenomena in Exfoliated Graphene Revealed by Infrared Pump–Probe Nanoscopy”, *Nano Letters* **14**, 894–900 (2014).
- [64] G. X. Ni, L. Wang, M. D. Goldflam, M. Wagner, Z. Fei, A. S. McLeod, M. K. Liu, F. Keilmann, B. Özyilmaz, A. H. Castro Neto, J. Hone, M. M. Fogler, and D. N. Basov, “Ultrafast optical switching of infrared plasmon polaritons in high-mobility graphene”, *Nature Photonics* **10**, 244–247 (2016).
- [65] K. F. Renk, *Basics of Laser Physics* (Springer Berlin Heidelberg, 2012).
- [66] C. W. Roberson and P. Sprangle, “A review of free-electron lasers”, *Physics of Fluids B: Plasma Physics* **1**, 3–42 (1989).
- [67] Z. Huang and K. J. Kim, “Review of x-ray free-electron laser theory”, *Physical Review Special Topics - Accelerators and Beams* **10**, 034801 (2007).

- [68] J. Döring, H.-G. von Ribbeck, M. Fehrenbacher, S. C. Kehr, and L. M. Eng, “Near-field resonance shifts of ferroelectric barium titanate domains upon low-temperature phase transition”, *Applied Physics Letters* **105**, 053109 (2014).
- [69] J. Döring, L. M. Eng, and S. C. Kehr, “Low-temperature piezoresponse force microscopy on barium titanate”, *Journal of Applied Physics* **120**, 084103 (2016).
- [70] L. Ozyuzer, A. E. Koshelev, C. Kurter, N. Gopalsami, Q. Li, M. Tachiki, K. Kadowaki, T. Yamamoto, H. Minami, H. Yamaguchi, T. Tachiki, K. E. Gray, W.-K. Kwok, and U. Welp, “Emission of Coherent THz Radiation from Superconductors”, *Science* **318**, 1291–1293 (2007).
- [71] D. Ahmad, B. H. Min, Y. I. Seo, W. J. Choi, S.-I. Kimura, J. Seo, and Y. S. Kwon, “Superconducting states study in electron-overdoped  $\text{BaFe}_{1.8}\text{Co}_{0.2}\text{As}_2$  using terahertz and far-infrared spectroscopy”, *Superconductor Science and Technology* **28**, 075002 (2015).
- [72] B. Pajot, *Optical Absorption of Impurities and Defects in Semiconducting Crystals*, Vol. 158, Springer Series in Solid-State Sciences (Springer Berlin Heidelberg, 2010).
- [73] P. T. Greenland, S. A. Lynch, A. F. G. van der Meer, B. N. Murdin, C. R. Pidgeon, B. Redlich, N. Q. Vinh, and G. Aepli, “Coherent control of Rydberg states in silicon”, *Nature* **465**, 1057–1061 (2010).
- [74] S. W. Wu, N. Ogawa, and W. Ho, “Atomic-Scale Coupling of Photons to Single-Molecule Junctions”, *Science* **312**, 1362–1365 (2006).
- [75] N. Jiang, E. T. Foley, J. M. Klingsporn, M. D. Sonntag, N. A. Valley, J. A. Dieringer, T. Seideman, G. C. Schatz, M. C. Hersam, and R. P. Van Duyne, “Observation of multiple vibrational modes in ultrahigh vacuum tip-enhanced Raman spectroscopy combined with molecular-resolution scanning tunneling microscopy”, *Nano Letters* **12**, 5061–5067 (2012).
- [76] R. Zhang, Y. Zhang, Z. C. Dong, S. Jiang, C. Zhang, L. G. Chen, L. Zhang, Y. Liao, J. Aizpurua, Y. Luo, J. L. Yang, and J. G. Hou, “Chemical mapping of a single molecule by plasmon-enhanced Raman scattering”, *Nature* **498**, 82–86 (2013).

- [77] T. L. Cocker, D. Peller, P. Yu, J. Repp, and R. Huber, “Tracking the ultrafast motion of a single molecule by femtosecond orbital imaging”, *Nature* **539**, 263–267 (2016).
- [78] S. Li, S. Chen, J. Li, R. Wu, and W. Ho, “Joint Space-Time Coherent Vibration Driven Conformational Transitions in a Single Molecule”, *Physical Review Letters* **119**, 1–5 (2017).
- [79] I. C. Moldovan-Doyen, G. Xu, L. Greusard, G. Sevin, E. Strupiechonski, G. Beaudoin, I. Sagnes, S. P. Khanna, E. H. Linfield, A. G. Davies, R. Colombelli, and Y. De Wilde, “Low temperature near-field scanning optical microscopy on infrared and terahertz photonic-crystal quantum cascade lasers”, *Applied Physics Letters* **98**, 231112 (2011).
- [80] R. L. Olmon, B. Slovick, T. W. Johnson, D. Shelton, S.-H. Oh, G. D. Boreman, and M. B. Raschke, “Optical dielectric function of gold”, *Physical Review B* **86**, 235147 (2012).
- [81] D. Chandler-Horowitz and P. M. Amiratharaj, “High-accuracy, midinfrared ( $450\text{ cm}^{-1} \leq \omega \leq 4000\text{ cm}^{-1}$ ) refractive index values of silicon”, *Journal of Applied Physics* **97**, 123526 (2005).
- [82] R. Kitamura, L. Pilon, and M. Jonasz, “Optical constants of silica glass from extreme ultraviolet to far infrared at near room temperature”, *Applied Optics* **33**, 8118–8133 (2007).
- [83] S. Reschke, F. Mayr, Z. Wang, P. Lunkenheimer, W. Li, D. Szaller, S. Bordács, I. Kézsmárki, V. Tsurkan, and A. Loidl, “Optical conductivity in multiferroic  $\text{GaV}_4\text{S}_8$  and  $\text{GeV}_4\text{S}_8$ : Phonons and electronic transitions”, *Physical Review B* **96**, 144302 (2017).
- [84] J. Hlinka, F. Borodavka, I. Rafalovskyi, Z. Docekalova, J. Pokorny, I. Gregora, V. Tsurkan, H. Nakamura, F. Mayr, C. A. Kuntscher, A. Loidl, S. Bordács, D. Szaller, H. J. Lee, J. H. Lee, and I. Kézsmárki, “Lattice modes and the Jahn-Teller ferroelectric transition of  $\text{GaV}_4\text{S}_8$ ”, *Physical Review B* **94**, 1–5 (2016).
- [85] Z. Wang, E. Ruff, M. Schmidt, V. Tsurkan, I. Kézsmárki, P. Lunkenheimer, and A. Loidl, “Polar Dynamics at the Jahn-Teller Transition in Ferroelectric  $\text{GaV}_4\text{S}_8$ ”, *Physical Review Letters* **115**, 1–5 (2015).

- [86] I. Kézsmárki, S. Bordács, P. Milde, E. Neuber, L. M. Eng, J. S. White, H. M. Rønnow, C. D. Dewhurst, M. Mochizuki, K. Yanai, H. Nakamura, D. Ehlers, V. Tsurkan, and A. Loidl, “Néel-type skyrmion lattice with confined orientation in the polar magnetic semiconductor  $\text{GaV}_4\text{S}_8$ ”, *Nature Materials* **14**, 1116–1122 (2015).
- [87] Á. Butykai, S. Bordács, I. Kézsmárki, V. Tsurkan, A. Loidl, J. Döring, E. Neuber, P. Milde, S. C. Kehr, and L. M. Eng, “Characteristics of ferroelectric-ferroelastic domains in Néel-type skyrmion host  $\text{GaV}_4\text{S}_8$ ”, *Scientific Reports* **7**, 44663 (2017).
- [88] H.-G. von Ribbeck, “THz Near-Field Microscopy and Spectroscopy”, PhD thesis (Technische Universität Dresden, 2015).
- [89] J. Kischkat, S. Peters, B. Gruska, M. Semtsiv, M. Chashnikova, M. Klinkmüller, O. Fedosenko, S. Machulik, A. Aleksandrova, G. Monastyrskiy, Y. Flores, and W. T. Masselink, “Mid-infrared optical properties of thin films of aluminum oxide, titanium dioxide, silicon dioxide, aluminum nitride, and silicon nitride”, *Applied Optics* **51**, 6789–6798 (2012).
- [90] S. V. Kalinin and D. A. Bonnell, “Local potential and polarization screening on ferroelectric surfaces”, *Physical Review B* **63**, 125411 (2001).
- [91] D. Lang, L. Balaghi, S. Winnerl, H. Schneider, R. Hübner, S. C. Kehr, L. M. Eng, M. Helm, E. Dimakis, and A. Pashkin, “Nonlinear plasmonic response of doped nanowires observed by infrared nanospectroscopy”, *Nanotechnology* **30**, 084003 (2019).
- [92] E. Dimakis, U. Jahn, M. Ramsteiner, A. Tahraoui, J. Grandal, X. Kong, O. Marquardt, A. Trampert, H. Riechert, and L. Geelhaar, “Coaxial multishell (In,Ga)As/GaAs nanowires for near-infrared emission on Si substrates”, *Nano Letters* **14**, 2604–2609 (2014).
- [93] X. Dai, A. Messanvi, H. Zhang, C. Durand, J. Eymery, C. Bougerol, F. H. Julien, and M. Tchernycheva, “Flexible Light-Emitting Diodes Based on Vertical Nitride Nanowires”, *Nano Letters* **15**, 6958–6964 (2015).
- [94] D. Saxena, S. Mokkalapati, P. Parkinson, N. Jiang, Q. Gao, H. H. Tan, and C. Jagadish, “Optically pumped room-temperature GaAs nanowire lasers”, *Nature Photonics* **7**, 963–968 (2013).

- 
- [95] J. A. Czaban, D. A. Thompson, and R. R. LaPierre, “GaAs Core-Shell Nanowires for Photovoltaic Applications”, *Nano Letters* **9**, 148–154 (2009).
- [96] P. Krogstrup, H. I. Jørgensen, M. Heiss, O. Demichel, J. V. Holm, M. Aagesen, J. Nygard, and A. Fontcuberta i Morral, “Single-nanowire solar cells beyond the Shockley–Queisser limit”, *Nature Photonics* **7**, 1–5 (2013).
- [97] K. Peng, P. Parkinson, L. Fu, Q. Gao, N. Jiang, Y.-n. Guo, F. Wang, H. J. Joyce, J. L. Boland, H. H. Tan, C. Jagadish, and M. B. Johnston, “Single Nanowire Photoconductive Terahertz Detectors”, *Nano Letters* **15**, 206–210 (2015).
- [98] K. Peng, P. Parkinson, J. L. Boland, Q. Gao, Y. C. Wenas, C. L. Davies, Z. Li, L. Fu, M. B. Johnston, H. H. Tan, and C. Jagadish, “Broadband Phase-Sensitive Single InP Nanowire Photoconductive Terahertz Detectors”, *Nano Letters* **16**, 4925–4931 (2016).
- [99] S. F. Feste, J. Knoch, S. Habicht, D. Buca, Q. T. Zhao, and S. Mantl, “Silicon nanowire FETs with uniaxial tensile strain”, *Solid-State Electronics* **53**, 1257–1262 (2009).
- [100] S. A. Baig, J. L. Boland, D. A. Damry, H. H. Tan, C. Jagadish, H. J. Joyce, and M. B. Johnston, “An Ultrafast Switchable Terahertz Polarization Modulator Based on III–V Semiconductor Nanowires”, *Nano Letters* **17**, 2603–2610 (2017).
- [101] T. Mårtensson, C. P. T. Svensson, B. A. Wacaser, M. W. Larsson, W. Seifert, K. Deppert, A. Gustafsson, L. R. Wallenberg, and L. Samuelson, “Epitaxial III-V Nanowires on Silicon”, *Nano Letters* **4**, 1987–1990 (2004).
- [102] I. Beleckaitė, J. Treu, S. Morkötter, M. Döblinger, X. Xu, R. Adomavičius, J. J. Finley, G. Koblmüller, and A. Krotkus, “Enhanced THz emission efficiency of composition-tunable InGaAs nanowire arrays”, *Applied Physics Letters* **110**, 201106 (2017).
- [103] K. Storm, F. Halvardsson, M. Heurlin, D. Lindgren, A. Gustafsson, P. M. Wu, B. Monemar, and L. Samuelson, “Spatially resolved Hall effect measurement in a single semiconductor nanowire”, *Nature Nanotechnology* **7**, 718–722 (2012).

- [104] O. Hultin, G. Otnes, L. Samuelson, and K. Storm, “Simplifying Nanowire Hall Effect Characterization by Using a Three-Probe Device Design”, *Nano Letters* **17**, 1121–1126 (2017).
- [105] P. Parkinson, J. Lloyd-Hughes, Q. Gao, H. H. Tan, C. Jagadish, M. B. Johnston, and L. M. Herz, “Transient terahertz conductivity of GaAs nanowires”, *Nano Letters* **7**, 2162–2165 (2007).
- [106] J. L. Boland, G. Tütüncüoğlu, J. Q. Gong, S. Conesa-Boj, C. L. Davies, L. M. Herz, A. Fontcuberta i Morral, and M. B. Johnston, “Towards higher electron mobility in modulation doped GaAs/AlGaAs core shell nanowires”, *Nanoscale* **9**, 7839–7846 (2017).
- [107] J. M. Stiegler, R. Tena-Zaera, O. Idigoras, A. Chuvilin, and R. Hillenbrand, “Correlative infrared-electron nanoscopy reveals the local structure-conductivity relationship in zinc oxide nanowires”, *Nature Communications* **3**, 1131 (2012).
- [108] A. Arcangeli, F. Rossella, A. Tomadin, J. Xu, D. Ercolani, L. Sorba, F. Beltram, A. Tredicucci, M. Polini, and S. Roddaro, “Gate-Tunable Spatial Modulation of Localized Plasmon Resonances”, *Nano Letters* **16**, 5688–5693 (2016).
- [109] W. Choi, E. Seabron, P. K. Mohseni, J. D. Kim, T. Gokus, A. Cernescu, P. Pochet, H. T. Johnson, W. L. Wilson, and X. Li, “Direct Electrical Probing of Periodic Modulation of Zinc-Dopant Distributions in Planar Gallium Arsenide Nanowires”, *ACS Nano* **11**, 1530–1539 (2017).
- [110] Y. Zhou, R. Chen, J. Wang, Y. Huang, M. Li, Y. Xing, J. Duan, J. Chen, J. D. Farrell, H. Q. Xu, and J. Chen, “Tunable Low Loss 1D Surface Plasmons in InAs Nanowires”, *Advanced Materials* **30**, 1802551 (2018).
- [111] T. Tauchnitz, T. Nurmamyrtov, R. Hübner, M. Engler, S. Facsko, H. Schneider, M. Helm, and E. Dimakis, “Decoupling the Two Roles of Ga Droplets in the Self-Catalyzed Growth of GaAs Nanowires on  $\text{SiO}_x/\text{Si}(111)$  Substrates”, *Crystal Growth and Design* **17**, 5276–5282 (2017).



- [112] T. Tauchnitz, Y. Berdnikov, V. G. Dubrovskii, H. Schneider, M. Helm, and E. Dimakis, “A simple route to synchronized nucleation of self-catalyzed GaAs nanowires on silicon for sub-Poissonian length distributions”, *Nanotechnology* **29**, 504004 (2018).
- [113] E. Dimakis, M. Ramsteiner, A. Tahraoui, H. Riechert, and L. Geelhaar, “Shell-doping of GaAs nanowires with Si for n-type conductivity”, *Nano Research* **5**, 796–804 (2012).
- [114] L. Balaghi, G. Bussone, R. Grifone, R. Hübner, J. Grenzer, M. Ghorbani-Asl, A. Krashennnikov, H. Schneider, M. Helm, and E. Dimakis, “Up to 40% reduction of the GaAs band gap energy via strain engineering in core/shell nanowires”, *ArXiv e-prints*, 1803.10873, 1–12 (2018).
- [115] A. C. Gossard, “Modulation Doping of Semiconductor Heterostructures”, in *Molecular beam epitaxy and heterostructures* (Springer Netherlands, Dordrecht, 1985), pp. 499–531.
- [116] D. Spirkoska, A. Fontcuberta i Morral, J. Dufouleur, Q. Xie, and G. Abstreiter, “Free standing modulation doped core-shell GaAs/AlGaAs heteronanowires”, *physica status solidi (RRL) - Rapid Research Letters* **5**, 353–355 (2011).
- [117] J. L. Boland, S. Conesa-Boj, P. Parkinson, G. Tütüncüoğlu, F. Matteini, D. Ruffer, A. Casadei, F. Amaduzzi, F. Jabeen, C. L. Davies, H. J. Joyce, L. M. Herz, A. Fontcuberta i Morral, and M. B. Johnston, “Modulation Doping of GaAs/AlGaAs Core–Shell Nanowires With Effective Defect Passivation and High Electron Mobility”, *Nano Letters* **15**, 1336–1342 (2015).
- [118] T. P. Pearsall, R. Carles, and J. C. Portal, “Single longitudinal-mode optical phonon scattering in  $\text{Ga}_{0.47}\text{In}_{0.53}\text{As}$ ”, *Applied Physics Letters* **42**, 436–438 (1983).
- [119] H. A. Lorentz, *The theory of electrons and its applications to the phenomena of light and radiant heat* (Leipzig : B.G. Teubner; New York : G.E. Stechert, 1916).
- [120] M. Levinshtein and M. Shur, *Handbook Series on Semiconductor Parameters*, edited by S. L. Rumyantsev (World Scientific, London, 1999), pp. 62–88.

- 
- [121] J. S. Blakemore, “Semiconducting and other major properties of gallium arsenide”, *Journal of Applied Physics* **53**, R123–R181 (1982).
- [122] R. H. Lyddane, R. G. Sachs, and E. Teller, “On the polar vibrations of alkali halides”, *Physical Review* **59**, 673–676 (1941).
- [123] P. Drude, “Zur Elektronentheorie der Metalle”, *Annalen der Physik* **306**, 566–613 (1900).
- [124] D. Stehr, “Infrared studies of impurity states and ultrafast carrier dynamics in semiconductor quantum structures”, PhD thesis (Technische Universität Dresden, 2007).
- [125] R. Kiessling, W. B. Colson, S. Gewinner, W. Schöllkopf, M. Wolf, and A. Paarmann, “Femtosecond single-shot timing and direct observation of subpulse formation in an infrared free-electron laser”, *Physical Review Accelerators and Beams* **21**, 080702 (2018).
- [126] F. Huth, A. Chuvilin, M. Schnell, I. Amenabar, R. Krutokhvostov, S. Lopatin, and R. Hillenbrand, “Resonant antenna probes for tip-enhanced infrared near-field microscopy”, *Nano Letters* **13**, 1065–1072 (2013).
- [127] F. H. Su, F. Blanchard, G. Sharma, L. Razzari, A. Ayesheshim, T. L. Cocker, L. V. Titova, T. Ozaki, J.-C. Kieffer, R. Morandotti, M. Reid, and F. A. Hegmann, “Terahertz pulse induced intervalley scattering in photoexcited GaAs”, *Optics Express* **17**, 9620–9629 (2009).
- [128] L. Razzari, F. H. Su, G. Sharma, F. Blanchard, A. Ayesheshim, H.-C. Bandulet, R. Morandotti, J.-C. Kieffer, T. Ozaki, M. Reid, and F. A. Hegmann, “Nonlinear ultrafast modulation of the optical absorption of intense few-cycle terahertz pulses in n-doped semiconductors”, *Physical Review B* **79**, 193204 (2009).
- [129] K.-H. Goetz, D. Bimberg, H. Jürgensen, J. Selders, A. V. Solomonov, G. F. Glinskii, and M. Razeghi, “Optical and crystallographic properties and impurity incorporation of  $\text{Ga}_x\text{In}_{1-x}\text{As}$  ( $0.44 < x < 0.49$ ) grown by liquid phase epitaxy, vapor phase epitaxy, and metal organic chemical vapor deposition”, *Journal of Applied Physics* **54**, 4543–4552 (1983).

- [130] T. Tyborski, S. Kalusniak, S. Sadofev, F. Henneberger, M. Woerner, and T. Elsaesser, “Ultrafast Nonlinear Response of Bulk Plasmons in Highly Doped ZnO Layers”, *Physical Review Letters* **115**, 1–5 (2015).
- [131] F. Blanchard, D. Golde, F. H. Su, L. Razzari, G. Sharma, R. Morandotti, T. Ozaki, M. Reid, M. Kira, S. W. Koch, and F. A. Hegmann, “Effective mass anisotropy of hot electrons in nonparabolic conduction bands of n-doped InGaAs films using ultrafast Terahertz pump-probe techniques”, *Physical Review Letters* **107**, 107401 (2011).
- [132] T. P. Pearsall, *GaInAsP Alloy Semiconductors*, 1st ed. (John Wiley and Sons, 1982).
- [133] V. Ariel, “Effective Mass and Energy-Mass Relationship”, ArXiv e-prints, 1205.3995, 1–3 (2012).
- [134] J. Lloyd-Hughes, “Terahertz spectroscopy of quantum 2D electron systems”, *Journal of Applied Physics D: Applied Physics* **47**, 374006 (2014).
- [135] G. Sucha, S. R. Bolton, D. S. Chemla, D. L. Sivco, and A. Y. Cho, “Carrier relaxation in InGaAs heterostructures”, *Applied Physics Letters* **65**, 1486–1488 (1994).
- [136] J. Huang, M. Loeffler, U. Muehle, W. Moeller, H. Mulders, L. Kwakman, and E. Zschech, “A Study of Gallium FIB induced Silicon Amorphization using TEM, APT and BCA Simulation”, *Microscopy and Microanalysis* **21**, 1839–1840 (2015).
- [137] J. A. Schuller, R. Zia, T. Taubner, and M. L. Brongersma, “Dielectric Metamaterials Based on Electric and Magnetic Resonances of Silicon Carbide Particles”, *Physical Review Letters* **99**, 107401 (2007).
- [138] S. K. Andersson and M. E. Thomas, “Infrared properties of CVD  $\beta$ -SiC”, *Infrared Physics and Technology* **39**, 223–234 (1998).
- [139] T. E. Tiwald, J. A. Woollam, S. Zollner, J. Christiansen, R. B. Gregory, T. Wetteroth, S. R. Wilson, and A. R. Powell, “Carrier concentration and lattice absorption in bulk and epitaxial silicon carbide determined using infrared ellipsometry”, *Physical Review B* **60**, 11464–11474 (1999).

- [140] A. R. Gentle and G. B. Smith, “Angular selectivity: impact on optimised coatings for night sky radiative cooling”, in Proceedings of spie - the international society for optical engineering (2009), 74040J.
- [141] N. Q. Vinh, P. T. Greenland, K. Litvinenko, B. Redlich, A. F. G. van der Meer, S. A. Lynch, M. Warner, A. M. Stoneham, G. Aeppli, D. J. Paul, C. R. Pidgeon, and B. N. Murdin, “Silicon as a model ion trap: Time domain measurements of donor Rydberg states”, Proceedings of the National Academy of Sciences **105**, 10649–10653 (2008).
- [142] M. Ligowski, D. Moraru, M. Anwar, T. Mizuno, R. Jablonski, and M. Tabe, “Observation of individual dopants in a thin silicon layer by low temperature Kelvin Probe Force Microscope”, Applied Physics Letters **93**, 1–4 (2008).
- [143] A. Pospischil, M. M. Furchi, and T. Mueller, “Solar-energy conversion and light emission in an atomic monolayer p–n diode”, Nature Nanotechnology **9**, 257–261 (2014).
- [144] K. F. Mak and J. Shan, “Photonics and optoelectronics of 2D semiconductor transition metal dichalcogenides”, Nature Photonics **10**, 216–226 (2016).
- [145] W. Bao, N. J. Borys, C. Ko, J. Suh, W. Fan, A. Thron, Y. Zhang, A. Buyanin, J. Zhang, S. Cabrini, P. D. Ashby, A. Weber-Bargioni, S. Tongay, S. Aloni, D. F. Ogletree, J. Wu, M. B. Salmeron, and P. J. Schuck, “Visualizing nanoscale excitonic relaxation properties of disordered edges and grain boundaries in monolayer molybdenum disulfide”, Nature Communications **6**, 7993 (2015).
- [146] S. Dai, Z. Fei, Q. Ma, A. S. Rodin, M. Wagner, A. S. McLeod, M. K. Liu, W. Gannett, W. Regan, K. Watanabe, T. Taniguchi, M. Thiemens, G. Dominguez, A. H. C. Neto, A. Zettl, F. Keilmann, P. Jarillo-Herrero, M. M. Fogler, and D. N. Basov, “Tunable Phonon Polaritons in Atomically Thin van der Waals Crystals of Boron Nitride”, Science **343**, 1125–1129 (2014).

- 
- [147] T. J. Wieting and J. L. Verble, “Infrared and Raman Studies of Long-Wavelength Optical Phonons in Hexagonal MoS<sub>2</sub>”, *Physical Review B* **3**, 4286–4292 (1971).
- [148] O. Khatib, H. A. Bechtel, M. C. Martin, M. B. Raschke, and G. L. Carr, “Far Infrared Synchrotron Near-Field Nanoimaging and Nanospectroscopy”, *ACS Photonics* **5**, 2773–2779 (2018).



# List of Abbreviations

a-SNOM	aperture scanning near-field optical microscopy
AC	alternating current
AFM	atomic force microscopy
BS	beam splitter
CB	conduction band
CMOS	complementary metal-oxide-semiconductor
cw	continuous wave
DC	direct current
DOS	density of states
ELBE	electron linear accelerator with high brilliance and low emittance
FEL	free-electron laser
FELBE	free-electron laser at the Helmholtz-Zentrum Dresden-Rossendorf
FIB	focused ion beam
FTIR	fourier-transform infrared spectroscopy
FWHM	full width at half maximum
HZDR	Helmholtz-Zentrum Dresden-Rossendorf

IR	infrared
KPFM	Kelvin-probe force microscopy
KRS5	thallium bromo-iodide
LD	laser diode
LHe	liquid helium
LN <sub>2</sub>	liquid nitrogen
LO	longitudinal optical
LT	low temperature
LT AFM	low-temperature atomic force microscopy
LT s-SNIM	low-temperature scattering scattering scanning near-field infrared microscopy
MBE	molecular beam epitaxy
MCT	mercury cadmium telluride
MIR	mid-infrared
NA	numerical aperture
NP	nanoparticle
NW	nanowire
OAM	off-axis parabolic mirror
PDM	point-dipole model
PFM	piezoresponse force microscopy
PI	proportional-integral
PM	power meter



---

QCL	quantum cascade laser
RT	room temperature
RT AFM	room-temperature atomic force microscopy
RT s-SNIM	room-temperature scattering scanning near-field infrared microscopy
RWTH	Rheinisch-Westfälische Technische Hochschule
s-SNIM	scattering scanning near-field infrared microscopy
s-SNOM	scattering scattering scanning near-field optical microscopy
SEM	scanning electron microscopy
sMIM	scanning microwave impedance microscopy
SP	set point
SPhP	surface phonon polariton
SPM	scanning probe microscopy
STED	stimulated emission depletion
STM	scanning tunneling microscopy
TDS	terahertz time-domain spectroscopy
TEM	transverse electromagnetic
TMD	transition metal dichalcogenides
TO	transversal optical
vdW	van der Waals



# List of Symbols

## Physical Constants

Symbol	Description	SI quantity
$\hbar = h/2\pi$	reduced Planck constant	$1.054\,572 \times 10^{-34}$ Js
$\epsilon_0$	vacuum permittivity	$8.854\,187 \times 10^{-12}$ AsV <sup>-1</sup> m <sup>-1</sup>
$c$	speed of light (in vacuum)	$2.997\,925 \times 10^8$ ms <sup>-1</sup>
$e$	elementary charge	$1.602\,177 \times 10^{-19}$ C
$h$	Planck constant	$6.626\,070 \times 10^{-34}$ Js
$k_B$	Boltzmann constant	$1.380\,649 \times 10^{-23}$ JK <sup>-1</sup>
$m_e$	electron rest mass	$9.109\,384 \times 10^{-31}$ kg

## Greek Symbols

Symbol	Description	Dimension	SI unit
$\alpha$	electric polarizability (in Chapter 2)	L <sup>3</sup>	m <sup>3</sup>
$\alpha$	nonparabolicity factor (in Chapter 4)	M <sup>-1</sup> L <sup>-2</sup> T <sup>2</sup>	J <sup>-1</sup>
$\beta$	sample response function	–	1
$\delta$	half of the opening angle	–	1

$\gamma$	Lorentz factor (in Section 2.3.2)	–	1
$\gamma$	damping/scattering rate	$T^{-1}$	$s^{-1}$
$\Lambda$	wavenumber	$L^{-1}$	$m^{-1}$
$\lambda$	wavelength	L	m
$\nu$	vibrational quantum number	–	1
$\Omega$	cantilever resonance frequency	$T^{-1}$	Hz
$\omega$	angular frequency	$T^{-1}$	$s^{-1}$
$\Phi$	s-SNIM phase	–	1
$\sigma$	cross section (in Chapter 2)	$L^2$	$m^2$
$\sigma$	standard deviation (in Chapter 4)	$T^{-1}$	$s^{-1}$
$\tau$	pulse duration	T	s
$\varepsilon = \varepsilon' + i\varepsilon''$	relative permittivity	–	1
$\xi$	heating coefficient	$\Theta M^{-1} L^{-2} T^3$	$KW^{-1}$

### Roman Symbols

Symbol	Description	Dimension	SI unit
$A$	cantilever oscillation amplitude	L	m
$\vec{B}$	magnetic field	$MI^{-1}T^{-2}$	T
$C$	electric capacitance	$M^{-1}L^{-2}T^4I^2$	F
$\mathbf{d} = (d_{ij})$	piezoelectric tensor	$MLI^{-1}T^{-3}$	$V^{-1}m$

---

$D$	cantilever displacement	L	m
$d_u$	undulator gap distance	L	m
$\vec{E}$	electric field	$\text{MLT}^{-3}\text{I}^{-1}$	$\text{Vm}^{-1}$
$\mathcal{E}$	energy	$\text{ML}^2\text{T}^{-2}$	J
$\vec{F}$	force	$\text{MLT}^{-2}$	N
$f$	frequency	$\text{T}^{-1}$	Hz
$I$	intensity	$\text{MT}^{-3}$	$\text{Wm}^{-2}$
$J$	rotational quantum number	–	1
$\vec{k}$	wave vector	$\text{L}^{-1}$	$\text{m}^{-1}$
$K$	undulator parameter	–	1
$\vec{v}$	velocity	$\text{LT}^{-1}$	$\text{ms}^{-1}$
$l_c$	cavity length	L	m
$m^*$	effective mass	M	kg
$n = n' + in''$	refractive index	–	1
$\vec{p}$	electric dipole moment	ILT	Cm
$\vec{p}$	momentum (in Appendix C.1)	$\text{MLT}^{-1}$	$\text{kgms}^{-1}$
$P$	power	$\text{ML}^2\text{T}^{-3}$	W
$\vec{r}$	distance	L	m
$s$	s-SNIM amplitude/signal	$\text{ML}^2\text{I}^{-1}\text{T}^{-3}$	V
$T$	temperature	$\Theta$	K

$t$	time	T	s
$U$	voltage	$\text{ML}^2\text{I}^{-1}\text{T}^{-3}$	V
$V$	potential	$\text{ML}^2\text{T}^{-2}$	J
$w$	Gaussian beam's waist	L	m
$\mathbf{X} = (x_{ij})$	strain tensor	–	1
$x, y, z$	cartesian coordinates	L	m

# List of Publications

## Relevant for this PhD thesis

- **D. Lang**, L. Balaghi, S. Winnerl, H. Schneider, R. Hübner, S. C. Kehr, L. M. Eng, M. Helm, E. Dimakis, and A. Pashkin, “Nonlinear plasmonic response of doped nanowires observed by infrared nanospectroscopy”, *Nanotechnology* **30**, 084003 (2019).
- **D. Lang**, J. Döring, T. Nörenberg, Á. Butykai, I. Kézsmárki, H. Schneider, S. Winnerl, M. Helm, S. C. Kehr, and L. M. Eng, “Infrared nanoscopy down to liquid helium temperatures”, *Review of Scientific Instruments* **89**, 033702 (2018).

## Further publications

- L. Wehmeier, **D. Lang**, Y. Liu, X. Xiang, S. Winnerl, L. M. Eng, and S. C. Kehr, “Polarization-dependent near-field phonon nanoscopy of oxides: SrTiO<sub>3</sub>, LiNbO<sub>3</sub>, and PbZr<sub>0.2</sub>Ti<sub>0.8</sub>O<sub>3</sub>”, *Physical Review B* **100**, 03544 (2019).
- J. Döring, **D. Lang**, F. Kuschewski, L. Wehmeier, T. Nörenberg, L. M. Eng, and S. C. Kehr, “Low-temperature nanospectroscopy of the structural ferroelectric phases in single-crystalline barium titanate”, *Nanoscale* **10**, 18074-18079 (2018).
- S. C. Kehr, R. G. P. McQuaid, L. Ortman, T. Kämpfe, F. Kuschewski, **D. Lang**, J. M. Gregg, and L. M. Eng, “A Local Superlens”, *ACS Photonics* **3**, 20-26 (2016).
- S. Prucnal, F. Liu, M. Voelskow, L. Vines, L. Rebohle, **D. Lang**, Y. Berencén, S. Andric, R. Boettger, M. Helm, S. Zhou, and W. Skorupa,

“Ultra-doped n-type germanium thin films for sensing in the mid-infrared”, *Scientific Reports* **6**, 27643 (2016).

#### Conferences: oral contributions

- **D. Lang**, L. Balaghi, E. Dimakis, R. Hübner, S. C. Kehr, L. M. Eng, A. Pashkin, S. Winnerl, H. Schneider, M. Helm, “Nonlinear Plasmonic Response of Doped GaAs Nanowires Observed in s-SNIM”, *Conference on Lasers and Electro-Optics (CLEO)*, 14.-18.05.2018, San José, USA.
- **D. Lang**, L. Balaghi, E. Dimakis, S. C. Kehr, L. M. Eng, S. Winnerl, H. Schneider, M. Helm, “Infrared nanoscopy on Si-doped GaAs-InGaAs core-shell nanowires”, *DPG-Frühjahrstagung*, 11.-16.03.2018, Berlin, Deutschland.
- **D. Lang**, S. Winnerl, H. Schneider, J. Li, S. Clowes, B. Murdin, J. Döring, S. C. Kehr, L. M. Eng, M. Helm, “Terahertz spectroscopy of individual donors in silicon by low-temperature s-SNOM”, *DPG-Frühjahrstagung*, 06.-11.03.2016, Regensburg, Deutschland.

#### Conferences: poster contributions

- **D. Lang**, L. Balaghi, E. Dimakis, S. C. Kehr, L. M. Eng, S. Winnerl, H. Schneider, M. Helm, “Infrared nanoscopy on Si-doped GaAs-InGaAs core-shell nanowires”, *WIRMS 2017 - 9th International Workshop on Infrared Microscopy and Spectroscopy with Accelerator Based Sources*, 25.-28.09.2017, Oxford, United Kingdom.
- **D. Lang**, J. Döring, F. Kuschewski, S. C. Kehr, L. M. Eng, S. Winnerl, H. Schneider, M. Helm, “Low-temperature scattering scanning near-field optical microscopy (LT-s-SNOM)”, *DPG-Frühjahrstagung der Sektion Kondensierte Materie*, 19.-24.03.2017, Dresden, Deutschland **and** *OTST2017 - Optical Terahertz Science and Technology*, 02.-07.04.2017, London, United Kingdom.
- **D. Lang**, J. Döring, F. Kuschewski, S. C. Kehr, L. M. Eng, S. Winnerl, H. Schneider, M. Helm, “Scattering-type scanning near-field infrared microscopy at low temperatures”, *Smaller and Faster: Infrared and Tera-*



*hertz Spectral-Imaging at the Nanoscale with Synchrotron Radiation and Free Electron Laser Sources*, 01.-02.12.2016, Trieste, Italia.

- **D. Lang**, S. Winnerl, H. Schneider, J. Li, S. Clowes, B. Murdin, J. Döring, S. C. Kehr, L. M. Eng, M. Helm, "Terahertz spectroscopy of individual donors in silicon by low-temperature s-SNOM", *Silicon Quantum Information Processing 2016: Towards hybrid quantum circuits*, 08.09.2016, Cambridge, United Kingdom.
- **D. Lang**, T. Uhlig, S. C. Kehr, L. M. Eng, M. Helm, "Super-resonant infrared near-field microscopy", *DPG-Frühjahrstagung*, 15.-20.03.2015, Berlin, Deutschland **and** *German THz Conference 2015*, 08.-10.06.2015, Dresden, Deutschland



# Acknowledgments

Finally, I would like to acknowledge all those who contributed to the success of this work. First of all, I would like to thank Professor **Manfred Helm** for the opportunity to carry out the doctoral thesis under his scientific supervision as well as for the discussions on joint publications. Moreover, I am grateful to Professor **Thomas Taubner** for agreeing to review this PhD thesis.

## HZDR: FWIH, FWI, and ELBE

Thanks a lot to the experienced veterans of FWIH: Dr. **Harald Schneider**, Dr. **Alexej Pashkin**, and Dr. **Stephan Winnerl**, for all kinds of scientific discussions, general advice, and the numerous proof readings during my time at HZDR. I thank **Leila Balaghi**, Dr. **Emmanouil 'Manos' Dimakis**, Dr. **Lothar Bischoff**, and Dr. **René Hübner** for the fruitful collaboration regarding the nanowires. Furthermore, I am very grateful to Dr. **Wolfgang Seidel**, Dr. **J. Michael 'Mike' Klopff** and the whole **ELBE team** for the operation of the free-electron laser FELBE and for dedicated support. Last but not least I would like to mention all former FWIH colleagues for help in the laboratory, all kinds of discussions, and simply for having a great time: **Tommaso Venanzi**, **Johannes Schmidt**, **Johannes M. Braun**, Dr. **Jacob C. König-Otto**, **Ivan Fotev**, Dr. **Markus Fehrenbacher**, **Carsten Franke**, Dr. **Faina Eßer**, **Uta Lucchesi**, Dr. **Abhishek Singh**, Dr. **Rakesh Rana**, Dr. **Daniel Stephan**, **Tina Tauchnitz**, **Malte Welsch**, **Pedro Pereira**, and **Diogo de Moura Pedroso**. (Sorry to all those I forgot here.)

## IAP, s-SNOM group

Special thanks goes out to Dr. **Susanne C. “Sanni” Kehr**, Prof. **Lukas M. Eng**, and the whole s-SNOM group at TU Dresden. Sanni and Lukas introduced me to the high art of s-SNOM and accompanied me from my diploma thesis at the IAPP to the end of this work. Finally, I am very grateful to my ‘fellow sufferers’ in the FELBE s-SNIM laboratory for all discussions, experimental support, and for making endless nightshifts more bearable: these are Dr. **Jonathan Döring**, **Frederik Kuschewski**, Dr. **Thales de Oliveira**, **Lukas Wehmeier**, and **Tobias Nörenberg**. Also thanks to Dr. **Hans-Georg “Hansen” von Ribbeck** for the pioneer work regarding the LT s-SNIM and the far-infrared FELBE-based s-SNIM, and **Marc T. “MTob” Wenzel** for leaving behind the famous Si/SiO<sub>2</sub> sample with preliminary results.

## External

Although the project did not really work, I thank Prof. **Ben Murdin**, Dr. **Juerong (Nicole) Li**, Dr. **Steven Clowes**, and coworkers from the University of Surrey for the efforts and discussions on the ‘individual Si impurities’.

I would like to thank **Lena Jung**, **Martin Lewin** and the whole group of Prof. Thomas Taubner from the RWTH Aachen for giving me the opportunity to measure the nanowire cross sections in their lab.

Finally, many thanks to **Ádám Butykai** from the Budapest University of Technology and Economics, as well as **István Kézsmárki**, **Stephan Reschke** and coworkers from the Universität Augsburg for the collaboration on all GaV<sub>4</sub>S<sub>8</sub> related topics.

## My loved ones

Finally, my greatest thanks to my family, my friends, and my beloved partner for the mental support in difficult times. It would not have been possible without you!

# Versicherung

Hiermit versichere ich, dass ich die vorliegende Arbeit ohne unzulässige Hilfe Dritter und ohne Benutzung anderer als der angegebenen Hilfsmittel angefertigt habe; die aus fremden Quellen direkt oder indirekt übernommenen Gedanken sind als solche kenntlich gemacht. Die Arbeit wurde bisher weder im Inland noch im Ausland in gleicher oder ähnlicher Form einer anderen Prüfungsbehörde vorgelegt.

Diese Dissertation wurde am Institut für Ionenstrahlphysik und Materialforschung am Helmholtz-Zentrum Dresden-Rossendorf (HZDR) unter der wissenschaftlichen Betreuung von Prof. Dr. Manfred Helm, Professor am Institut für Angewandte Physik der Technischen Universität Dresden, angefertigt.

Hiermit erkläre ich, zu keiner anderen Zeit und an keinem anderen Ort zuvor ein anderes Promotionsverfahren eröffnet zu haben.

Ich erkenne die Promotionsordnung der Fakultät Mathematik und Naturwissenschaften der Technischen Universität Dresden in der gültigen Fassung vom 23.02.2011 an.

Dresden, den \_\_\_\_\_

Denny Lang







Bautzner Landstr. 400  
01328 Dresden, Germany  
Tel. +49 351 260-2260  
Fax +49 351 260-3285  
m.helm@hzdr.de  
<http://www.hzdr.de>